

---

A NUMERICAL INVESTIGATION OF THE ENERGY  
TRANSFER OF A BODY UNDER FLUIDELASTIC  
GALLOPING

---

BY H.G.K.G JAYATUNGA

A THESIS SUBMITTED TO MONASH UNIVERSITY IN FULFILLMENT OF THE  
REQUIREMENTS FOR THE DEGREE OF

DOCTOR OF PHILOSOPHY

Department of Mechanical Engineering

Monash University

October 2015



# STATEMENT OF ORIGINALITY

---

This thesis contains no material that has been accepted for the award of a degree or diploma in this, or any other, university. To the best of the candidates knowledge and belief, this thesis contains no material previously published or written by another person except where due reference is made in the text.

---

Kasun Gayantha Jayatunga

October 2015

# ABSTRACT

---

This thesis investigates the potential of energy harvesting through fluid-elastic galloping through studying the energy transfer between the body and the fluid.

This was carried out by numerically integrating a previously derived Quasi-Steady State (QSS), and via Direct Numerical Simulations (DNS) of the fluid-structure system.

A review of the literature identifies a need for new scaling parameters to better represent fluid-elastic galloping. New governing non-dimensional parameters for galloping namely, the combined mass-stiffness,  $\Pi_1$  and the combined mass-damping  $\Pi_2$  are formulated using natural time scales of the linearised QSS model. These new dimensionless groups provide a far better collapse of the predicted power output from the galloping of a square cross section in comparison with the classical parameters, regardless of whether the data comes from the QSS or DNS models. These time scales also provide a linear estimate of the frequency of the system, which is shown to match the frequency measured during the DNS simulations while  $\Pi_1 > 10$ .

A comparison between the quasi-steady state and direct numerical simulation data, reveals that the quasi-steady state model provides a good approximation of the power output at high  $\Pi_1$ . However, the QSS approximation deviates from the DNS predictions at low values of  $\Pi_1$  because the QSS model does not model vortex shedding which becomes more significant as  $\Pi_1$  decreases. However, the QSS model provides a reasonable prediction of the value of  $\Pi_2$  at which maximum power is produced. Both the error in predicted maximum power between the QSS and the DNS models and the relative power of the vortex shedding are quantified and scale approximately to  $1/\sqrt{\Pi_1}$ .

A semi-empirical search for an optimal body cross section for the extraction of energy is also presented. A hybrid rectangular/triangular body is used, to deliberately test the hypothesis that inhibition of the reattachment of the shear layers can promote large forces,

---

velocities, and therefore energy extraction. It is shown that two features control the energy extraction: the proximity of the shear layer to the body; the velocity of the flow in the shear layers. Both can be controlled by the amount of tapering of the afterbody, and a balance needs to be found between the two to optimize the geometry for energy extraction.

Comparison of results from the QSS and DNS models shows similar trends of maximum power being increased as the body becomes more tapered. However, the difference between the QSS and DNS models increases exponentially as the tapering is increased. Inspection of time averaged flow-field data show that the flow in the true fluid-structure situation is not quasi-static, violating the primary assumption of the QSS model. However, the QSS model still provides a reasonable initial qualitative approximation to design galloping energy harvesting systems.

# ACKNOWLEDGMENTS

---

I would like to express my deepest gratitude to my supervisors, Dr. Tan Boon Thong (Dr. Kenny) and Dr Justin Scott Leontini. Dr. Kenny thank you for entertaining me when I was having difficulties. Dr Justin, for explaining me complicated concepts and helping, guiding and providing words of encouragement when I was going through tough situations. I would like to thank both my supervisors for training me to conduct quality research and teaching me proper research techniques.

My warmest gratitude goes to the administrator of the Monash High-performance computer facility (SUN grid), Philip Chan for helping me out immensely and facilitating to carry out my simulations. Mention must be made to Monash University, Malaysia for providing me with the scholarship to pursue my PhD.

I would like to thank my closest friends Nishan and Hasuli who were pseudo-siblings for me from undergraduate level. Thank you for the support and encouragement. I would like to extend my thanks to Rangika and Devangi. Dr Anuja Dharmarathna, thank you for all the support, guidance and treating me as your own son when I needed help.

My Deepest gratitude goes out to my close friends in Monash Malaysia for helping me out, providing support and being there for me when I was going through very tough situations.

I am indebted for the support provided by my family. Amma, Thatha, Akki, Ayya and Sanula (“Johnny”). Amma thank you for firmly telling me that “ A PhD has to be earned...!”. A special thank goes out to Saranga for all the support you provided. My gratitude extends to Mr Asanka Ranasinghe, Ms Dayani De Silva Mr Shanaka De Silva for providing me strength and encouragement.

---

Last but definitely not least, I am much indebted to Mrs Malin Bamunuarachchi for the blessings, prayers and the encouragement given to me when I hit “rock-bottom” and was on the verge of giving up. Thank you madam.

# A LIST OF PUBLICATIONS RELATED TO THIS THESIS

---

JAYATUNGA, H. G. K. G., TAN, B.T & LEONTINI, J.S. 2015 A study on the energy transfer of a square prism under fluid-elastic galloping *Journal of Fluids and Structures* **55**,384–397.

LEONTINI, J.S., JISHENG, Z., JAYATUNGA, H. G. K. G., LO JANCONO, D., TAN B. T., & SHERIDAN, J. 2014 Frequency selection and phase locking during aeroelastic galloping *19th Australasian Fluid Mechanics Conference, Melbourne, Australia*



# NOMENCLATURE

---

Symbol	Description
$a_1, a_3, a_5, a_7$	Coefficients of the polynomial to determine $C_y$
$A$	Displacement amplitude
$\mathcal{A} = DL$	Frontal area of the body
$c$	Damping constant
$c^* = cD/mU$	Non-dimensionalised damping factor
$C_L = F_L/0.5\rho U^2 DL$	Lift force coefficient
$C_D = F_D/0.5\rho U^2 DL$	Drag force coefficient
$C_y = F_y/0.5\rho U^2 DL$	Transverse force coefficient
$D$	Characteristic length (side length) of the cross section of the body
$El$	Subscript denoting integration over a single element
$f = \sqrt{k/m}/2\pi$	Natural frequency of the system
$f_g$	Frequency of galloping
$f_s$	Frequency of vortex shedding
$f_{QSS}$	Frequency predicted by the QSS model
$f_{lin}$	Linear frequency
$f_{DNS}$	Frequency predicted by DNS simulations
$F_L$	Instantaneous lift force
$F_D$	Instantaneous drag force
$F_y$	Instantaneous transverse force
$F_0$	Amplitude of the oscillatory force due to vortex shedding

Continued on next page →

---

← Continued from previous page

Symbol	Description
$\mathcal{F}$	Fourier transform of velocity
$g$	Index of the data points inside each element in the $\xi$ -direction
$h$	Variable indicative of resolution of macro-element mesh
$i$	Index of the data point being considered during construction of the Lagrange polynomial in the $\xi$ -direction
$\mathbf{J}$	Jacobian operator for coordinate transformation
$j$	Data point index in computational space in $\eta$ -direction
$k$	Spring constant
$m$	Mass of the body
$m_a$	Added mass
$m^* = m/\rho D^2 L$	Mass ratio
$\mathbf{N}$	The non-linear convection term in the NavierStokes equations, $(\mathbf{V} \cdot \nabla)\mathbf{V}$
$n$	Timestep count to the current timestep
$\mathbf{n}$	Unit vector in the direction normal to a boundary
$P_d$	Power dissipated due to mechanical damping
$P_{in} = \rho U^3 D/2$	Energy flux of the approaching flow
$P_m$	Dimensionless mean power
$P_t$	Power transferred to the body by the fluid
$P_s$	Surface pressure
$P_{trial}$	Trial solution for pressure
$q$	Data point index in computational space in the $\xi$ -direction
$\mathbf{R}$	Residual formed when substituting trial solution into governing equations
$Re$	Reynolds number
$s$	Data point index in computational space in the $\eta$ -direction
$t$	Time
$U$	Freestream velocity

Continued on next page →

---

← Continued from previous page

Symbol	Description
$U_i$	Induced velocity
$U^* = U/fD$	Reduced velocity
$v$	Normalised component of velocity in the $y$ -direction
$\mathbf{v}_{body}$	Instantaneous transverse velocity of the body
$V_m$	Velocity magnitude of the flow
$\mathbf{V}$	Non-dimensional velocity vector, $\mathbf{u}/U$
$\mathbf{V}_{trial}$	Trial solution for velocity
$\mathbf{V}^*$	Intermediate normalised velocity vector at the end of the advection sub-step
$\mathbf{V}^{**}$	Intermediate normalised velocity vector at the end of the pressure sub-step
$\mathbf{V}_{body}$	Transverse velocity of the body, $\dot{y}/U$
$\mathbf{V}_{body}^{(n+1)\dagger}$	First approximation of $\mathbf{V}_{body}$ at the end of the timestep during the convection substep of the elastically mounted body.
$\mathbf{V}_{body}^{(n+1)\ddagger}$	Second approximation of $\mathbf{V}_{body}$ at the end of the timestep during the convection substep of the elastically mounted body.
$\mathbf{V}_{body}^{(n+1)'} $	Approximation of $\mathbf{V}_{body}$ at the end of the timestep after relaxation during the elastically-mounted cylinder convection substep
$\mathbf{V}^{(n)}$	Normalised velocity vector at timestep $n$
$\mathbf{V}^{(n+1)}$	Normalised velocity vector at timestep $n + 1$
$\widehat{\mathbf{V}}^*$	Vector of $\mathbf{V}^*$ at the node points
$\Delta \mathbf{V}_{body}$	Change in $\mathbf{V}_{body}$ over one timestep
$\Delta \mathbf{V}_{body}^\dagger$	First approximation of change in $\mathbf{V}_{body}$ over one timestep during the elastically-mounted body convection substep
$x$	Cartesian coordinate in the freestream flow direction, positive downstream

Continued on next page →

← Continued from previous page

Symbol	Description
$y$	Cartesian coordinate transverse to the flow direction and span direction
$y_{body}$	Transverse cylinder displacement
$y_{body}^{(n+1)\dagger}$	A first approximation to $y_{body}$ at the end of the timestep during the elastically-mounted body convection substep
$y, \dot{y}, \ddot{y}$	Transverse displacement, velocity and acceleration of the body/cylinder
$Y = y/D$	Non-dimensional transverse displacement
$\dot{Y} = m^* \dot{y}/a_1 U$	Non-dimensional transverse velocity
$\ddot{Y} = m^{*2} D \ddot{y}/a_1^2 U^2$	Non-dimensional transverse acceleration
$\Delta\tau$	The non-dimensional timestep
$\epsilon$	Under-relaxation parameter used during the elastically-mounted body convection substep
$\eta$	Coordinate axis in computational space
$\xi$	Coordinate axis in computational space
$\Gamma_1 = 4\pi^2 m^{*2}/U^{*2} a_1^2$	First dimensionless group arising from linearised, non-dimensionalised equation of motion
$\Gamma_2 = c^* m^*/a_1$	Second dimensionless group arising from linearised, non-dimensionalised equation of motion
$\lambda$	Inverse time scale of a galloping dominated flow
$\lambda_{1,2}$	Eigenvalues of linearised equation of motion
$\omega_n = 2\pi f$	Natural angular frequency of the system
$\omega_s$	Vortex shedding angular frequency
$\Pi_1 = 4\pi^2 m^{*2}/U^{*2}$	Combined mass-stiffness parameter
$\Pi_2 = c^* m^*$	Combined mass-damping parameter
$\rho$	Fluid density
$\varphi$	Strain rate tensor
$\theta = \tan^{-1}(\dot{y}/U)$	Instantaneous angle of incidence (angle of attack)

Continued on next page →

---

← Continued from previous page

Symbol	Description
$\zeta = c/2m\omega_n$	Damping ratio

# CONTENTS

---

<b>1</b>	<b>Preliminary remarks</b>	<b>2</b>
<b>2</b>	<b>A review of the literature</b>	<b>5</b>
2.1	Fluid-elastic galloping . . . . .	5
2.1.1	Excitation of galloping . . . . .	5
2.1.2	Quasi-steady state theory . . . . .	6
2.1.3	Induced force and the shear layers . . . . .	10
2.1.4	Governing parameters of galloping . . . . .	14
2.1.5	Frequency response . . . . .	14
2.1.6	Fluid mechanics governing the galloping response . . . . .	15
2.1.7	Galloping as a mechanism of energy harvesting . . . . .	17
2.1.8	Review summary and statement of objectives . . . . .	19
<b>3</b>	<b>Methodology and validation</b>	<b>22</b>
3.1	Introduction . . . . .	22
3.1.1	Parameters used . . . . .	22
3.2	Quasi-steady model . . . . .	24
	Solving the quasi-steady state equation . . . . .	24
3.3	Calculation of average power . . . . .	25
3.4	Direct numerical simulations (DNS) . . . . .	26
3.4.1	Governing equations . . . . .	26
3.4.2	Temporal discretisation: Time-splitting . . . . .	28
	Integration of the substep equations . . . . .	29
	The convection substep . . . . .	30

	The pressure substep . . . . .	32
	The diffusion substep . . . . .	33
	Spatial discretisation: Spectral element method . . . . .	33
3.4.3	Convergence and validation studies . . . . .	38
	Domain size . . . . .	38
	Boundary conditions . . . . .	38
	Convergence . . . . .	39
<b>4</b>	<b>Governing parameters of fluid-elastic galloping</b>	<b>42</b>
4.1	Introduction . . . . .	42
4.1.1	Static body results . . . . .	43
4.1.2	Formulation of the new dimensionless groups $\Pi_1$ and $\Pi_2$ . . . . .	45
4.1.3	Comparison of $\Pi_1$ and $\Pi_2$ with classical VIV parameters . . . . .	47
4.1.4	Comparison of power between high and low $Re$ data . . . . .	50
4.1.5	Dependence on mass-stiffness, $\Pi_1$ . . . . .	51
4.1.6	Dependence on the mass ratio $m^*$ . . . . .	55
4.1.7	Comparison with DNS data . . . . .	55
4.2	Frequency response of the system . . . . .	64
4.2.1	Formulating the linear frequency of the system . . . . .	64
4.2.2	Comparison of predicted frequencies using different approaches . . . . .	65
	Spectral analysis of the DNS data at low $\Pi_1$ . . . . .	69
	Comparison of $f_{lin}$ and $f_{QSS}$ in $\Pi_1$ $\Pi_2$ space . . . . .	71
4.3	Summary of analysis of power transfer using the QSS model . . . . .	73
<b>5</b>	<b>Optimization of the cross section for power extraction</b>	<b>76</b>
5.1	Introduction . . . . .	76
5.2	Influence of the shear layers . . . . .	78
5.3	Static body results . . . . .	80
5.4	QSS Mean power output . . . . .	82
5.5	Investigation of flow characteristics at low $\frac{d}{T}$ cases . . . . .	83
5.5.1	Surface pressure . . . . .	83
5.5.2	Velocity profiles at the points of flow separation . . . . .	84

---

5.5.3	Mean streamlines . . . . .	86
5.6	Fluid-structure interaction (DNS) results . . . . .	89
5.6.1	Mean power data . . . . .	89
5.6.2	Flow-field data . . . . .	90
5.7	Design considerations for a galloping energy extraction system through in- hibition of shear layer reattachment. . . . .	94
5.8	Summary . . . . .	94
<b>6</b>	<b>Conclusions</b>	<b>97</b>



# CHAPTER 1

---

## PRELIMINARY REMARKS

Fluid-structure interactions occur in many situations in our everyday lives. From the blood flow through our veins to the flight of an A-380 airbus, fluid structure interactions have a significant influence. Vibrations are an important phenomenon which have either a desirable or otherwise effect, in mechanical systems, both in nature and engineering.

Flow induced vibrations are one type of the significant phenomena occurring as a result of fluid structure interactions. In this broader class of flow induced vibrations, fluid-elastic galloping is one commonly visible phenomenon in nature. Fluid-elastic galloping in particular has been widely researched during the past century due to the adverse effects caused on civil structures where vibrations created through fluid-elastic galloping leading to failure either through high peak loads or the cumulative effect of fatigue. One such classic example used in the engineering field is the collapse of Tacoma Narrows bridge on November 7<sup>th</sup> 1940. Another example is the vibrations created by galloping on transmission lines due to ice deposition (Parkinson and Smith, 1964). Due to such adverse effects caused by fluid-elastic galloping, extensive research has been conducted to understand its mechanism in order to control and suppress these vibrations.

With detrimental environmental impact of fossil fuel, the search for alternative energy sources with minimal environmental impact has become an important area of research in the modern world, and researchers conducting studies on flow induced vibrations are moving towards investigating the possibility of harvesting energy from these vibrations; hence, finding mechanisms to excite and sustain these vibrations is paramount (Barrero-Gil et al.,

---

2010).

One such research group at the University of Michigan has conducted extensive research on energy extraction through Vortex Induced Vibrations (VIV) (Bernitsas et al., 2008, 2009; Raghavan and Bernitsas, 2011; Lee and Bernitsas, 2011). However, VIV is a resonance type of phenomenon where the vibrations occur when the vortex shedding frequency aligns with the natural frequency of the system. This phenomenon is known as “lock-in”.

In contrast, fluid-elastic galloping is a “velocity dependent and damping controlled ” mechanism (Païdoussis et al., 2010); thus, it operates over a wide range of natural frequencies and flow speeds. More in-depth discussion on the mechanism of fluid-elastic galloping is presented in section 2. The fact that galloping operates over a wide range of natural frequencies provides fluid-elastic galloping an advantage over VIV as a mode of energy extraction.

Although extensive research has been conducted in the area of fluid-elastic galloping, the area of energy harvesting through fluid-elastic galloping is quite new where the concept was proposed very recently by Barrero-Gil et al. (2010). Thus, more fundamental work is needed in this area, particularly on the energy transfer between the fluid and the body.

To bridge the gap of existing knowledge the following approach has been employed in the work presented in this thesis. A review of literature is presented in chapter 2 where the mechanism of galloping and the theoretical model which describes galloping is extensively discussed with reference of existing literature; also the gaps of current knowledge on energy transfer during galloping are identified. Based on these identifications of the gaps of the current knowledge, the objectives are defined.

The study is presented in two phases. Phase 1 is focused on understanding the governing mechanical parameters followed by phase 2 where the possibility of achieving a higher power output though inhibition of shear layer reattachment is investigated.

The tools employed to carry out this study are discussed in chapter 3, where the methodology and validation are presented. Here, the quasi-steady state model is introduced and the method of numerical integration in order to solve this model is discussed followed by the presentation of equations which are used to calculate average power. Direct Numerical Simulations(DNS) at low Reynolds numbers are carried out for both stationary and oscillating bluff bodies. The models and numerical algorithms employed to carry out the DNS

are presented, followed by a convergence and validation study.

An inadequacy of the traditional scaling parameters used to describe galloping is identified in the literature review; a new set of non-dimensionalised scaling parameters namely  $\Pi_1$  and  $\Pi_2$  is formulated from the linearised Quasi-Steady State (QSS) model and presented in chapter 4. These parameters are then compared with the existing scaling parameters. The influence of these parameters on mean power is then discussed in  $\Pi_1$  and  $\Pi_2$  space followed by a comparison between the QSS and DNS data.

The influence of  $\Pi_1$  and  $\Pi_2$  on fluid-elastic galloping is further investigated in this chapter through a study on the influence of the new scaling parameters on the frequency response. An expression for the galloping frequency is formulated based on  $\Pi_1$  and  $\Pi_2$  using the eigenvalues of the linearized system. The frequency data obtained from this model are compared with data obtained using other approaches. The limitations of this linear frequency model are identified and the region where this model can be applied are identified and quantified.

The results and discussion on the work carried out on phase 2 are presented in chapter 5. As hypothesised, inhibition of the shear layer re-attachment could lead to higher power output based on the data presented in Luo et al. (1994); the testing of this hypothesis is carried out here.

The shear layer re-attachment is inhibited systematically by tapering away the top and bottom trailing edges of the square cross section. The static body results, QSS predictions, the predictions from the fluid-structure interaction simulations and the underpinning fluid-mechanics are discussed. This chapter concludes with presentation of some fundamental design considerations which will be used to obtain an efficient energy harvesting system through control of the shear layer reattachment.

Finally, the conclusions obtained from this study are presented in chapter 6.

## CHAPTER 2

---

# A REVIEW OF THE LITERATURE

### 2.1 Fluid-elastic galloping

Fluid-elastic galloping is one of the common observable flow-induced vibration modes of a slender body. This phenomenon is most common in civil structures, such as buildings and iced-transmission lines. The term “aeroelastic galloping” is commonly used as the body is driven by wind. However, this mechanism can occur on a slender body immersed in any Newtonian fluid, provided that the conditions to sustain the galloping mechanism are satisfied. This work is based on a general Newtonian flow, thus the term “fluid-elastic galloping” is used throughout this thesis.

#### 2.1.1 Excitation of galloping

Païdoussis et al. (2010) describe galloping as a “velocity dependent and damping controlled” phenomenon. Therefore, in order for a body to gallop, an initial excitation has to be given to that body. While this excitation is mainly caused by the force created from vortex shedding, other fluid instabilities may contribute to this initial excitation. When a bluff body moves along the transverse direction of a fluid flow, it generates a force along the transverse direction. This force, also termed as the induced lift, is a result of the fluid flow and the motion of the body. When this body is attached to a flexible system (i.e. a system that can be modelled by a spring, mass and damper), the induced lift becomes the forcing component of the system. Galloping is sustained if the induced lift is periodic and in phase

with the motion of the body.

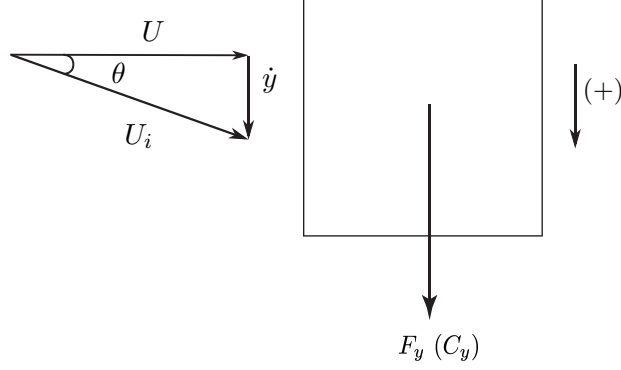


Figure 2.1: Induced angle of attack on a square prism due to the resultant of free-stream velocity of the fluid and transverse velocity of the body.

A square cross section can be used as an example to further explain the galloping phenomenon. Figure 2.1 illustrates the motion of the body at a given instant. The induced angle of attack is formed on the square cross section as a result of the free stream velocity vector  $U$  and the transverse velocity vector of the body  $\dot{y}$ . An angle of attack implies that there will be a non-zero lift force on the body. This transverse force also known as the induced lift generates in the same direction as the transverse velocity of the body as illustrated in figure 2.1 in a body under the influence of galloping. Though the illustration is a square prism, this mechanism can also be observed on any body that can have an angle of attack. The sign convention in this figure (and generally used in this scope of research) states that downward direction is positive. Further explanation as to how the transverse forcing is generated is provided in section 2.1.3

### 2.1.2 Quasi-steady state theory

The vibrations experienced in iced electric transmission lines was the key phenomenon which compelled researchers into studying fluid-elastic galloping. Some of the earlier work by Glauert (1919) and Den Hartog (1956) led to the pioneering study on galloping by Parkinson and Smith (1964) which produced a mathematical model for a system under the influence of fluid-elastic galloping. A non-linear oscillator model was developed by Parkinson and Smith (1964) to predict the response of the system. Since then, this model

has been widely used in almost all subsequent studies on galloping. Essentially, the model assumes the flow is quasi-steady. This means that the instantaneous induced lift force of the oscillating body is equal to that of the lift force generated by the same body when static at the same induced angle of attack. For the quasi-steady assumption to be valid, the conditions below have to be satisfied.

- The velocity of the body does not change rapidly
- There is no interaction between vortex shedding and galloping

Both of these conditions imply that the vortex shedding frequency must be much higher than the galloping frequency.

The oscillator equation was solved using the Krylov and Bogoliubov method (Parkinson and Smith, 1964). The results obtained from experiments, carried out at  $Re = 22000$  and a mass ratio ( $m^*$ ) around 1164 had a good agreement with the theoretical data which is shown in figure 2.2. The details of this quasi-steady model are provided in section 2.1.2.

Figure 2.2 shows the comparison of the scaled amplitude of oscillation between the mathematical model and the experimental data of Parkinson and Smith (1964). The data shows a good agreement between the model and the experiments.

### Quasi-steady state oscillator model

A simple transversely oscillating system with external driving force could be modelled with a spring mass damper system which can be expressed as,

$$m\ddot{y} + c\dot{y} + ky = Q, \quad (2.1)$$

where the forcing term  $Q$  is the external force which drives the system.

Thus, the quasi-steady equation of motion of a transversely oscillating body under galloping, with linear springs and damping can be expressed by replacing the forcing term with the induced force (explained in section 2.1.2),

$$m\ddot{y} + c\dot{y} + ky = F_y, \quad (2.2)$$

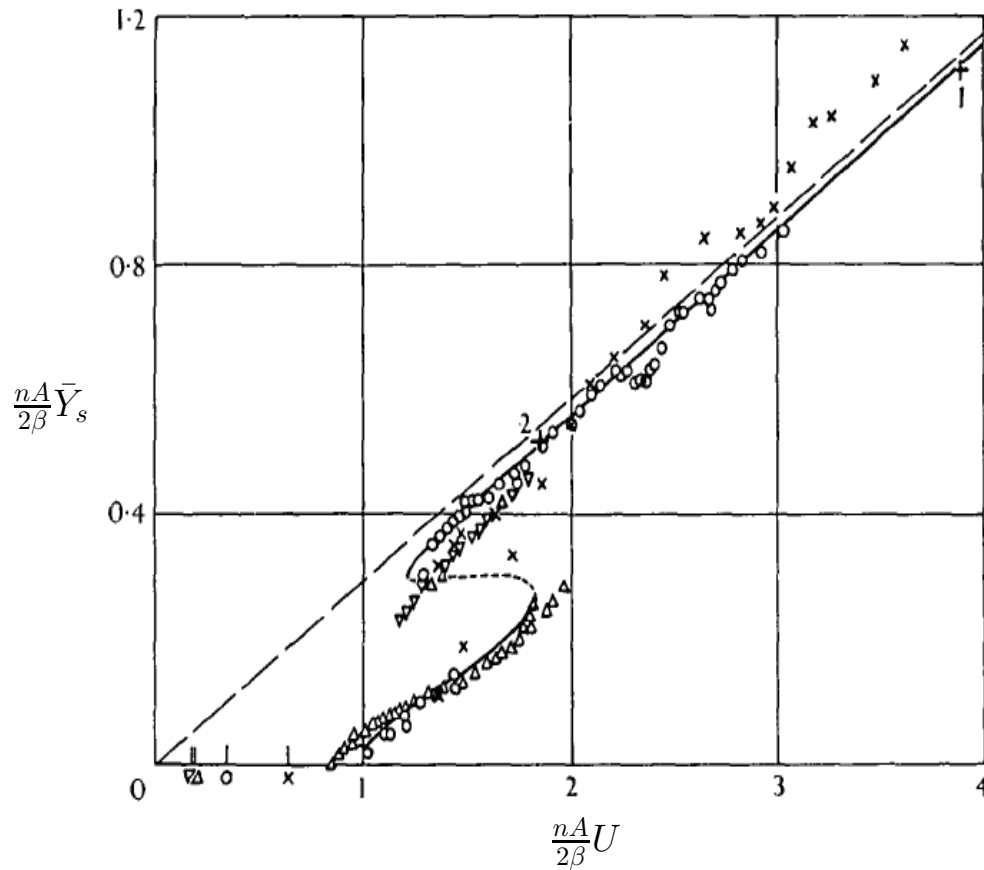


Figure 2.2: “Collapsed amplitude-velocity characteristic. Theory: ——— stable limit cycle, ---unstable limit cycle. Experiment ( $\times$ )  $\beta = .00107$ , ( $\circ$ )  $\beta = .00196$ , ( $\triangle$ )  $\beta = .00364$ , ( $\nabla$ )  $\beta = .00372$ , +1  $\beta = .0012$ , +2  $\beta = .0032$  Reynolds numbers 4,000 – 20,000 ”. Figure extracted from Parkinson and Smith (1964).  $\frac{nA}{2\beta} \bar{Y}_s$  is the dimensionless displacement amplitude parameter and  $\frac{nA}{2\beta} U$  is the reduced velocity.  $\beta$  is the damping ratio and  $n = \frac{1}{m^*}$ . The experimental data shows a good agreement with the theoretical model.

where the forcing term  $F_y$  is given by

$$F_y = \frac{1}{2}\rho U^2 \mathcal{A} C_y. \quad (2.3)$$

As explained in section 2.1.2, the quasi-steady assumption uses the stationary  $C_y$  data for varying angles of attack as inputs to the oscillator equation. Parkinson and Smith (1964) used a 7<sup>th</sup> order curve fit (retaining only the odd powers) to interpolate the stationary  $C_y$  data as a function of the angle of attack. The order of the polynomial can be chosen arbitrarily depending on the study. For example Barrero-Gil et al. (2009, 2010) used a 3<sup>rd</sup> order polynomial in order to simplify the analytical model. However, Ng et al. (2005) pointed out that a 7<sup>th</sup> order polynomial is sufficient as higher order polynomials do not provide a significantly better result. When using a 7<sup>th</sup> order polynomial, the lift coefficient is expressed as a function of the angle of attack  $\theta$  in the model as,

$$C_y(\theta) = a_1 \left( \frac{\dot{y}}{U} \right) - a_3 \left( \frac{\dot{y}}{U} \right)^3 + a_5 \left( \frac{\dot{y}}{U} \right)^5 - a_7 \left( \frac{\dot{y}}{U} \right)^7. \quad (2.4)$$

By substituting this forcing function into the oscillator equation (Eq:2.2) the quasi-steady state (QSS) model can be obtained as

$$m\ddot{y} + c\dot{y} + ky = \frac{1}{2}\rho U^2 \mathcal{A} \left( a_1 \left( \frac{\dot{y}}{U} \right) - a_3 \left( \frac{\dot{y}}{U} \right)^3 + a_5 \left( \frac{\dot{y}}{U} \right)^5 - a_7 \left( \frac{\dot{y}}{U} \right)^7 \right). \quad (2.5)$$

The current study is focused on the low  $Re$  region, and it is an established fact that in this region the vortex shedding will be well-correlated along the span and therefore will provide a significant forcing. Joly et al. (2012) introduced an additional sinusoidal forcing function to the model in order to integrate this forcing by vortex shedding. By the addition of this forcing Joly et al. (2012) managed to obtain accurate predictions of the displacement amplitude even at low mass ratios, where the galloping is significantly suppressed by the vortex shedding to the point that it is no longer detectable. However, the strength or the amplitude of this sinusoidal forcing needed to be tuned in an *ad hoc* manner, and the relationship between this forcing and the other system parameters was not clear. Thus in the current study this forcing is not used.

### Presence of hysteresis

Parkinson and Smith (1964) observed a hysteresis region when the displacement amplitude



## 2. A REVIEW OF THE LITERATURE

---

was plotted as a function of the reduced velocity. Essentially two amplitudes were observed for the same reduced velocity depending on the initial condition. This fact is quite vital for energy harvesting as two values of energy levels can be present for the same reduced velocity. Thus, care is required in considering the initial conditions of the system to gain a higher power output.

Although hysteresis was observed in the amplitude data of Parkinson and Smith (1964), the studies carried out by Barrero-Gil et al. (2009) and Joly et al. (2012) at much lower Reynolds numbers ( $159 \leq Re \leq 200$ ), did not show any hysteresis. Luo et al. (2003) concluded that hysteresis was present due to the presence of an inflection point in the  $C_y$  curve which was only observed at high Reynolds numbers (Parkinson and Smith (1964) data) and was not present at lower Reynolds numbers. It was further explained by Luo et al. (2003) that the cause of this inflection point was the intermittent reattachment of the shear layer at certain angles that occurred at high Reynolds numbers.

Figure 2.3 shows the vorticity contours of a square cross section obtained at various points of the vortex shedding cycle, at  $Re = 1000$  at  $\theta = 2^\circ$  obtained from Luo et al. (2003) using the diffusion-vortex method and vortex-in-cell method. The points 7 and 11 show the intermittent shear layer reattachment which causes the hysteresis in the  $C_y$  vs.  $\theta$  curve at high Reynolds numbers.

### 2.1.3 Induced force and the shear layers

The quasi-steady model has already been validated and re-validated by many studies (Parkinson and Smith, 1964; Barrero-Gil et al., 2009; Luo et al., 2003) and proven to model galloping. Since this model essentially assumes that the system is quasi-steady, the mean flow-field data of static body simulations at various angles of incidence can be used to analyse the behaviour of the instantaneous flow field of a galloping system at the same instantaneous induced angle.

Païdoussis et al. (2010); Parkinson and Smith (1964); Barrero-Gil et al. (2010) and many other published studies state that a system which sustains galloping should satisfy

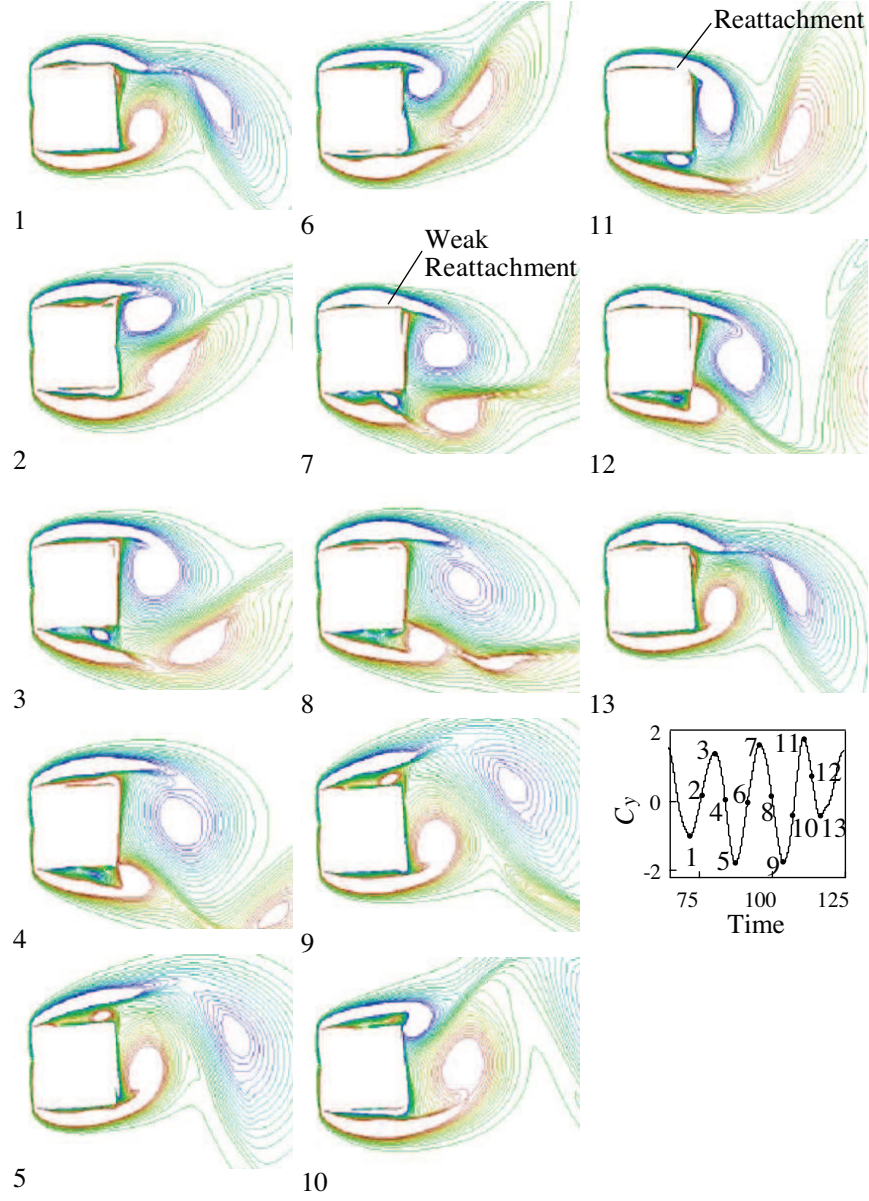


Figure 2.3: Vorticity contours of  $C_y$  and the corresponding time for  $Re = 1000$ ,  $\theta = 2^\circ$  extracted from Luo et al. (2003). The intermittent shear level is visible in points 7 and 11

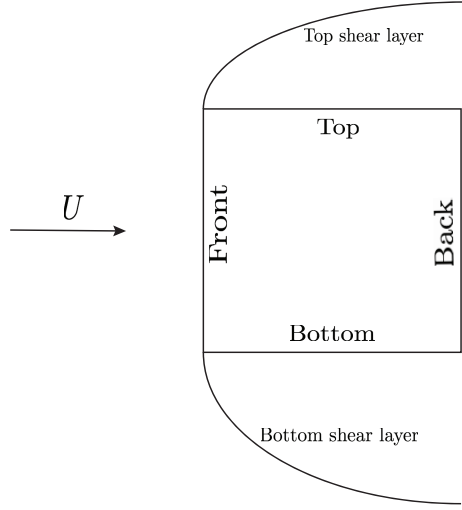


Figure 2.4: Illustration of the top and bottom shear layers



Figure 2.5: Shear strain rate magnitude contours of time averaged flow field on a stationary square section at  $Re = 200$  at different incidence angles. (a)  $2^\circ$  ( $C_y$  increases), (b)  $4^\circ$  ( $C_y$  peaks) and (c)  $6^\circ$  ( $C_y$  decreases). The bottom shear layer comes closer to the bottom wall and reattaches as the angle of incidence increases.

the condition that  $\partial C_y / \partial \theta > 0$ , i.e, an upward motion from the equilibrium position should induce an upward lift force. The mean induced lift ( $C_y$ ) occurs due to the unbalanced pressure distribution on the top and bottom sides of the afterbody of the cross section (refer figure 2.4) when a small transverse velocity is given (Parkinson, 1989). This pressure difference of the afterbody is a result of the relative proximity of the top and bottom shear layers (illustrated in figure 2.4) to the respective sides of the body.

Contour plots of the shear strain rate magnitude which is directly proportional to shear stress, for a static square cross section at various incidence angles as shown in figure 2.5 clearly shows the behaviour of the shear layers at either sides of the body. Data are presented for three key incidence angles of  $2^\circ$ ,  $4^\circ$  and  $6^\circ$ , for  $Re = 200$  and taken from DNS simulations using the spectral element method. In comparison with figure 4.1 these points can be identified as being in regions where  $C_y$  initially increasing,  $C_y$  is maximum and  $C_y$  decreases. Note that these data and plots are obtained from the current study for the purpose of providing a better illustration.

As the angle of incidence ( $\theta$ ) increases clockwise from  $2^\circ$  to  $6^\circ$ , it can be clearly observed in figure 2.5 that the bottom shear layer comes closer to the bottom wall of the body compared to the top shear layer. The shear layer nearer to the body creates higher suction compared to the shear layer at the opposite side, as the higher velocity in the shear layer implies a lower pressure, from a simple Bernoulli-type argument. This pressure imbalance between the top and bottom sides of the body creates a downward force which with the sign convention introduced in figure 2.1 is positive. As the angle is further increased to  $\theta = 4^\circ$ , the bottom shear layer comes even closer and therefore the pressure difference becomes greater leading to a higher  $C_y$ . The induced lift force  $C_y$ , becomes maximum when the shear layer near to the wall just reattaches at the trailing edge. As  $\theta$  is further increased at  $\theta = 4^\circ$  (figure 2.5 (b)), the recirculation region formed by the reattachment of the bottom shear layer shrinks in size resulting in a reduction of the velocity near the wall, and therefore an increase in pressure. This implies a reduction of the pressure imbalance between the top and bottom surface leading to the reduction in  $C_y$ . This theory has been discussed in Parkinson (1989). The variation of  $C_y$  vs  $\theta$  is presented in figure 4.1. As the body is connected to an oscillatory system (discussed in section 2.1.1), this shear layer behaviour also harmonizes with the cyclic behaviour of the system providing the driving force to the system so that the motion of galloping is sustained. Even though both galloping and VIV depend on the behavior of the shear layers in either side of the body, Galloping depends on the proximity of the shear layers to body where as VIV depends on the shedding of the vortices. As galloping depends on the force generated as a result of proximity of the shear layers to the body, galloping is dependent on the motion of the body where as VIV is dependent on the vortex shedding. Hence, VIV is dependent on the vortex shedding

frequency and “lock-in” while galloping is present for larger frequencies.

### 2.1.4 Governing parameters of galloping

From the published literature, it is observed from the earlier works such as Parkinson and Brooks (1961); Luo et al. (1994) and more recent studies such as Luo et al. (2003); Barrero-Gil et al. (2010); Joly et al. (2012) that classical VIV parameters have been incorporated to describe galloping. These parameters are the reduced velocity  $U^*$  which is the velocity of the flow normalised by the natural frequency of the system and  $\zeta$  which is the damping ratio based on the linear system in a vacuum. Both these parameters contain a natural structural frequency component. As VIV is a resonant type of phenomenon these parameters are suitable for VIV. However, as galloping is not a resonance-type phenomenon driven by the natural frequency, but a velocity driven phenomenon, these normalisations might not be suitable for galloping. This can be clearly observed in Barrero-Gil et al. (2010). In this study, which is focused on energy harvesting, the power extracted by the system presented using these current parameters does not collapse well. Therefore, it is necessary to formulate new parameters which effectively describe galloping, particularly the energy transfer between the fluid and the body as it is the focus of this study.

### 2.1.5 Frequency response

It is clear that the cyclic motion of the shear layer will harmonize with the mechanical system of a body under the influence of galloping. Therefore, the frequency response should be close to the natural frequency of the system  $\omega_n$  (Païdoussis et al., 2010). This is significantly different from the VIV mechanism, where the primary frequency comes from the periodic forcing of the vortex shedding. Hence, in the QSS model the natural frequency of the system can be identified as the frequency of oscillation. However, it should be noted that this is valid in the regimes where the conditions discussed in section 2.1.2 are satisfied.

The experimental studies carried by Bouclin (1977) concluded at high reduced velocities with large inertia (where the natural frequency is very low), the motion of the body controls the frequency of the system rather than the vortex shedding. The structural damping has no effect provided that it is small. This study also concluded that as the inertia and the reduced velocity get lower, there is some interaction between vortex shedding and galloping.

When this occurs the frequency is mainly governed by vortex shedding.

### 2.1.6 Fluid mechanics governing the galloping response

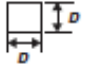
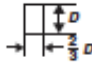
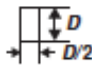

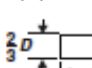
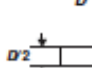
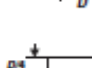


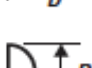


As discussed in subsection 2.1.3 the driving force of a galloping system is the asymmetrical placement of the shear layers at either sides of the body. As a consequence, it is clear that a significant afterbody is needed for the shear layer interaction to sustain galloping. Parkinson (1974, 1989) and Bearman et al. (1987) have discussed well the importance of the length and the shape of the body for galloping in their reviews. It is also highlighted in Parkinson (1974) that the most important physical parameters for galloping are the size relative to the characteristic height and the shape of the afterbody. Manipulating the shape of the afterbody and thereby manipulating the shear layer interactions with the body, gives the ability to control the galloping response.

Blevins (1990) provided a good comparison of the shapes which are prone to galloping based on the work by Parkinson and Brooks (1961), Nakamura and Mizota (1975) and Nakamura and Tomonari (1977). The reproduction of Blevins's data can be found in Païdoussis et al. (2010) and presented in figure 2.6. Here the induced angle is represented by  $\alpha$  and the transverse force coefficient is represented by  $C_{fy}$ . In order for galloping to sustain, the direction of both these quantities should be same and thus have to satisfy the condition of

$$\frac{\partial C_{fy}}{\partial \alpha} > 0 \quad (2.6)$$

Naudascher and Wang (1993), Ruscheweyh et al. (1996), Deniz (1997) and Weaver and Veljkovic (2005) also provide data on different cross sectional shapes. Alonso et al. (2009) carried out wind tunnel tests on biconvex and rhomboidal cross sections. This study concluded that the galloping stability is dependent on the angle of attack. The aspect ratios where galloping is sustained in these cross sections were identified. Studies were further carried out by Alonso for elliptical cross sections (Alonso et al., 2010) which concluded that galloping is Reynolds number dependent for elliptical cross sections. The study of triangular cross sections carried out by (Alonso et al., 2005) isolated the angles of attack where galloping is sustained. The regions of stability for galloping at different angles of attack and the static force coefficients are presented in these studies with regards to the

## 2. A REVIEW OF THE LITERATURE

Section	$h/d$	$\partial C_{Fy}/\partial \alpha$		Reynolds number
		Smooth flow	Turbulent flow <sup>b</sup>	
	1	3.0	3.5	$10^5$
	3/2	0.	-0.7	$10^5$
	2	-0.5	0.2	$10^5$
	4	-0.15	0.	$10^5$
	2/3	1.3	1.2	$6.6 \times 10^4$
	1/2	2.8	-2.0	$3.3 \times 10^4$
	1/4	-10.	-	$2 \times 10^3 - 2 \times 10^4$
 (Thin airfoil)	- <sup>c</sup>	-6.3	-6.3	$> 10^3$
	-	-6.3	-6.3	$> 10^3$
	-	-0.1	0.	$6.6 \times 10^4$
	-	-0.5	2.9	$5.1 \times 10^4$
	-	0.66	-	$7.5 \times 10^4$

<sup>a</sup>  $\alpha$  is in radians; flow is left to right.  $\partial C_{Fy}/\partial \alpha = -\partial C_L/\partial \alpha - C_D$ , with  $C_{Fy}$  based on the dimension  $D$ , so that  $\partial C_{Fy}/\partial \alpha > 0$  for galloping.  
<sup>b</sup> Approximately 10% turbulence.  
<sup>c</sup> Inappropriate to use  $h/d$ .

Figure 2.6: “The transverse force coefficient for various sections in steady smooth or turbulent flow (after Blevins (1990))” obtained from Païdoussis et al. (2010). Here the induced angle is represented by  $\alpha$  and the transverse force force coefficient is represented by  $C_{fy}$ . In order for galloping to sustain, the direction of both of these quantities should be same and thus have to satisfy the condition of  $\frac{\partial C_{fy}}{\partial \alpha} > 0$

cross section involved. Luo et al. (1994) carried out an interesting study where the influence of the afterbody on galloping was investigated. The sides of a square section was chamfered gradually delaying the shear layer re-attachment, and two trapezoidal cross sections and one isosceles triangle was obtained. The  $C_y$  vs.  $\theta$  plots revealed that the maximum value of  $C_y$  increased as the chamfering angle increased (i.e when the cross section was transformed from a square to a isosceles triangle). Another interesting observation was that the incident angle where maximum  $C_y$  occurred increased as the chamfering angle increased. Inhibition of the shear layer reattachment leads to higher  $C_y$  at higher induced angles which leads to higher induced velocities.

The power transfer from fluid to the body can be defined as,

$$P_m = \frac{1}{T} \int_0^T F_y \dot{y} dt, \quad (2.7)$$

From equation 2.7 it can be seen that power transfer could be increased by increasing either  $F_y$  or  $\dot{y}$  or both. From observations of Luo et al. (1994) it can be seen that inhibition of shear layer reattachment will lead to higher  $F_y$  occurring at higher induced velocities, which is beneficial for energy harvesting because as shown in equation 2.7, power is a function of both  $F_y$  and the velocity of the body. Kluger et al. (2013) concluded that the best cross sectional shape for their "vibro-wind" energy harvester was a trapezoidal cross section. However, this study has not revealed the underpinning fluid mechanics in detail such as the behaviour of the shear layers which makes an optimum cross section.

While many of these previous studies have investigated the influence of different body shapes on the galloping response, very few have systematically varied the shape of the body with the aim of deliberately amplifying the galloping. If galloping is to be used as an energy harvesting mechanism, finding an optimum body shape which produces large transverse velocities is desirable.

### 2.1.7 Galloping as a mechanism of energy harvesting

The focus of fluid-elastic galloping research in the past was on understanding and developing methods to suppress it, due to the adverse effects on civil structures. However, recently the focus of research has been redirected to develop mechanisms to excite galloping rather than suppressing it. This is due to the recent demand for alternative energy sources with minimal



## 2. A REVIEW OF THE LITERATURE

---

environmental impact. Thus, this demand for alternative energy has lead researchers to develop ways of extracting useful energy from flow induced vibrations.

Bernitsas and his group in the University of Michigan have made significant progress on using VIV as potential candidate for energy extraction. Bernitsas et al. (2008) introduced the concept of using VIV as a mode of energy extraction. The group have developed a device called VIVACE converter based on this concept. The work has been further expanded to focus on various aspects (such as Reynolds number effects, damping effects etc.) in Bernitsas et al. (2009); Raghavan et al. (2009); Raghavan and Bernitsas (2011); Lee et al. (2011). This group has studied extensively on the effect of the mechanical parameters, the Reynolds number effects and the bottom boundary conditions of the VIVACE converter in order to obtain efficient energy output using VIV as an energy harvesting mechanism.

In contrast, the research carried out investigating the possibility of energy harvesting using fluid-elastic galloping is quite limited. Barrero-Gil et al. (2010) conducted the pioneering study on energy harvesting using fluid-elastic galloping. The key consideration investigated in this study was that unlike VIV, fluid-elastic galloping is not dependent on a synchronisation or a “lock-in” mechanism. Therefore, it can operate on a wide spectrum of frequencies giving fluid-elastic galloping an advantage over VIV as a mechanism of energy harvesting. The study incorporated the QSS model where the Krylov and Bogoliubov method was used to solve the equation. This study used a  $3^{rd}$  order polynomial rather than a  $7^{th}$  order polynomial for simplification purposes which would have lead to less accurate quantitative results. However, this initial work showed that galloping can indeed used as a candidate for energy harvesting. Vicente-Ludlam et al. (2014) quantitatively showed that there is a link between the optimal electrical load resistance and the flow speed. This study was built on Barrero-Gil et al. (2010) taking the QSS model as the mode of data acquisition. Similar to Barrero-Gil et al. (2010) this study also incorporated a low order  $3^{rd}$  order polynomial for the QSS model which again restricted the quantitative accuracy of the results. Since the work was mainly qualitative, it was identified that the understanding is primary and therefore step-by-step research has to be conducted in order to properly understand the link between energy transfer in the galloping mechanism and an experimental prototype should be developed to test the engineering performance.

Kluger et al. (2013) from Cornell university have produced a prototype called “Vibro-

wind” energy harvester which essentially uses the galloping mechanism. The mechanism used here differ slightly from the traditional transversely oscillating body, where the oscillating body is connected with a cantilevered beam. Thus, there is both translational and rotational motion in the system. It was concluded that the amplitude of the galloping oscillator which couples the rotational motion with the translational motion was always less than the amplitude of a body under a pure translational motion. As the present study is focused on theoretical aspects of the energy transfer, motion of the body is kept purely translational.

### 2.1.8 Review summary and statement of objectives

It is clear that more investigations should be carried out on energy transfer of a galloping system, particularly to develop efficient energy harvesting systems. More fundamental research is needed to explore the underpinning effects of mechanical and fluid dynamic parameters influencing the energy transfer of a galloping system to fill the gaps of the existing knowledge base. Thus, the objectives of the current research, spread over two phases, are defined as follows.

#### **Phase 1: Understand the governing mechanical parameters of the system and isolate regions of parameter space where a good power transfer can be obtained**

Païdoussis et al. (2010) describes galloping as a “velocity dependent damping controlled phenomenon”. Yet, so far the scaling parameters used in studies are the traditional VIV parameters which are the damping ratio  $\zeta$  and the reduced velocity  $U^*$  (Barrero-Gil et al., 2010) which has a embedded frequency component. Thus the following objectives are defined for this phase

- Formulate a new set of scaling parameters based on the natural time-scales of the system.
- Investigate the influence of these parameters on mean power transfer.
- Isolate the regions where high power transfer can be obtained.

- Investigate the relationship between these new scaling parameters and the frequency response of the system.

### **Phase 2: Understand the fluid mechanics of the system and optimise and control these mechanics to obtain a higher power transfer**

Luo et al. (1994) showed that inhibition of shear layer reattachment can lead to higher peak  $F_y$  at higher induced angles and therefore higher transverse velocities. Thus, from equation 2.7, it can be hypothesised that a higher mean power can be obtained by inhibition of the shear layer reattachment. Hence, the following objectives were defined for phase 2.

- Obtain QSS power data by systematically delaying the shear layer and investigate the influence on power.
- Identify the relationship between the flow structures and the mean power output through analysis of the flow-field.
- Provide design considerations for a galloping energy extraction system based on passive control of the shear layers.

The stated aims are addressed by the following sections. Objectives of phase 1 are addressed in chapter 4. A new set of scaling parameters namely the combined mass stiffness  $\Pi_1$  and the combined mass damping  $\Pi_2$  are formulated from the linearised QSS model. The power data is obtained from numerically solving the QSS model and direct numerical simulations are presented through the new parameters and compared against the classical VIV parameters. Furthermore, an expression for the frequency of the system is formulated in terms of  $\Pi_1$  and  $\Pi_2$ . The data obtained through this model are compared against data acquired through QSS model and DNS.

Chapter 5 addresses the objectives of phase 2, where the possibility of achieving higher power transfer through the inhibition of shear layer reattachment is investigated. The inhibition of the shear layer reattachment is achieved by altering the afterbody of the square cross section. The mean power data of these cross sections obtained using the QSS model and DNS are analysed and compared. Key regions of the  $C_y$  vs.  $\theta$  curve which significantly influences the power transfer are analysed and compared. Through this

comparison, design considerations for an efficient galloping energy harvesting system are discussed.

## CHAPTER 3

---

# METHODOLOGY AND VALIDATION

### 3.1 Introduction

An overview of the modeling and the computational methods used in this study are presented in this chapter. This study uses well established techniques to model and study fluid elastic galloping. Therefore, only a brief overview is provided together with relevant references where the development and vigorous validation has been presented.

This chapter is presented in the following order. The equations used to model the system are presented and discussed. Next, a brief discussion of the techniques used for direct numerical simulations are presented, followed by the problem formulation and the discussion of the parameters used. Finally, validation data are presented and discussed to demonstrate the accuracy of the direct numerical simulations.

#### 3.1.1 Parameters used

The findings in this study are presented in two categories i.e. high and low Reynolds numbers, so as to study the system at laminar and turbulent flow regimes. One of the main objectives in this study is to capture the essential flow physics which governs galloping accurately through direct numerical simulations. Detailed data could be obtained on sensitive parts of the flow-field such as the shear layer through by computational methods, in particular Direct Numerical Simulation (DNS) compared to experimental methods. However, DNS becomes computationally intractable at high Reynolds number. Thus, a major

portion of the study was carried out in the laminar range where the flow is laminar and two dimensional. It is possible to carry out 3-dimensional simulations at the turbulent regions. However, this demands a large number of nodes (in the range of millions) and a longer computational time (in the range of months for a single simulation) to gain an accurate result and thus, the laminar 2-dimensional regime was selected.

A second modelling technique employed is the numerical integration of a low-order, but nonlinear, equation of motion derived using a quasi-static assumption (Parkinson and Smith, 1964). This model only requires force data obtained from static body simulations or experiments. Therefore, although a majority of the study is focused on the low Reynolds number regime, some results are presented using inputs from published data at high Reynolds numbers to this low order model to provide a comparison between high and low Reynolds number cases.

One crucial factor is the selection of a suitable Reynolds number for the “low” Reynolds number regime for the simulations to be valid. Studies by Tong et al. (2008) and Sheard et al. (2009) reveal that the approximate value of 3-dimensional transition of the wake for a stationary square cross section is  $Re = 160$ . Barrero-Gil et al. (2010) concluded that a high value of  $a_1$  or the initial gradient of the  $C_y$  vs.  $\theta$  curve should be high to gain an efficient energy harvesting through galloping. Joly et al. (2012) showed that this gradient is significantly higher at  $Re = 200$  compared to  $Re = 160$ . Furthermore, Leontini et al. (2007) concluded that the oscillation of the bluff body essentially stabilizes the wake, for example the the limit of three-dimensional transition of an oscillating circular cylinder can be as high as  $Re = 280$ , compared to the transition Reynolds number of  $Re \simeq 190$  for a stationary cylinder. As the essential flow physics such as the formation of the Kàrmàn vortex street is common for both a circular and square bluff body, it can be assumed that the wake is also stabilised for oscillating square cross sections. Thus,  $Re = 200$  was selected as the Reynolds number for the “low” Reynolds number region as a compromise between keeping the flow strictly two-dimensional, and providing a high enough lift to generate vigorous galloping.

$Re = 22300$  was defined as the “high” Reynolds number in this study, which matches the pioneering study of galloping by Parkinson and Smith (1964). Therefore, the aerodynamic data for a stationary square section at this Reynolds number was obtained from the

literature as input to the QSS model. For the high  $Re$  tests, predictions of power output were obtained using the coefficients of the  $C_y$  vs.  $\theta$  curve from Parkinson and Smith (1964) as inputs to the QSS model. Stationary  $C_y$  data at different angles of attack used as inputs to the QSS model were obtained for the low Reynolds number regime using direct numerical simulations.

The average power was obtained by using equation 3.1, and the averaging was done over no less than 20 galloping periods. The mass ratio  $m^*$  was kept at 1163 for  $Re = 22300$  (Similar to Parkinson and Smith (1964)). Considering previous studies (Robertson et al., 2003; Joly et al., 2012)  $m^*$  was kept at  $m^* = 20$  which was a level of inertia not so high as to suppress galloping and not so low for vortex shedding to dominate and weaken galloping as observed by Joly et al. (2012). The reduced velocity  $U^*$  was kept  $U^* \geq 40$  to keep the natural frequency of the system far from the frequency of vortex shedding to ensure that the primary mode of flow-induced vibration was galloping as opposed to vortex-induced vibration (VIV). These parameters were used throughout this study unless specified otherwise.

## 3.2 Quasi-steady model

The quasi-steady state model discussed in section 2.1.2 was used to obtain oscillator response data. The quasi-steady state model has proven its ability to obtain accurate galloping response data (as also discussed in section 2.1.2). Therefore, a large number of cases can be modelled in a small amount of computational time. The oscillator equation consists of a spring, mass and damper oscillator expression with a 7<sup>th</sup> order interpolation polynomial in terms of the body velocity (or equivalently, the instantaneous incidence angle) as the forcing function (equation 2.5), obtained from a curve fit of aerodynamic data (i.e.  $C_y$  as a function of the incidence angle).

### Solving the quasi-steady state equation

The quasi-steady model being an ordinary differential equation can be solved using different solving methods. Vio et al. (2007) showed that numerical integration provides accurate data, and this technique is employed here. A fourth-order Runge-Kutta ODE solving

scheme was used in solving the quasi-steady state oscillator equation. The built in ‘ode45’ function in MATLAB was used primarily to solve the QSS equation while in some cases ‘ode15s’ function was used when the equation became more stiff.

### 3.3 Calculation of average power

The ideal potential amount of harvested power output is represented as the dissipated power due to mechanical damping before losses in any power take-off system are included. Thus the mean power output can be expressed as

$$P_m = \frac{1}{T} \int_0^T (cj)\dot{y}dt, \quad (3.1)$$

where  $T$  is the period of integration and  $c$  is the mechanical damping constant.

The work done on the body by the fluid is equal to this quantity, defined as

$$P_m = \frac{1}{T} \int_0^T F_y \dot{y}dt, \quad (3.2)$$

where  $F_y$  is the transverse (lift) force.

The two definitions of the mean power provide two vital interpretations of power transfer. Equation 3.1 shows that the power is proportional to the mechanical damping and the magnitude of the transverse velocity. At first glance one may assume that the power can be increased by increasing damping. In a practical power extraction device, the significant component of damping would be due to the electrical generator and therefore, an increase in damping would be due to the increase of the load or electrical resistance. Yet this perception of damping is not quite accurate as very high damping would result in reducing the velocity amplitude which then would not result in a higher energy output according to equation 3.1. In consequence, a balance needs to be struck where the damping is high, but not to the extent that it will affect power output adversely by overly suppressing the motion of the body.

On the other hand, equation 3.2 shows that a higher power is attained during situations where the transverse force  $F_y$  and the transverse velocity are in phase. Hence, a simple increase in the magnitude of the force or the velocity is not satisfactory to attain a higher power transfer. A higher power output can be obtained when there is a smaller phase difference between the force and the velocity.



#### 3.4 Direct numerical simulations (DNS)

Direct numerical simulations were employed to obtain the stationary data to be used as inputs to the QSS model and to obtain fluid-structure interaction (FSI) predictions to be compared with the QSS model at low Reynolds numbers. A high-order spectral element code which simulates two-dimensional laminar flows was used to obtain the DNS data. This code essentially solves the Navier-Stokes equations in an accelerated reference frame that accelerates with the body. A three-step time-splitting scheme also known as a fractional step method was used for temporal discretisation. A predictor-corrector method was used for the FSI data where an elastically mounted body was involved. A description of the spectral element method in general can be found in Karniadakis and Sherwin (2005). This code has been very well validated in a variety of fluid-structure interaction problems similar to that studied in the current study (Leontini et al., 2007; Griffith et al., 2011; Leontini et al., 2011; Leontini and Thompson, 2013). An overview of the algorithm is presented in the following subsections which is described in detail by Leontini (2007).

##### 3.4.1 Governing equations

In this study, the following key assumptions were made to carry out the direct numerical simulations.

- To formulate the differential equations to an infinitesimally small fluid section, the fluid was assumed to be a continuum. This assumption is valid for all macro flows as is the case in this study.
- To avoid the modelling acoustic wave propagation, it was assumed that the density of the fluid is constant. The fluid is incompressible. This particular assumption is usually valid for Mach numbers (ratio of the speed of sound to the speed of fluid flow ) less than 0.3.
- The fluid was assumed to be a Newtonian fluid, which means that the shear stress is directly proportional to the strain rate.

The assumptions used are quite standard and further information can be found in White (1999).

These assumptions lead to the Navier-Stokes equations as the equations which govern the motion of a Newtonian, incompressible fluid.

$$\frac{\partial \mathbf{u}}{\partial t} + (\mathbf{u} \cdot \nabla) \mathbf{u} = -\frac{\nabla p_f}{\rho} + \frac{\mu_v}{\rho} (\nabla^2 \mathbf{u}) , \quad (3.3)$$

and continuity,

$$\nabla \cdot \mathbf{u} = 0 . \quad (3.4)$$

The velocity vector field is represented by  $\mathbf{u}$ , time by  $t$ , the pressure field by  $p_f$ , fluid density by  $\rho$  and the dynamic viscosity by  $\mu_v$ . In the Navier-Stokes equation (3.3) the left hand side represents the inertial forces and the right hand side represents the forces from pressure and viscous stresses. The net mass flux into the fluid element is specified to be zero by the continuity equation (3.4).

These equations are generalised by non-dimensionalisation. In the case of bluff body wake flows, the equations are typically non-dimensionalised by using the characteristic length of the body i.e the frontal projected height  $D$ , and the free-stream velocity  $U$ .

For cases investigating fluid structure interactions the equations are modified to be solved in an accelerated reference frame. The frame of reference is attached to the body. Therefore, an extra term is added to the Navier-stokes equations which represents the acceleration of the body. Thus, the equations can be written as,

$$\frac{\partial \mathbf{V}}{\partial \tau} = -\nabla P + \frac{1}{Re} (\nabla^2 \mathbf{V}) - (\mathbf{V} \cdot \nabla) \mathbf{V} + \frac{d\mathbf{V}_{body}}{d\tau} , \quad (3.5)$$

$$\nabla \cdot \mathbf{V} = 0 . \quad (3.6)$$

The non dimensional terms are defined as follows:  $\mathbf{V} = \mathbf{u}/U$ ,  $\tau = tU/D$ ,  $P = p_f/(\rho U^2)$ ,  $Re = \rho U D/(\mu_v)$  and  $\mathbf{V}_{body} = \mathbf{v}_{body}/U$ , and  $\mathbf{v}_{body}$  being the velocity of the body.  $\frac{d\mathbf{V}_{body}}{d\tau}$ , represents acceleration of the body, or  $\ddot{y}$ .

The Navier-Stokes equations are coupled with the oscillator differential equation

$$\frac{\ddot{y}_{cyl}}{D} + 2\zeta \sqrt{k^*} \frac{\dot{y}_{cyl}}{D} + k^* \frac{y_{body}}{D} = \frac{\pi C_L}{2 m^*} , \quad (3.7)$$

Where  $\zeta$  is the damping ratio,  $k^* = kD^2/mU^2$  and  $C_L = F_{lift}/(0.5\rho U^2 D)$ . The lift coefficient per unit length of the body is  $C_L$ , the transverse displacement of the body is given by  $y_{body}$ , the characteristic length scale of the body is  $D$ ,  $k$  is the spring constant and

the mass per unit length of the body is represented by  $m$ . The general form of this linear oscillator equation can be found in books such as Naudascher and Rockwell (1994). The final form of the coefficients were constructed by non-dimensionalising the general linear oscillator equation.

#### 3.4.2 Temporal discretisation: Time-splitting

The problem was discretised in order to solve equations 3.5, 3.6 and 3.7 in both space and time. A three-step time splitting method was used for the temporal discretisation. This scheme, also known as the fractional step method, was used to separately integrate the terms in the right hand side of the Navier-Stokes equation (Karniadakis and Sherwin, 2005). The overall integration of one time-step is split into three substeps. An approximate solution of the Navier-Stokes equation is gained by this scheme.

The body acceleration, along with the convective acceleration terms, is integrated through the whole time step in order to obtain an initial approximation of the intermediate velocity field. This velocity field is used as the initial condition for the integration of the pressure. A secondary intermediate velocity field is obtained as a result of this pressure integration substep. This secondary velocity field is then used as the starting condition for the integration of the diffusion term which results in the final velocity field.

The three semi-discretised substep equations are as follows:

$$\mathbf{V}^* - \mathbf{V}^{(n)} - \Delta \mathbf{V}_{body} = - \int_{\tau}^{\tau+\Delta\tau} (\mathbf{V} \cdot \nabla) \mathbf{V} d\tau \quad (3.8)$$

$$\mathbf{V}^{**} - \mathbf{V}^* = - \int_{\tau}^{\tau+\Delta\tau} \nabla P d\tau \quad (3.9)$$

$$\mathbf{V}^{(n+1)} - \mathbf{V}^{**} = \frac{1}{Re} \int_{\tau}^{\tau+\Delta\tau} \nabla^2 \mathbf{V} d\tau, \quad (3.10)$$

The current time step is represented by  $n$  and the intermediate velocity fields at the end of the convection and pressure substeps are  $\mathbf{V}^*$  and  $\mathbf{V}^{**}$  respectively. The change in the body velocity over a time step is given by  $\Delta \mathbf{V}_{body} = \int_{\tau}^{\tau+\Delta\tau} \frac{d\mathbf{V}_{body}}{d\tau} d\tau$ .

The addition of these three substep equations reduces to the integrated form of the Navier-Stokes equation in equation 3.5.

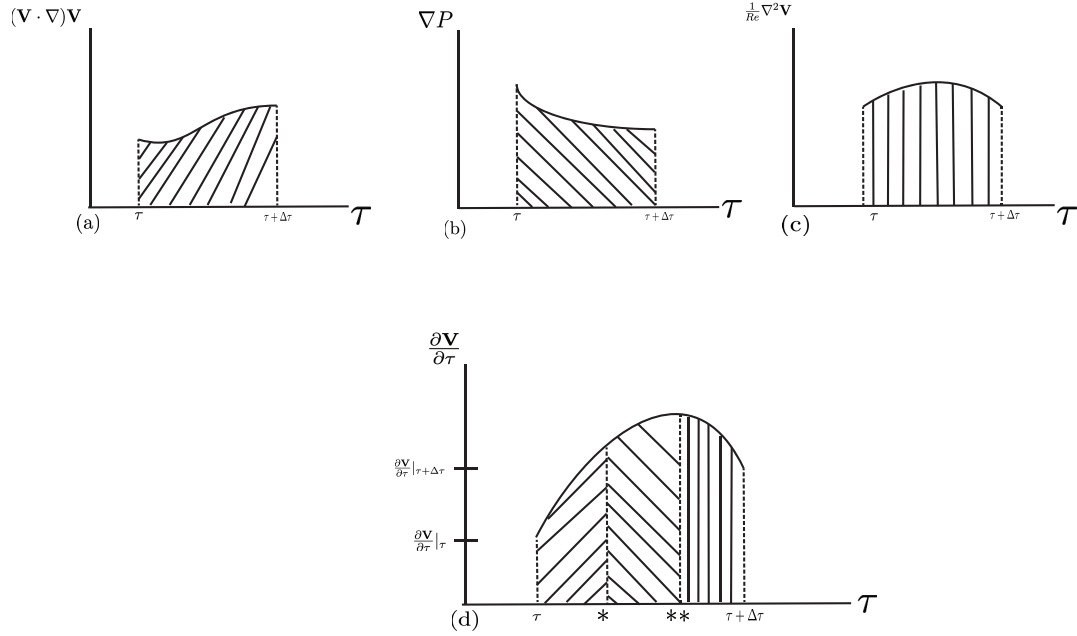


Figure 3.1: Sketch of the integration of the time splitting scheme. (a), (b) and (c) represents the convection pressure and diffusion sub steps. The intermediate time steps are represented by  $(*)$  and  $(**)$

Figure 3.1 (a), (b) and (d) show an illustration of the integration sub steps presented in equations 3.8, 3.9 and 3.10. The overall integration of the three sub-steps is illustrated in figure 3.1 (d), which is the addition of equations 3.8, 3.9 and 3.10.

### Integration of the substep equations

The integration methods of the pressure, convection and diffusion sub steps are presented in this subsection.

#### The convection substep

As the system involves free oscillation, a coupling between the oscillation equation (equation 3.7) and the Navier-Stokes equations had to be employed. As a result, the body dynamics had to be solved at each time-step.

An iterative predictor-corrector scheme was employed to obtain the solution of the coupled equations. The initial iteration being the “predictor” step was obtaining approximations for all the quantities involved in the integration. A quadratic extrapolation was used to obtain an initial estimate of  $\Delta \mathbf{V}_{body}$  from three previous time step values of  $\mathbf{V}_{body}$ . Therefore, a non-dynamical approximation can be obtained.

$$\mathbf{V}_{body}^{(n+1)\dagger} = 3\mathbf{V}_{body}^{(n)} - 3\mathbf{V}_{body}^{(n-1)} + \mathbf{V}_{body}^{(n-2)} , \quad (3.11)$$

The dagger ( $\dagger$ ) indicates that the value is an initial approximation eg.  $\mathbf{V}_{body}^{(n+1)\dagger}$ . Thus,  $\Delta \mathbf{V}_{body}^\dagger$  was obtained by a simple subtraction of the value at the current time step.

The approximated position of the body at the next time step can be obtained by carrying out an integration of the body velocity over the time step. A third-order Adams-Moulton method was used to perform the integration. Therefore, the final equation describing the position of the body is given by,

$$\frac{y_{body}^{(n+1)\dagger} - y_{body}^{(n)}}{\Delta \tau} = \frac{1}{12}(5\mathbf{V}_{body}^{(n+1)\dagger} + 8\mathbf{V}_{body}^{(n)} - \mathbf{V}_{body}^{(n-1)}) . \quad (3.12)$$

The transverse displacement of the body is denoted by  $y_{body}$ .

In order to obtain an approximation for  $\mathbf{V}^*$ , a solution was obtained for equation 3.8 using the previous approximated quantities.

By using a third-order Adams-Bashforth scheme and incorporating the approximation of equation 3.11 for  $\Delta \mathbf{V}_{body}^\dagger$  the first approximation for  $\mathbf{V}^*$  was obtained using the equation,

$$\frac{\mathbf{V}^* - \mathbf{V}^{(n)} - \Delta \mathbf{V}_{body}^\dagger}{\Delta \tau} = \frac{1}{12}(23\mathbf{N}(\mathbf{V})^{(n)} - 16\mathbf{N}(\mathbf{V})^{(n-1)} + 5\mathbf{N}(\mathbf{V})^{(n-2)}) . \quad (3.13)$$

The explicit integration method was only used for the first approximation and for the subsequent iterations a semi-implicit method was used for  $\mathbf{V}^*$ .

This step was followed by solving the remaining substep equations in order to obtain an approximation for  $\mathbf{V}^{(n+1)\dagger}$ , and then the “predictor” portion of the predictor-corrector method was completed.

The body velocity approximation  $\mathbf{V}_{body}^\dagger$ , was updated commencing the “corrector” cycle of the predictor-corrector method. This was carried out using a third-order integration scheme.

$$\frac{\mathbf{V}_{body}^{(n+1)\dagger} - \mathbf{V}_{body}^{(n)}}{\Delta\tau} = \frac{1}{24}(25\ddot{y}_{cyl}^{(n+1)} - 2\ddot{y}_{cyl}^{(n)} + \ddot{y}_{cyl}^{(n-1)}) . \quad (3.14)$$

$\Delta\mathbf{V}_{body}^\dagger$  was updated using the recalculated value of  $\mathbf{V}_{body}^{(n+1)\dagger}$ . The velocity was integrated over a time step in order to obtain the position of the body. For the first correction cycle a third order Adams-Moulton method was used which completed the first iteration of the predictor-corrector method.

$$\frac{y^{(n+1)\dagger} - y^{(n)}}{\Delta\tau} = \frac{1}{12}(5\mathbf{V}_{body}^{(n+1)\dagger} + 8\mathbf{V}_{body}^{(n)} - \mathbf{V}_{body}^{(n-1)}) , \quad (3.15)$$

Slight modifications were employed to the subsequent iterations in order to improve numerical stability. However, the iterations proceeded in a similar manner. As the approximations for  $\Delta\mathbf{V}_{body}^\dagger$  and  $\mathbf{V}^{(n+1)\dagger}$  were available, further correction steps were carried out using third-order Adams-Moulton scheme .

$$\frac{\mathbf{V}^* - \mathbf{V}^{(n)} - \Delta\mathbf{V}_{body}^\dagger}{\Delta\tau} = \frac{1}{12}(5\mathbf{N}(\mathbf{V})^{(n+1)\dagger} + 8\mathbf{N}(\mathbf{V})^{(n)} - \mathbf{N}(\mathbf{V})^{(n-1)}) . \quad (3.16)$$

The two remaining substeps were then solved to obtain a new approximation of  $\mathbf{V}^{(n+1)\dagger}$ .

The first correction step was carried out by employing 3.14 to obtain a second estimate for the velocity of the body  $\mathbf{V}_{body}^{(n+1)\ddagger}$ . A relaxation equation (equation 3.17) was used for the velocity of the body prior to using equation 3.15 since the equations were quite stiff.

$$\mathbf{V}_{body}^{(n+1)'} = \mathbf{V}_{body}^{(n+1)\dagger} + \epsilon(\mathbf{V}_{body}^{(n+1)\ddagger} - \mathbf{V}_{body}^{(n+1)\dagger}) , \quad (3.17)$$

$\mathbf{V}_{body}^{(n+1)\ddagger}$  and  $\mathbf{V}_{body}^{(n+1)\dagger}$  represent the most current and previous approximations respectively. The under relaxation parameter is represented by  $\epsilon$  which controls the proportion of the correction which is considered in each iteration. The final approximation at the

### 3. METHODOLOGY AND VALIDATION

---

end of the relaxation process is represented by  $\mathbf{V}_{body}^{(n+1)'}$  and was used in equation 3.15 for completing the correction cycle and hence, the iteration.

A set of convergence criteria were specified until which the iteration was continued. The lift force of the body, the velocity of the body and the fluid velocity were required to converge to the required convergence criteria. A series of convergence studies were carried out in order to obtain the convergence criteria (Pregalato, 2003). The solution converged typically within 3 – 4 iterations and the iteration count exceeded 10 only in very rare cases.

The procedure to obtain the solution for  $\mathbf{V}^*$  (velocity field at the end of the convection substep) in a nutshell is as follows. A predictor-corrector method was employed, where the primary predictor cycle was first employed. This was followed by obtaining an approximation for  $\Delta\mathbf{V}_{body}$  which was calculated using equation 3.11. From this approximation ( $\Delta\mathbf{V}_{body}$ ) the position of the body was approximated using equation 3.12.

Next, using an explicit Adams-Bashforth scheme, an approximation was obtained for  $\mathbf{V}^*$  by solving the substep equation (equation 3.13). The predictor cycle was completed by solving the remaining substep equations to arrive at the first approximation of  $\mathbf{V}^{(n+1)}$ .

Then, the primary corrector step was initiated by calculating the forces of the body from the current approximation of  $\mathbf{V}^{(n+1)}$ . Using these forces together with the current approximations of the velocity and the displacement of the body and the equation of motion of the body (eq:3.7) an approximation for the acceleration of the body at the end of the timestep was obtained. By integrating this acceleration over the timestep using equation 3.14 the corrected approximation of  $\Delta\mathbf{V}_{body}$  was obtained. Using equation 3.15 the corrected approximation for  $y_{body}^{(n+1)}$  was obtained by integrating the velocity over a timestep and using the recent value of  $\Delta\mathbf{V}_{body}$ . The primary corrector step and the primary iteration was completed once this step was completed. All the remaining iterations were carried out in a similar manner with an under relaxation presented in equation 3.17.

#### **The pressure substep**

The pressure equation was solved in two parts in order to find solutions to the two unknowns i.e. the pressure field and the velocity field at the end of the timestep.

The integration of the pressure substep was initiated by formulating equation 3.9 in terms of a second-order Adams-Moulton scheme which gives,

$$\frac{\mathbf{V}^{**} - \mathbf{V}^*}{\Delta\tau} = -\frac{1}{2}(\nabla P^{(n+1)} + \nabla P^{(n)}) . \quad (3.18)$$

The equation was further reduced by considering that the *RHS* is equal to  $\nabla P^{(n+1/2)}$ . The divergence of equation 3.18 was taken. Using equation 3.6, continuity was applied to the velocity field at the end of the pressure substep which resulted in the pressure field having a Poisson equation of the form of

$$\nabla^2 P^{(n+\frac{1}{2})} = \frac{1}{\Delta\tau} \nabla \cdot \mathbf{V}^* . \quad (3.19)$$

This equation can be solved at the middle of the timestep for the pressure field. Therefore, this pressure field can then be back-substituted to equation 3.18, together with the simplified *RHS*, to solve for the velocity field  $\mathbf{V}^{**}$ , at the end of the substep.

### The diffusion substep

Numerical stability of the solution scheme has to be considered for the diffusion substep although the equation for diffusion is linear. Therefore, the Crank-Nicholson scheme or the second order Adams-Moulton scheme which is a semi-implicit scheme and unconditionally numerically stable is employed. Thus this formulates the final equation (eq 3.10) of the time splitting scheme as,

$$\frac{\mathbf{V}^{(n+1)} - \mathbf{V}^{**}}{\Delta\tau} = \frac{1}{2Re}(\nabla^2 \mathbf{V}^{(n+1)} + \nabla^2 \mathbf{V}^{(n)}) . \quad (3.20)$$

The integration over the timestep is obtained from the solution of this equation for  $\mathbf{V}^{(n+1)}$ , thus completing the time splitting scheme and the timestep.

### Spatial discretisation: Spectral element method

The spatial discretisation was done using a nodal based spectral-element method. This method is a member of the finite-element class. The computational domain is separated into a series of macro elements and then a continuous solution is obtained over each element. Mesh refinement can be done in the areas where high gradients are experienced, which is also known as *h*-refinement. It was necessary that all elements to be quadrilateral. Yet, the elements were not restricted from having curved sides.



### 3. METHODOLOGY AND VALIDATION

---

The calculation of the residual  $\mathbf{R}$  initiates the solution process. All the terms of the governing equations (the Navier-Stokes equation eq 3.5) were moved to the *LHS*. Thus, the resulting expression is,

$$\frac{\partial \mathbf{V}}{\partial \tau} + \nabla P - \frac{1}{Re}(\nabla^2 \mathbf{V}) + (\mathbf{V} \cdot \nabla) \mathbf{V} - \frac{d\mathbf{V}_{body}}{d\tau} = 0 . \quad (3.21)$$

A trial solution is substituted into equation 3.21. The *RHS* of the equation would be zero if the trial solution is the exact solution of the equation. If the trial solution is not the exact solution but an approximation to the exact solution which is the case in general, then the *RHS* will be non-zero and a residual will be formed. This residual can be defined by,

$$\frac{\partial \mathbf{V}_{trial}}{\partial \tau} + \nabla P_{trial} - \frac{1}{Re}(\nabla^2 \mathbf{V}_{trial}) + (\mathbf{V}_{trial} \cdot \nabla) \mathbf{V}_{trial} - \frac{d\mathbf{V}_{body}}{d\tau} = \mathbf{R} , \quad (3.22)$$

The trial solutions for velocity and pressure fields are  $\mathbf{V}_{trial}$  and  $P_{trial}$  respectively. The error term which is introduced through the trial function is the residual  $\mathbf{R}$ . It is clear from equation 3.22 that the definition of the residual is the governing equation with the trial solution substituted to the true solution.

In order to effectively distribute the error over the domain, the residual has to be weighted in order to minimise the maximum local error. To perform this task the inner product of the residual with a series of weighing functions were taken. The integral of the product of the weighting function and the residual is the inner product of the residual which is set to zero. The method employed here is also commonly known as weighted residual method.

Tensor-product Lagrange polynomials were used for both interpolating trial functions and weighting functions in the DNS carried out in this study. The order of the polynomials  $p$  can be varied from 2 to 14 in order to further improve grid resolution which is also known as  $p$  refinement. This  $p$  refinement coupled with  $h$  refinement leads to a method called  $h - p$  method which is used to improve accuracy (Karniadakis and Sherwin, 2005). The method also can be identified as a Galerkin method as both trial and weighting functions used were from the same family of functions. Fletcher (1984, 1991) provides further details on weighted-residual methods and Galerkin methods.

Lagrange polynomials can be defined as,

$$L_i(\xi) = \prod_{\substack{g=1 \\ g \neq i}}^{p+1} \frac{(\xi - \xi_g)}{(\xi_i - \xi_g)} \quad (3.23)$$

The spatial coordinate is  $\xi$  and the indices of the data points are represented by  $i$  and  $g$  and the number of data points are represented by  $p + 1$ . One of the properties of Lagrange polynomials is that they are equal to unity at the point  $i$  and are zero at all the other points (but not between points). Thus a continuous polynomial which matches the exact values of the velocity at the node point can be obtained when  $L_i$  is multiplied by the velocity at point  $i$  and then summing over all points. The tensor-product polynomials in two dimensions  $N_{q,s}(\xi, \eta)$  can be defined as the product of the Lagrange polynomial in one direction  $L_q(\xi)$ , with that in the other direction,  $L_s(\eta)$ .

The outline of the procedure to find the solution is as follows. The process is initiated by forming the inner product of the residual and the tensor-product Lagrange polynomial weighting function.

This gives the integral

$$\int \int_{\Omega} N_{k,m}(\xi, \eta) \cdot \left[ \frac{\partial \mathbf{V}_{trial}}{\partial \tau} + \nabla P_{trial} - \frac{1}{Re} (\nabla^2 \mathbf{V}_{trial}) + (\mathbf{V}_{trial} \cdot \nabla) \mathbf{V}_{trial} - \frac{d\mathbf{V}_{body}}{d\tau} \right] dx dy = 0, \quad (3.24)$$

The computational domain is represented by  $\Omega$ .  $N_{q,s}(\xi, \eta)$  are the weighting functions as defined in the computational space.

From equation 3.24 it is seen that each term in the equation is multiplied by the weighting function. Thus, the integral is split into components and the process can be carried out in each of the substep equations 3.8, 3.9 and 3.10. For example the discretised equation for 3.13 can be expressed as

$$\begin{aligned} & \frac{1}{\Delta \tau} \int \int_{\Omega} N_{q,s}(\xi, \eta) \cdot (\mathbf{V}_{trial}^* - \mathbf{V}_{trial}^{(n)} - \Delta \mathbf{V}_{body}) dx dy = \\ & \int \int_{\Omega} N_{q,s}(\xi, \eta) \cdot \left( \frac{1}{12} (23\mathbf{N}(\mathbf{V}_{trial})^{(n)} - 16\mathbf{N}(\mathbf{V}_{trial})^{(n-1)} + 5\mathbf{N}(\mathbf{V}_{trial})^{(n-2)}) \right) dx dy. \end{aligned} \quad (3.25)$$

This integral can be broken into components. Hence, the first term of the of the LHS

### 3. METHODOLOGY AND VALIDATION

---

of equation 3.25 can be defined as,

$$\int \int_{\Omega} \mathbf{V}_{trial}^* N_{q,s}(\xi, \eta) dx dy . \quad (3.26)$$

The first term in equation 3.13 can be used as an example to illustrate the process of obtaining the solution using the spectral element method. In order to calculate the integral of equation 3.26 over the entire computational domain, the integral is evaluated over each element separately. After that, the contributions of each element are summed together.

All the quadrilateral elements are mapped to a square ranging between  $-1$  to  $1$  in both directions where  $\xi$  and  $\eta$  are the orthogonal coordinates of this square. The approximation of the integral is simplified by defining the internal node points as the points used for Gauss-Lobatto-Legendre (GLL) quadrature.

A Jacobian is introduced to perform this coordinate transformation and hence, the integral over each element becomes,

$$\int \int_{El} \mathbf{V}^* N_{q,s}(\xi, \eta) \mathbf{J}(\xi, \eta) d\xi d\eta , \quad (3.27)$$

The Jacobian is represented by  $\mathbf{J}$  and “ $El$ ” denotes that the integration is performed over a single element. The solution of equation 3.27,  $\mathbf{V}_{trial}^*$ , can be re-written as a summation of Lagrange polynomial components. This equation also expresses the tensor-product Lagrange polynomials representing the weighting functions in directions of  $\xi$  and  $\eta$ . Therefore, the equation can be expressed as,

$$\int \int_{El} \sum_{i,j} \widehat{\mathbf{V}}^*_{L_i(\xi)L_j(\eta)} L_q(\xi)L_s(\eta) \mathbf{J}(\xi, \eta) d\xi d\eta . \quad (3.28)$$

The velocity in the nodal points are represented by  $\widehat{\mathbf{V}}^*$ ,  $L$  is the one-dimensional Lagrange polynomial and  $i$  and  $j$  represent the node index in directions  $\xi$  and  $\eta$ .

The Gauss-Lobatto Legendre (GLL) quadrature can be used to obtain an approximation to the integral in equation 3.28, taking the definition of the location of the internal points in the computational domain. Thus approximation of 3.28 can be expressed as,

$$\sum_{a,b} W_{a,b} \sum_{i,j} \widehat{\mathbf{V}}^*_{i,j} L_i(\xi_a)L_j(\eta_b)L_q(\xi_a)L_s(\eta_b) \mathbf{J}(\xi_a, \eta_b) . \quad (3.29)$$

$W_{a,b}$  represents the weighting coefficients for GLL quadrature,  $a$  and  $b$  represent the position of the node in the directions  $\xi$  and  $\eta$  respectively.

Even though equation 3.29 appears to be quite intimidating to deal with, the expression can be considerably simplified because of the fact that the system is discrete and only the values at the nodal points are considered. Since for the Lagrange polynomials

$$\mathbf{L}_i(\xi_a) = \delta_{ia} = \begin{cases} 1 & i = a \\ 0 & i \neq a \end{cases} . \quad (3.30)$$

where  $\delta_{ia}$  is the Kronecker delta. This substitution leads to a significant reduction of the non-zero elements in the simulation and leads to a much simpler expression. If the convection substep (example considered here) is considered, only a single term remains based on the  $\mathbf{V}^*$  term in the convection substep equation which is,

$$W_{q,s} \mathbf{J}(\xi_q, \eta_s) \widehat{\mathbf{V}}_{q,s}^* . \quad (3.31)$$

All the governing terms can be simplified similarly and this process is repeated over all elements. A global matrix is assembled by collecting the contribution of each element and then this matrix system is solved to obtain solutions for the unknown velocity and pressure fields at the nodal points.

Only the continuity of each function is required across the boundaries, with no condition imposed on the gradient (this condition is known as  $C_0$  continuity), even though the shape functions are higher-order polynomials within each element. It can be shown that the method achieves global exponential convergence (Karniadakis and Sherwin, 2005).

The numerical process used for this study has been demonstrated to give exponential spatial convergence as the number of internal nodes per element is increased (Thompson et al., 1996).

A Neumann condition for the pressure was applied at all the boundaries except the outlet. The condition specified the normal gradient of the pressure, the value of which was calculated from the Navier–Stokes equations (Gresho and Sani, 1987). A Dirichlet condition for the pressure ( $p = 0$ ) was enforced at the outlet. The details of the method can be found in Thompson et al. (2006, 1996).

Although the physical validity of the outlet boundary condition is not quite true, this does not turn out to be a significant problem provided that the domain outflow is sufficiently far away from the body.

#### 3.4.3 Convergence and validation studies

##### Domain size

A numerical domain similar to that used in Leontini and Thompson (2013) was used as the numerical domain in the present study where the trailing part of the domain was increased to capture the long wave lengths associated with the low flow frequencies of galloping. This selection was done for two reasons. The first reason was that both Leontini and Thompson (2013) and the present study were carried out using the same numerical solving code. The second reason was that the cross sections used in both studies are similar. Thus, further optimisation of the domain need not be carried out as Leontini and Thompson (2013) has already shown this domain to be adequate for this class of flows.

For all cases, a rectangular domain was employed where the inlet was placed  $20D$  from the centre of the body, while the outlet was situated  $60D$  away from the centre of the body. The lateral boundaries were placed  $20D$  away from the centre of the body. The macro element arrangement of the general domain is shown figure 3.2. The macro element arrangement near the cross section was altered to cater for different cross sections. The near wall macro element configuration for the different cross sections are presented in figure 3.3. The domain incorporated was essentially similar to the domain used in Leontini and Thompson (2013) apart for the long trailing section to capture the long wavelengths of galloping frequencies.

##### Boundary conditions

The boundary conditions, regardless of the mesh, were common for all the simulations performed. A no-slip condition was applied to the cross section wall. This condition ensures that the velocity is zero at the surface of the cross section. For stationary simulations a Dirichlet boundary condition is applied to the inlet and lateral boundaries, specifying that the velocity is the freestream value. For FSI cases a time-dependent Dirichlet boundary condition was employed for the velocity on the inlet and lateral boundaries. A Dirichlet boundary condition has a specified value for the variables (Kreyszig, 2010) in this case velocity. The time-dependent Dirichlet condition has to be implemented for the FSI cases to account for the accelerated reference frame attached to the cross section. Thus, the inlet

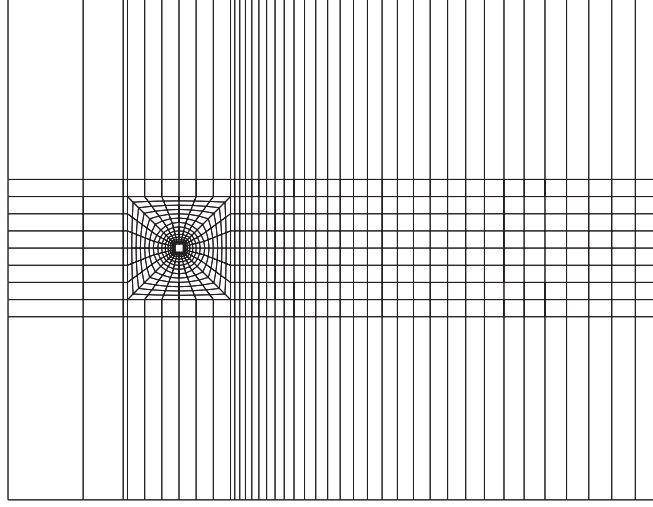


Figure 3.2: Macro element arrangement in the domain for the square cross section geometry. The inlet extending  $20D$  upstream from the centre of the body, while the outlet extends  $60D$  downstream from the centre of the body. The lateral boundaries were placed  $20D$  away from the centre of the body

boundary was set to  $u = U$  and  $v = -\dot{y}$  for FSI cases and  $v = 0$  for stationary cases, where  $u, v$  are the velocities in the  $x$  and  $y$  directions, respectively.

The outlet which is at the boundary downstream of the body was assigned a Neumann boundary condition (where the gradient of a property is specified Tu et al. (2008)),  $\frac{\partial \mathbf{V}}{\partial \mathbf{n}} = 0$  where  $\mathbf{n}$  denotes the unit normal vector. This assumes that the flow does not spatially evolve while exiting the domain.

### Convergence

A series of simulations for the oscillatory cases were carried out in order to ensure the results were grid independent. This was done by keeping the layout of the macro element the same and varying the order of the interpolation polynomial (*p-refinement*). The transverse velocity amplitudes were compared against various polynomial orders. The time step is also reduced as the spectral resolution increases to satisfy the Courant condition. The summary of the results is presented in figure 3.4 .

Figure 3.4 shows the mean velocity amplitude (sub-figure (a)) and the galloping fre-

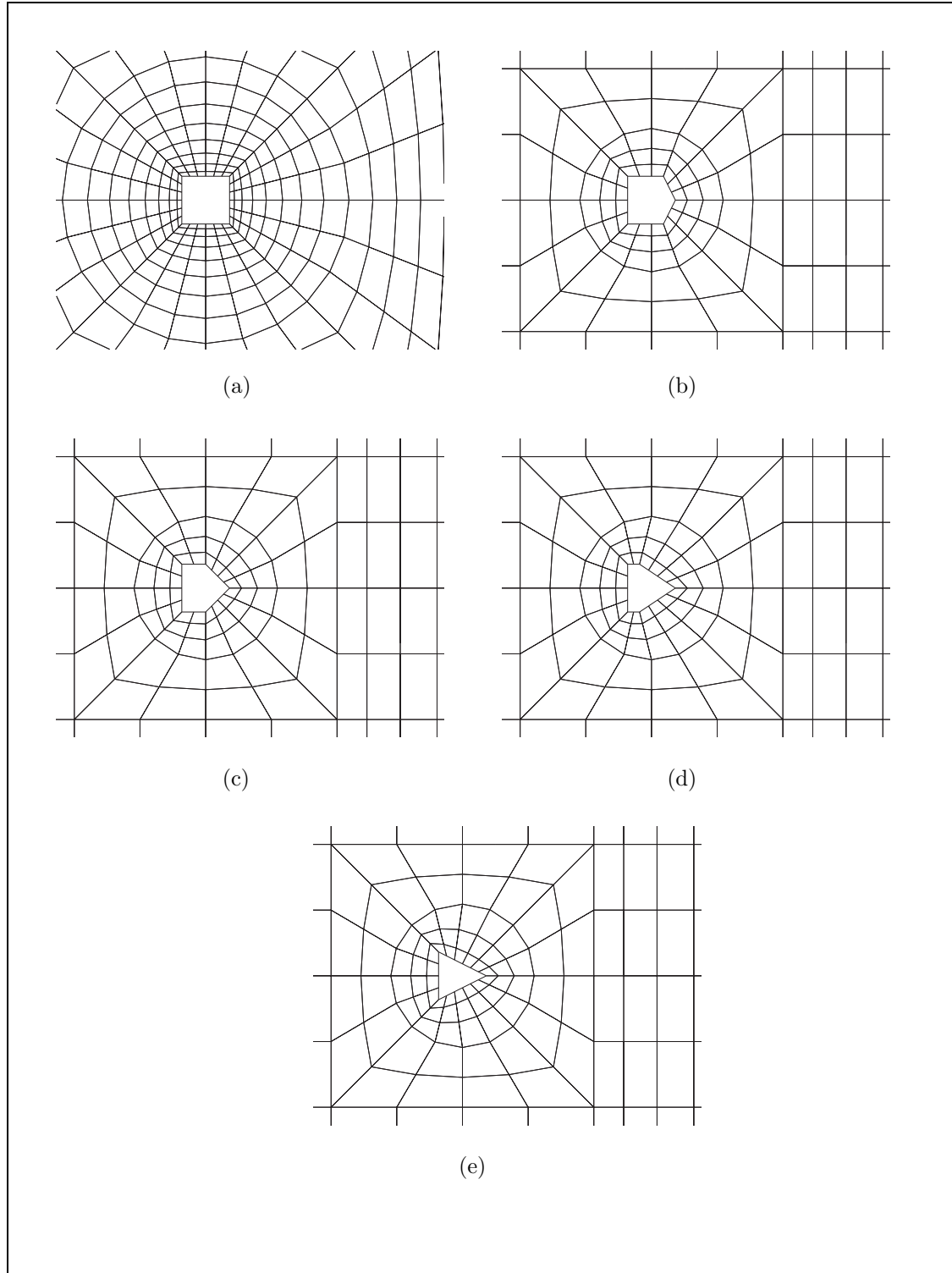


Figure 3.3: Configuration of the macro elements near the cross section. (a) square, (b)  $\frac{d}{\tau} = 0.75$ , (c)  $\frac{d}{\tau} = 0.5$ , (d)  $\frac{d}{\tau} = 0.25$  and (e) triangle.

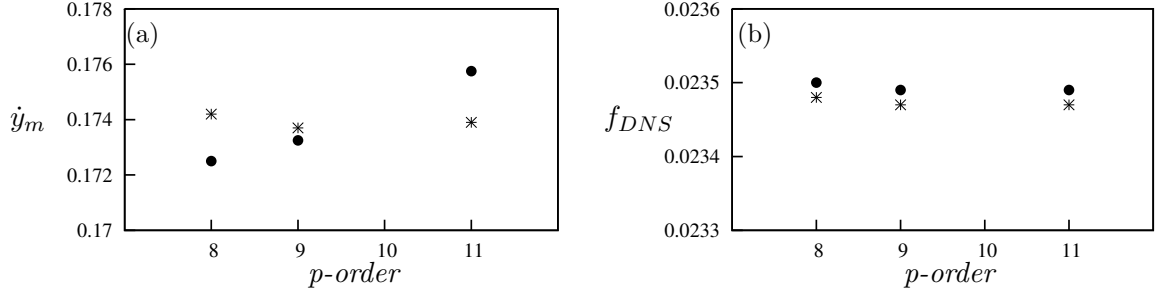


Figure 3.4: Mean velocity amplitude ( $\dot{y}_m$ ) (a) and the galloping frequency ( $f_{DNS}$ ) (b) as a function of the interpolation polynomial. Data present  $\frac{tU}{D} = 0.001$  (\*) and  $\frac{tU}{D} = 0.0005$  (•). Data acquired  $Re = 200$   $\Pi_2 = 0$  using FSI direct numerical simulations.

quency (sub-figure (b)) at different polynomial orders. Two factors namely, the quantitative accuracy of the data and the computational time had to be considered during the decision making process to obtain the optimum spacial and temporal resolution. Even though higher order polynomials gave very accurate data, the time step has to be reduced accordingly to meet the Courant condition. As galloping is a low frequency phenomenon, a longer time is taken to achieve the steady oscillating state. Furthermore, as galloping is dependent on the initial excitation of the flow, the initial development of galloping takes a significant amount of time. Both of these factors result in long computation times ranging from 1 to 2 weeks or more. Thus a 9<sup>th</sup> order polynomial was incorporated with  $\frac{tU}{D} = 0.001$  time-step which produced an acceptable computation time with an acceptable accuracy. A difference of less than 1% was achieved for both mean velocity amplitude of the body and galloping frequency using these spatial and temporal parameters.

As Leontini and Thompson (2013) used an 8<sup>th</sup> order polynomial with a time with a time step of 0.005, the current study which used a similar mesh as Leontini and Thompson (2013), incorporated an 11<sup>th</sup> order polynomial with  $\frac{tU}{D} = 0.00025$  time-step for static cases, to ensure high accuracy.

As the other cross sections presented in this thesis had relatively small deviation from the original square cross section, the FSI simulations were also carried out using these spatial and temporal parameters.



## CHAPTER 4

---

# GOVERNING PARAMETERS OF FLUID-ELASTIC GALLOPING

### 4.1 Introduction

The review of published literature reveals that fluid-elastic galloping has a potential to be used as a mechanism for energy extraction (Barrero-Gil et al., 2010). Thus, the following questions emerge. What are the optimum parameters for energy transfer in a galloping system? How do they influence galloping?

Another fluid-structure interaction phenomenon, vortex-induced vibration (VIV), has also been investigated as a candidate for the power extraction from flows. The work from Bernitsas et al. (2008, 2009); Raghavan and Bernitsas (2011); Lee and Bernitsas (2011) and others from the same group at the University of Michigan have made significant progress in this area of research. Therefore it may seem, at least initially, reasonable to present data from the fluid-elastic problem in the same parameters as typically used in VIV studies, which can be observed in current literature on galloping (Barrero-Gil et al., 2009, 2010; Parkinson and Smith, 1964).

However, the data presented in the pioneering study on energy harvesting from galloping (Barrero-Gil et al., 2010) presented using classical VIV parameters (i.e.  $U^*$ ,  $m^*\zeta$ ), shows that the mean power data does not collapse well. Here it is hypothesized that the reason behind this is the difference in time-scales of VIV and galloping. Thus the work presented

in this chapter is focused on testing this hypothesis. First, new parameters considering this difference in timescale are obtained, and then the optimum conditions for mean power output in terms of these new parameters are found.

Since the the Quasi-steady state model is the primary mathematical model used to model galloping in this study, the fluid-dynamic characteristics of flow over a static body are presented and discussed first as it is the main input to the QSS model. Then, the natural time scales of the system are obtained using the linearised QSS model. Next, the new non-dimensional governing parameters  $\Pi_1$  ( a type of combined mass-stiffness) and  $\Pi_2$  (a combined mass-damping), are formulated by non-dimensionalising the QSS model from these natural time scales. Following this is a comparison of galloping data using the classical VIV parameters and the new parameters  $\Pi_1$  and  $\Pi_2$ . Then, the influence of  $\Pi_1$  and  $\Pi_2$  and the conditions for an optimum power output are discussed from QSS data. Finally, the QSS data are compared and discussed against FSI direct numerical simulations and final conclusions are presented.

#### 4.1.1 Static body results

The main data acquisition tool for galloping is the QSS model. As discussed in chapter 3.2, the input to the QSS model is the lift force as a function of the induced angle of attack  $\theta$ . This function is obtained using lift and drag ( $C_y$ ) data from static body simulations or experiments, to which a polynomial is fitted. These static body data and the polynomial coefficients are presented here in figure 4.1 and table 4.1 respectively. Figure 4.1 shows the plots of time averaged  $C_y$  data as a function of  $\theta$ , as well as the 7<sup>th</sup> order polynomial fits. Data were acquired for high and low Reynolds numbers. For high Reynolds numbers, the static body polynomial data are obtained from Parkinson and Smith (1964) while for low Reynolds numbers a 7<sup>th</sup> order non-linear least square regression fit on static body DNS simulations was used.

There are several differences that can be observed between high and low Reynolds number data. The peak value of  $C_y$  is significantly lower at  $Re = 200$  ( $C_y = 0.12$  at  $5^\circ$ ) compared to  $Re = 22300$  ( $C_y = 0.57$  at  $13^\circ$ ) . The inflection point present around  $8^\circ$  for  $Re = 22300$  is not present at  $Re = 200$ . This agrees with the findings of Luo et al. (2003). Luo et al. (2003) concluded that hysteresis in the system response occurs due to

#### 4. GOVERNING PARAMETERS OF FLUID-ELASTIC GALLOPING

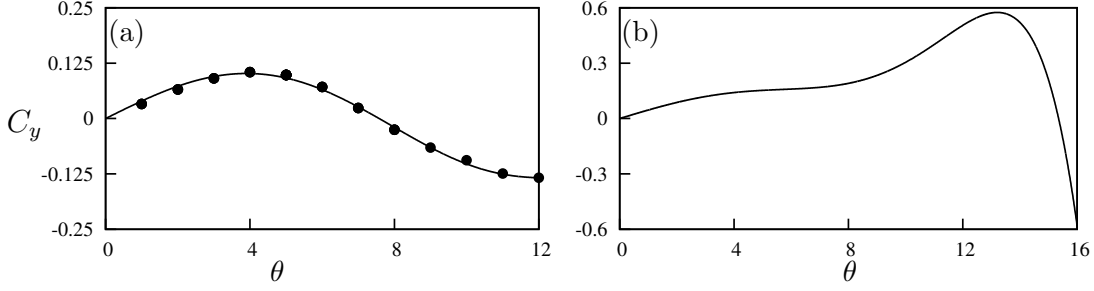


Figure 4.1: Lift coefficient,  $C_y$ , as a function of incidence angle  $\theta$ , for a static square cross section. (a) Data from simulations at  $Re = 200$  and (b) data from Parkinson and Smith (1964) at  $Re = 22300$ . The values at points ( $\bullet$ ) are acquired from direct numerical simulations. Curves in both plots are 7th-order interpolating polynomials used to interpolate the fluid forcing for the QSS model.

Case	$a_1$	$a_3$	$a_5$	$a_7$
$Re = 200$	2.32	197.8	4301.7	30311.9
$Re = 22300$	2.69	168	1670	59900

Table 4.1: Coefficient values used in the 7th order interpolation polynomial for high ( $Re = 22300$ ) and low ( $Re = 200$ ) Reynolds numbers. These data are used as input data to calculate the right-hand side of Eq. 2.5 throughout this study.

the inflection point in the  $C_y$  curve. Therefore, hysteresis can not be observed at  $Re = 200$ .

The range of incident flow angles where  $C_y$  remains positive is narrow at  $Re = 200$  ( $0^\circ < \theta \leq 7^\circ$ ) compared to  $Re = 22300$  ( $0^\circ < \theta \leq 15^\circ$ ). This positive range sustains galloping, as the power is only transferred from the fluid to the supporting structure within this range of incident angles. This is because the fluid forces are acting in the direction of velocity of the body, or in phase with, the oscillating body as demonstrated by equation 3.2. Incident angles beyond this range suppress the galloping as power is transferred in the opposite direction, i.e; from body to fluid. Thus, it is expected that the transferred power at  $Re = 200$  to be significantly lower than at  $Re = 22300$ , because of the relatively low

values of  $C_y$  and the narrow range of positive  $C_y$  at  $Re = 200$ .

#### 4.1.2 Formulation of the new dimensionless groups $\Pi_1$ and $\Pi_2$

The natural time scales of the system can be found by solving for the eigenvalues of the linearised equation of motion (Eq:2.5), namely

$$m\ddot{y} + c\dot{y} + ky = \frac{1}{2}\rho U^2 \mathcal{A}a_1 \left( \frac{\dot{y}}{U} \right), \quad (4.1)$$

which is a simplified version of the equation of motion presented in equation 2.5 with the polynomial series for the lift force truncated at the linear term.

Combining the  $\dot{y}$  terms and solving for eigenvalues  $\lambda$  gives

$$\lambda_{1,2} = -\frac{1}{2} \frac{c - \frac{1}{2}\rho U \mathcal{A}a_1}{m} \pm \frac{1}{2} \sqrt{\left[ \frac{c - \frac{1}{2}\rho U \mathcal{A}a_1}{m} \right]^2 - 4 \frac{k}{m}}. \quad (4.2)$$

If it is assumed that the spring is relatively weak,  $k \rightarrow 0$ , a single non-zero eigenvalue remains. This eigenvalue is

$$\lambda = -\frac{c - \frac{1}{2}\rho U \mathcal{A}a_1}{m}. \quad (4.3)$$

Further, if it is assumed that the mechanical damping is significantly weaker than the fluid-dynamic forces on the body,  $c \rightarrow 0$  and

$$\lambda = \frac{\frac{1}{2}\rho U \mathcal{A}a_1}{m}. \quad (4.4)$$

In this form,  $\lambda$  represents the inverse time scale of the motion of the body due to the effect of the long-time fluid-dynamic forces. In fact, the terms can be regrouped and  $\lambda$  written as

$$\lambda = \frac{a_1}{m^*} \frac{U}{D} \quad (4.5)$$

Written this way, the important parameters that dictate this inverse time scale are clear. The rate of change in the fluid-dynamic force with respect to angle of attack when the body is at the equilibrium position,  $\partial C_y / \partial \theta$ , is represented by  $a_1$ . The mass ratio is represented by  $m^*$ . The inverse advective time scale of the incoming flow is represented by the ratio  $U/D$ . Increasing  $a_1$  would mean the force on the body would increase more rapidly with small changes in the angle of attack,  $\theta$ , or transverse velocity. Equation 4.5 shows that such a change will increase the inverse time scale, or analogously decrease the

response time of the body. Increasing the mass of the body, thereby increasing  $m^*$ , has the opposite effect. The inverse time scale is decreased, or as might be expected, a heavier body will respond more slowly.

This timescale can then be used to non-dimensionalize the equation of motion, and to find the relevant dimensionless groups of the problem. It was suggested by Shiels et al. (2001); Leonard and Roshko (2001) to use a flow-based timescale such  $D/U$  for the characteristic time for flow-induced vibration problems, rather than a structural-based timescale such as the natural frequency. This point is discussed further in Williamson and Govardhan (2004). Here, this advective time is further scaled by the mass ratio  $m^*$ , as suggested from the eigenvalues of the linearized equation of motion. Hence, if the non-dimensional time,  $\tau$ , is defined such that  $\tau = t(a_1/m^*)(U/D)$ , the equation of motion presented in equation 2.5 can be non-dimensionalized as

$$\ddot{Y} + \frac{m^{*2}}{a_1^2} \frac{kD^2}{mU^2} Y = \left( \frac{1}{2} - \frac{m^*}{a_1} \frac{cD}{mU} \right) \dot{Y} - \frac{a_1 a_3}{m^{*2}} \dot{Y}^3 + \frac{a_1^3 a_5}{m^{*4}} \dot{Y}^5 - \frac{a_1^5 a_7}{m^{*6}} \dot{Y}^7. \quad (4.6)$$

The coefficients can be regrouped into combinations of non-dimensional groups, and rewritten as

$$\ddot{Y} + \frac{4\pi^2 m^{*2}}{U^{*2} a_1^2} Y = \left( \frac{1}{2} - \frac{c^* m^*}{a_1} \right) \dot{Y} - \frac{a_1 a_3}{m^{*2}} \dot{Y}^3 + \frac{a_1^3 a_5}{m^{*4}} \dot{Y}^5 - \frac{a_1^5 a_7}{m^{*6}} \dot{Y}^7, \quad (4.7)$$

where  $U^*$  is the reduced velocity typically used as an independent variable in vortex-induced vibration studies and  $c^* = cD/mU$  is a non-dimensional damping parameter.

Equation 4.7 shows there are five non-dimensional parameters that play a role in setting the response of the system. These are the stiffness (represented by the reduced velocity  $U^*$ ), the damping  $c^*$ , the mass ratio  $m^*$ , and the geometry and  $Re$ , represented by the coefficients of the polynomial fit to the  $C_y$  curve,  $a_n$ . The grouping of these parameters into two groups in equation 4.7 which arise by non-dimensionalising using the natural time scale of the galloping system, suggests there are two groups besides geometry (represented by  $a_n$ ) and  $Re$  that dictate the response:  $\Gamma_1 = 4\pi^2 m^{*2}/U^{*2} a_1^2$  and  $\Gamma_2 = c^* m^*/a_1$ . For a given geometry and Reynolds number,  $\Gamma_1$  can be thought of as a combined mass-stiffness, whereas  $\Gamma_2$  can be thought of a combined mass-damping parameter. It is assumed that during galloping the stiffness plays only a minor role because galloping time periods are significantly large which implies that  $k \rightarrow 0$ . Therefore,  $\Gamma_2$  seems a likely parameter to collapse the data. In fact, in the classic paper on galloping from Parkinson and Smith

---

(1964), galloping data from wind tunnel tests is presented in terms of a parameter that can be shown to be the same as  $\Gamma_2$ .

All of the quantities that make up  $\Gamma_1$  and  $\Gamma_2$  can, in theory, be known before an experiment is conducted. However, the quantity  $a_1$  is a relatively difficult one to determine, requiring static body experiments or simulations. Here, the geometry is unchanged and results are only being compared at the same  $Re$ . Hence, suitable parameters can be formed by multiplying  $\Gamma_1$  and  $\Gamma_2$  by  $a_1^2$  and  $a_1$  respectively, to arrive at a mass-stiffness parameter  $\Pi_1 = 4\pi^2 m^{*2}/U^{*2}$ , and a mass-damping parameter defined as  $\Pi_2 = c^* m^*$ .

Equation 4.7 can be re-written explicitly in terms of  $\Pi_1$  and  $\Pi_2$  to give

$$\ddot{Y} + \Pi_1 \dot{Y} = \Pi_2 \dot{Y} - \frac{a_1 a_3}{m^{*2}} \dot{Y}^3 + \frac{a_1^3 a_5}{m^{*4}} \dot{Y}^5 - \frac{a_1^5 a_7}{m^{*6}} \dot{Y}^7. \quad (4.8)$$

#### 4.1.3 Comparison of $\Pi_1$ and $\Pi_2$ with classical VIV parameters

Figure 4.2 shows the comparison of mean power data at  $Re = 200$  presented using different independent variables. Subfigures (a), (c) and (e) show the displacement amplitude, velocity amplitude and the mean power as a function of the classic VIV parameter,  $U^*$  for various damping ratios  $\zeta$ . Subfigures (b), (d) and (f) shows the same data as a function of  $\Pi_2$ , for various, reasonably high values of  $\Pi_1$ , as defined above in section 4.1.2. The data presented using the classical VIV parameters follows the same trends as Barrero-Gil et al. (2010). Barrero-Gil et al. (2010) and Vicente-Ludlam et al. (2014) observed that the maximum dimensionless power is achieved at two times the velocity at which the galloping starts. A similar conclusion can be drawn from the data presented here in figures 4.2. However, the data presented using the dimensionless group formulated using the natural time scales of the system shows an excellent collapse for both velocity amplitude and mean power, showing that the power is essentially dictated by  $\Pi_2$ . This implies that unlike VIV which is a type of resonant phenomenon, the natural frequency of the system which is used to scale  $U^*$ ,  $\zeta$  and  $\Pi_1$  does not have a large influence on the system behaviour in these cases.

While the velocity and power data collapse well, the amplitude data still shows some spread. Figure 4.3 shows the displacement amplitude data obtained in figure 4.2 (a), but rescaled on a length scale that considers the stiffness by incorporating  $\Pi_1$ , which essentially

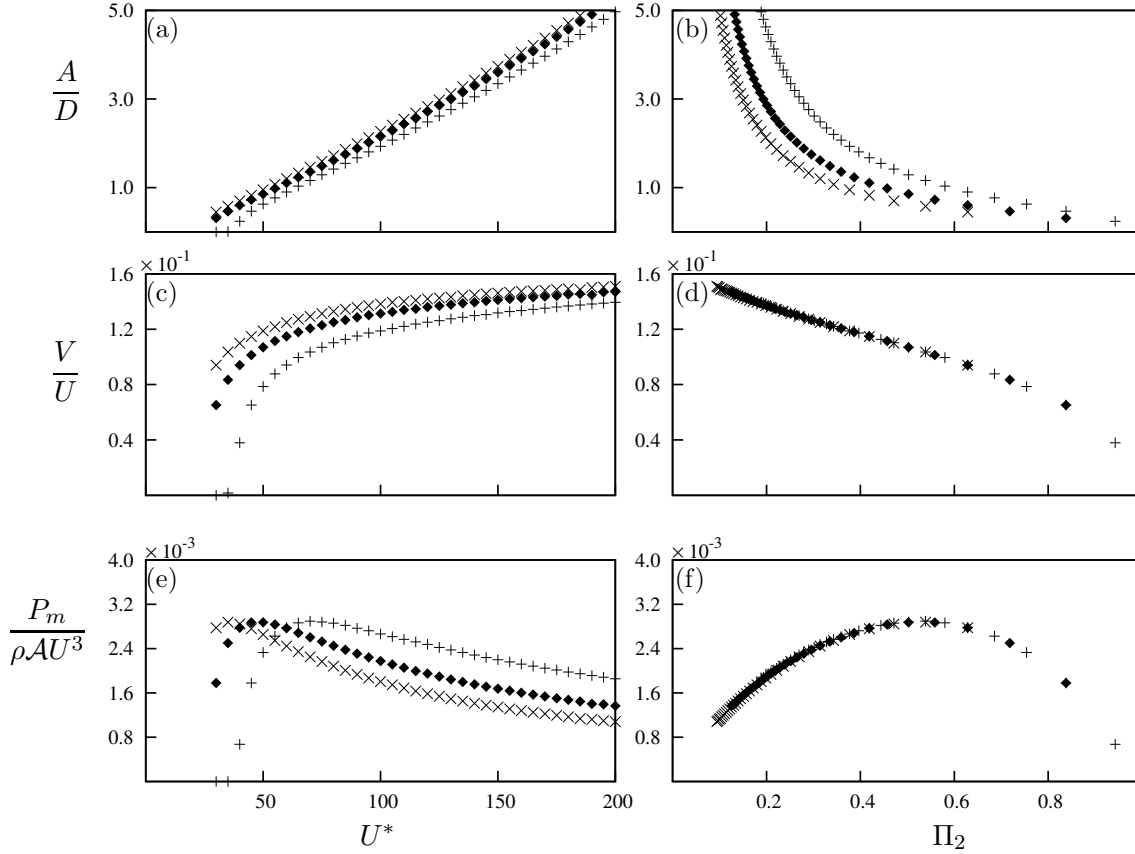


Figure 4.2: Displacement amplitude, velocity amplitude and dimensionless mean power data as functions of two different independent variables. Data presented in (a), (c) and (e) using the classical VIV parameter  $U^*$ , obtained at  $Re = 200$  and  $m^* = 20$  at three different damping ratios:  $\zeta = 0.075$  ( $\times$ ),  $\zeta = 0.1$  ( $\blacklozenge$ ) and  $\zeta = 0.15$  ( $+$ ). (b) (d) and (f) are the same data presented using the combined mass-damping parameter ( $\Pi_2$ ) as the independent variable. Even though  $\Pi_1$  varies in the range of  $0.4 \leq \Pi_1 \leq 17.5$ , it is clear that the power is a function of  $\Pi_2$  only.

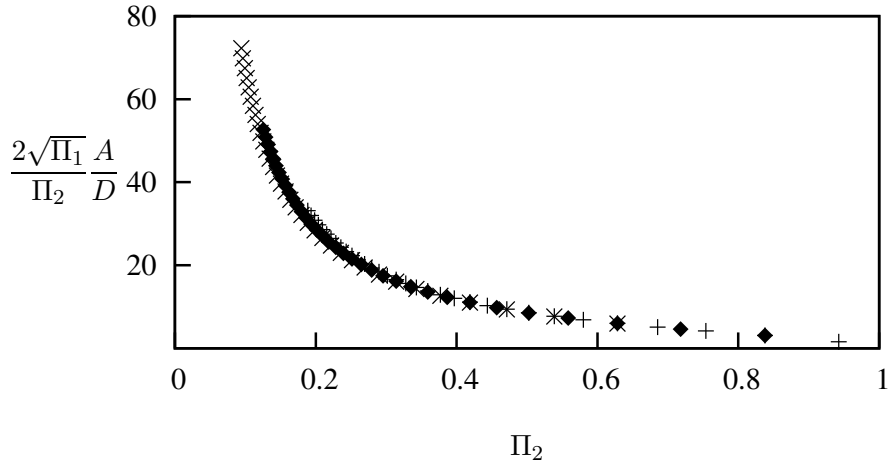


Figure 4.3: Displacement amplitude data as a function of  $\Pi_2$ . obtained at  $Re = 200$  and  $m^* = 20$  at three different damping ratios:  $\zeta = 0.075$  ( $\times$ ),  $\zeta = 0.1$  ( $\blacklozenge$ ) and  $\zeta = 0.15$  ( $+$ ). The dependent variable is scaled with  $\frac{2\sqrt{\Pi_1}}{\Pi_2}$  which is equal to  $\frac{1}{\zeta}$ . This scaling is similar to Parkinson and Smith (1964) and the deviation of data using this scaling at high  $U^*$  could be observed in Parkinson and Smith (1964)



reduces the scaling parameter to  $\frac{1}{\zeta}$ , shows an excellent collapse. Thus, it is clear that the displacement amplitude is dependent on both  $\Pi_1$  and  $\Pi_2$ . It can be seen that as  $\Pi_1$  and  $\Pi_2 \rightarrow 0$ ,  $\frac{A}{D}$  approaches infinity; where for very slack springs the body will need to travel a larger distance to balance the transverse force.

#### 4.1.4 Comparison of power between high and low $Re$ data

The marked success of the collapse using  $\Pi_2$  for the  $Re = 200$  case, particularly of the mean power, can also be replicated for the higher  $Re$  case at  $Re = 22300$ . Figure 4.4 presents the mean power for high  $Re$  cases for selected values of  $\Pi_1$ . It is shown that the data collapse in both cases, demonstrating the validity of using  $\Pi_2$  as an independent variable.

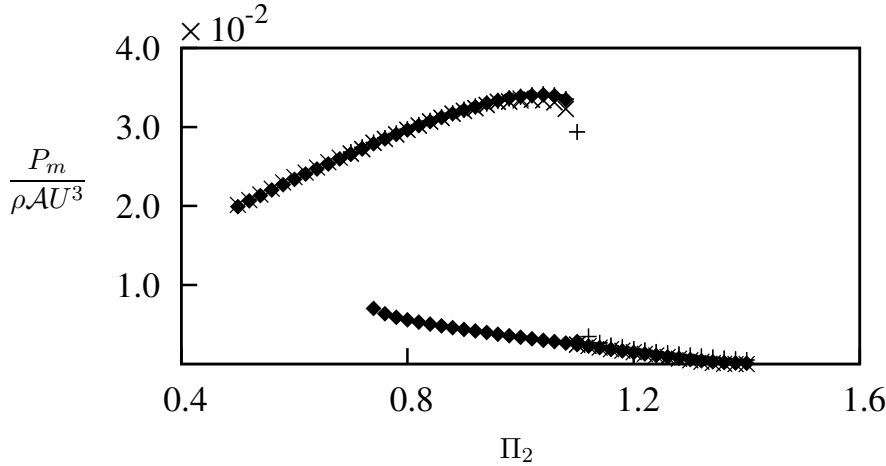


Figure 4.4: Dimensionless mean power as a function of  $\Pi_2$ . Data presented at  $Re = 22300$ ,  $\Pi_1 = 200$  ( $\times$ ),  $\Pi_1 = 2000$  ( $\blacklozenge$ ) and  $\Pi_1 = 10000$  ( $+$ ). Hysteresis could be observed at high  $Re$ .

Hysteresis can be observed for the  $Re = 22300$  case. The different solutions can be obtained by manipulating the initial conditions (initial displacement) of the system. The upper branch was obtained by giving an initial displacement which was higher than the expected amplitude while the lower branch was obtained by providing a lower initial displacement than the expected amplitude. Although theory shows a possible third state, it is an unstable branch which cannot be achieved with a time integration method such as that employed in this study. This was also observed by Vio et al. (2007).

#### 4.1.5 Dependence on mass-stiffness, $\Pi_1$

The results of sections 4.1.3 and 4.1.4 show that the mean extracted power is essentially a function of a single variable, the combined mass-damping  $\Pi_2$ . However, the timescale analysis of section 4.1.2 showed that a second variable, the combined mass-stiffness  $\Pi_1$  should also play a role. Previous studies (see, for example Bouclin (1977)) have also indicated a complex interaction between the amplitude and natural frequency, particularly for high natural frequencies (or equivalently, low values of  $\Pi_1$ ). Here, the impact of  $\Pi_1$  is investigated further. Overall, the system behaviour can be separated into two wide regimes; that for “high”  $\Pi_1$  and that for “low”  $\Pi_1$ . These two regimes are further investigated and explained in this following section.

Figure 4.5 shows the mean power as a function of  $\Pi_2$  for a range of values of  $\Pi_1$ . Two subfigures are shown; subfigure (a) shows data for  $\Pi_1 \geq 10$ , while (b) shows data for  $\Pi_1 \leq 10$ . In figure 4.5(a), the collapse of the mean power is excellent, showing that for  $\Pi_1 \geq 10$ , the mean power is independent of  $\Pi_1$ .

For low values of  $\Pi_1 \leq 10$ , figure 4.5(b) shows that the predicted mean power increases as  $\Pi_1$  is decreased, indicating that the mean power is a weak function of  $\Pi_1$  at low  $\Pi_1$  levels. This provides the distinction between high and low  $\Pi_1$  regimes. For high values where  $\Pi_1 \geq 10$ , the mean extracted power is a function of  $\Pi_2$  only; for low values where  $\Pi_1 < 10$ , the mean extracted power is a weak function of  $\Pi_1$ .

Regardless of the value of  $\Pi_1$ , the variation of the mean extracted power with  $\Pi_2$  is essentially the same. With increasing  $\Pi_2$ , the mean extracted power initially increases, before reaching some maximum value and then decreases. This relationship between power and  $\Pi_2$  can be explained by analysing the time histories of selected cases. Data at  $\Pi_1 = 10$ ,  $m^* = 20$  and  $Re = 200$  are shown in figure 4.6 and are analysed as an example. Values of  $\Pi_2$  less than (region 1), equal to (region 2), and greater than (region 3) the value where the mean extracted power is a maximum are analysed as examples.

The instantaneous power from the fluid to the body can be expressed as  $P_t = F_y \dot{y}$ . Similarly the dissipated power due to the mechanical damping can be expressed as  $P_d = (c\dot{y})\dot{y}$ . The time average of these two quantities, described in equations 3.1 and 3.2 must be equal due to energy conservation.

At region 1 ( $\Pi_2 = 0.15$ ) the damping is low in comparison with region 2 and 3. While

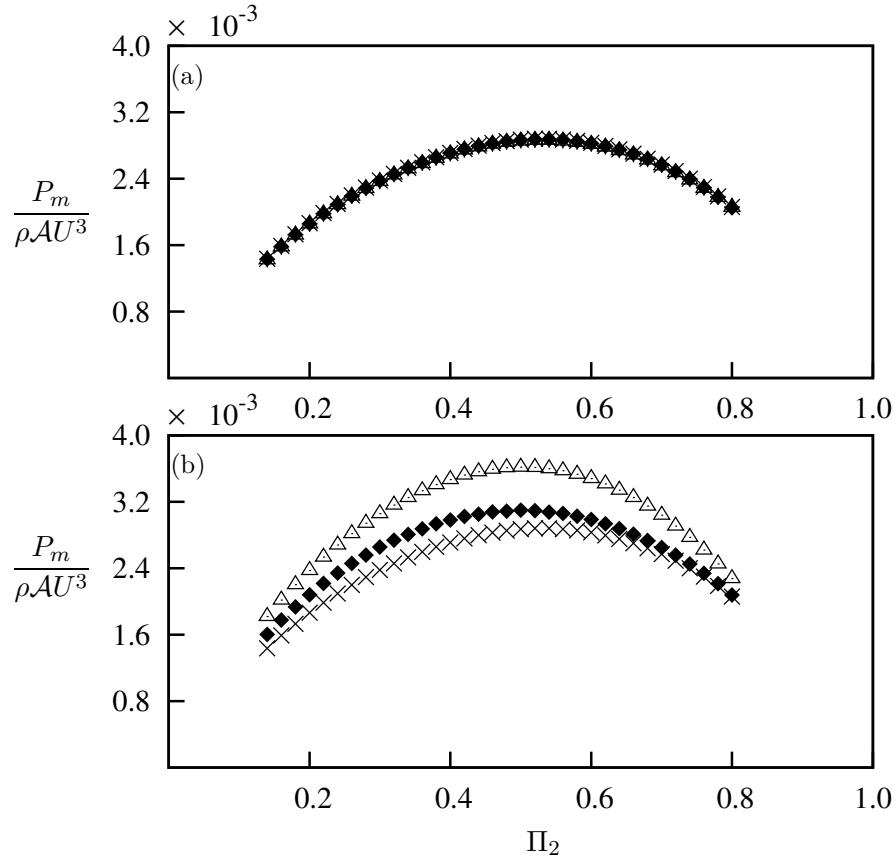


Figure 4.5: Dimensionless mean power as a function of  $\Pi_2$  obtained using the QSS model at  $Re = 200$ . (a) High  $\Pi_1$ ; data presented at four different combined mass-stiffness levels.  $\Pi_1 = 10$  ( $m^* = 20$ ,  $U^* = 40$ ) ( $\times$ ),  $\Pi_1 = 100$  ( $m^* = 80$ ,  $U^* = 50$ ) ( $+$ ),  $\Pi_1 = 500$  ( $m^* = 220$ ,  $U^* = 60$ ) ( $\blacklozenge$ ) and  $\Pi_1 = 1000$  ( $m^* = 400$ ,  $U^* = 40$ ) ( $\triangle$ ). (b) Low  $\Pi_1$ ; data presented at  $\Pi_1 = 10$  ( $\times$ ),  $\Pi_1 = 0.1$  ( $\blacklozenge$ ), and  $\Pi_1 = 0.01$  ( $\triangle$ ).

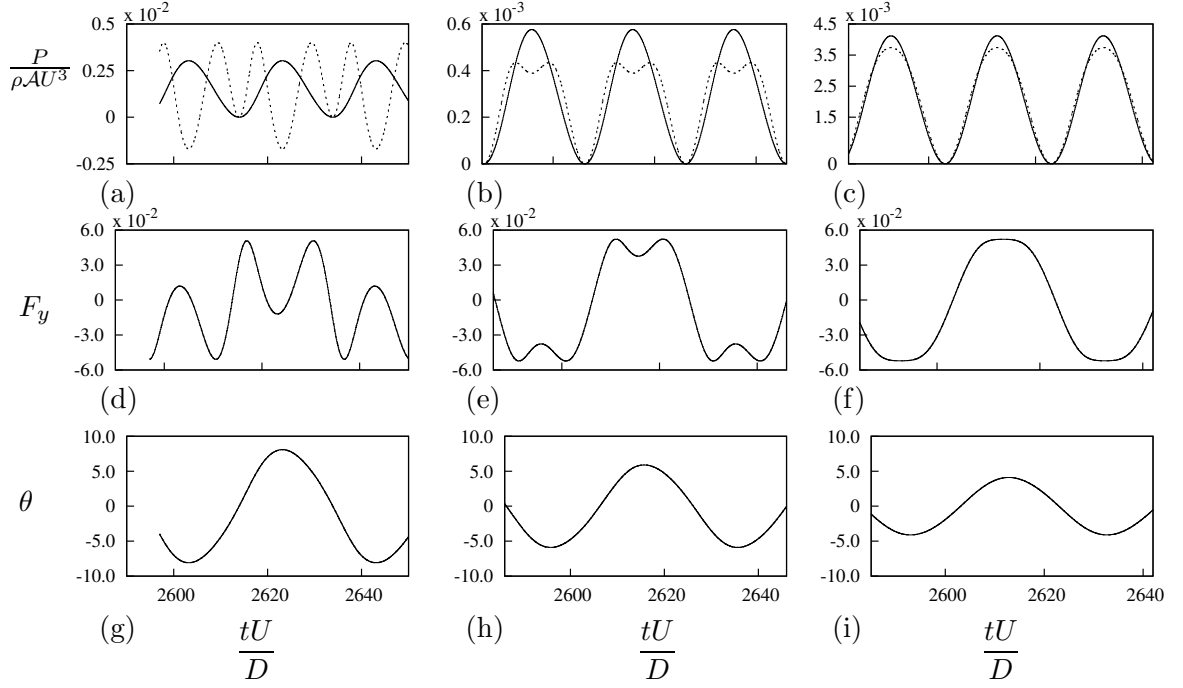


Figure 4.6: Time histories of  $P_t$ ,  $P_d$ ,  $F_y$  and  $\theta$  at  $\Pi_2 = 0.15, 0.54$  and  $0.8$  from the QSS model. Data was obtained at  $m^* = 20$ ,  $\Pi_1 = 10$  and  $Re=200$ . The time histories of  $P_d$  (—) and  $P_t$  (---) are presented for: (a)  $\Pi_2 = 0.15$ ; (b)  $\Pi_2 = 0.54$ ; (c)  $\Pi_2 = 0.8$ . Time histories of the instantaneous force  $F_y$  for: (d)  $\Pi_2 = 0.15$ ; (e)  $\Pi_2 = 0.54$ ; (f)  $\Pi_2 = 0.8$ . Time histories of the instantaneous angle  $\theta$  for: (g)  $\Pi_2 = 0.15$ ; (h)  $\Pi_2 = 0.55$ ; (i)  $\Pi_2 = 0.8$ .

this may lead to larger oscillations, damping is required to dissipate and therefore extract power according to equation 3.1. Therefore, the low damping in this region leads to a low mean power output. Fig.4.6 (a) shows that  $P_d$  (the power dissipated by damping) becomes negative over some portion of the cycle. This is caused by the high velocity amplitude leading to the equivalent incident angle  $\theta$  to exceed the range where  $C_y$  is positive (i.e.  $0 < \theta < 6^\circ$  as shown in figure 4.1(a)). In this portion of the cycle the fluid-dynamic force actually opposes the direction of travel and power is transferred from the structure to the fluid during those times. From an energy perspective, the mechanical damping is not sufficient to remove the energy transferred from the fluid to the structure through work during other times of the cycle because  $\Pi_2$  is substantially low. Therefore this excess energy is transferred back to the fluid as depicted by the negative region of  $P_d$ .

At region 3 where  $\Pi_2 = 0.8$  the damping constant is high and a clear sinusoidal signal is observed for both  $P_d$  and  $P_t$  in figure 4.6(c). Figures 4.6(f) and 4.6(i) show that equivalent incident angle  $\theta$  (which for small values, is proportional to the transverse velocity of the body) is in phase with  $F_y$ . The velocity amplitude in this case is small and  $\theta$  is within the range where the fluid-dynamic force increases with the incident angle (i.e.  $0 < \theta \leq 5^\circ$  as shown in figure 4.1(a)). According to equation 3.2, these conditions are suitable for high power output. However in this case, the high damping limits the velocity amplitude and results in relatively low fluid dynamic forces.

At region 2 (  $\Pi_2 = 0.54$ ), a balance is found between high and low values of damping.  $P_d$  is not a pure sinusoidal signal, however the signal remains periodic. From the time history graph of  $P_d$ , two ‘peaks’ are present in a single half cycle as shown in figure 4.6(b). In this case, the velocity amplitude actually exceeds the equivalent incident angle where the fluid-dynamic forces peaks (i.e.  $\theta = 5^\circ$  in figure 4.1 (a)). The dips in  $P_d$  between the two peaks approximately correspond to the time where the transverse velocity is higher than 0.09 (i.e.  $\theta = 5.14$ ) and  $F_y$  decreases with increasing transverse velocity. The mean power output is at its maximum. This is due to the fact that this region is the best compromise between regions 1 and 3. The damping is high enough to obtain a high power output while not so high that the motion is completely suppressed.

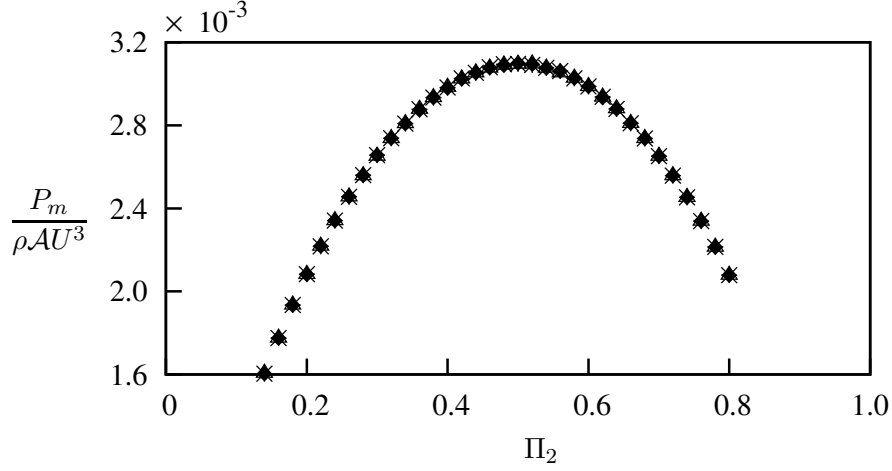


Figure 4.7: Dimensionless mean power as a function of  $\Pi_2$  obtained using QSS model at  $\Pi_1 = 0.1$ . Data presented at  $m^* = 2$  ( $\blacklozenge$ ),  $m^* = 20$  ( $\triangle$ ) and  $m^* = 50$  ( $*$ ). The mass ratio does not have an effect on  $P_m$  even at low  $\Pi_1$ .

#### 4.1.6 Dependence on the mass ratio $m^*$

While for high values of  $\Pi_1$  it is clear that the mean extracted power is a function of  $\Pi_2$  only, a question arises for low values of  $\Pi_1$ ; is the variation in the mean extracted power purely a function of  $\Pi_1$ , or is it also a function of the mass ratio  $m^*$ ? To answer this question, the model has been solved for a fixed value of  $\Pi_1$ , but for varying values of  $m^*$ . This means that  $\Pi_1$  was varied by changing the system stiffness.

Figure 4.7 shows the mean extracted power as a function of  $\Pi_2$ , for a fixed  $\Pi_1 = 0.1$ , for three different values of  $m^*$ . From the figure it is clear that the results are independent of  $m^*$ , and are functions of  $\Pi_1$  and  $\Pi_2$  only.

#### 4.1.7 Comparison with DNS data

The QSS model assumes that the only force driving the system is the instantaneous lift, which is same as the mean lift on a static body at the same angle of attack. However, vortex shedding is also present in this system. Therefore, an essential assumption when this model is used, is that the effect of vortex shedding is minimal. Hence, the model has been always used at high  $Re$  and at high mass ratios because at those Reynolds numbers and mass ratios, the vortex shedding does not correlate across the span. This study is focused on identifying the limiting parameters of the QSS model at low Reynolds numbers

by providing a comparison with DNS results.

Joly et al. (2012) showed that the displacement data obtained using the QSS assumption and DNS agree well at low Reynolds numbers, with the modification implemented to the oscillator equation which accounts for the vortex shedding. These data were obtained at zero damping levels. However, the current study is focused on the behaviour and the power transfer of the system. Therefore analysing the behaviour of the system with increasing damping is of interest.

The comparison between QSS and the DNS results is presented in figure 4.8. The maximum displacement, velocity and mean extracted power are presented as functions of  $\Pi_2$ . A range of values of  $\Pi_1$  is compared with the QSS model data for  $\Pi_1 = 10$ . Figures 4.8(a) and 4.8(b) show little variation with  $\Pi_1$ , and the comparison between the QSS model and the DNS simulations is quite good. However, the mean extracted power shown in figure 4.8(c) reveals that the mean power is influenced by both  $\Pi_1$  and  $\Pi_2$ . This is particularly clear for low values of  $\Pi_1$ , where the discrepancy between the QSS model predictions of power and the DNS simulations is the largest. Comparison of figure 4.8(c) with figure 4.5(a) shows that  $\Pi_1$  has much more influence on the power extracted than predicted by the QSS model for low  $\Pi_1$  values. In fact, the QSS model predicts that the mean extracted power should increase with decreasing  $\Pi_1$  when  $\Pi_1$  moves to the low  $\Pi_1$  region (figure 4.5(b)), whereas the DNS simulations show that the mean extracted power decreases with decreasing  $\Pi_1$ .

Figure 4.9(a) clearly shows the dependence of the mean extracted power on  $\Pi_1$ . Here, the maximum power extracted for a given value of  $\Pi_1$ , over all values of  $\Pi_2$  (essentially the value of extracted power at the turning point), is plotted as a function of  $\Pi_1$ . These values were obtained by fitting a quadratic to the data of figure 4.7 and finding the value of mean extracted power at the turning point. The rapid decrease in the extracted power as  $\Pi_1 \rightarrow 0$  is clear.

Figure 4.9(a) also shows that  $\Pi_1$  is important to higher values than predicted by the QSS model. For the QSS model, the mean extracted power was essentially independent of  $\Pi_1$  for  $\Pi_1 > 10$ , as shown by the open symbols on the figure. However, the mean extracted power from the DNS data shows a significant dependence on  $\Pi_1$  for  $\Pi_1 < 250$ . Even so, the power extracted during the DNS simulations converges to the value predicted by the

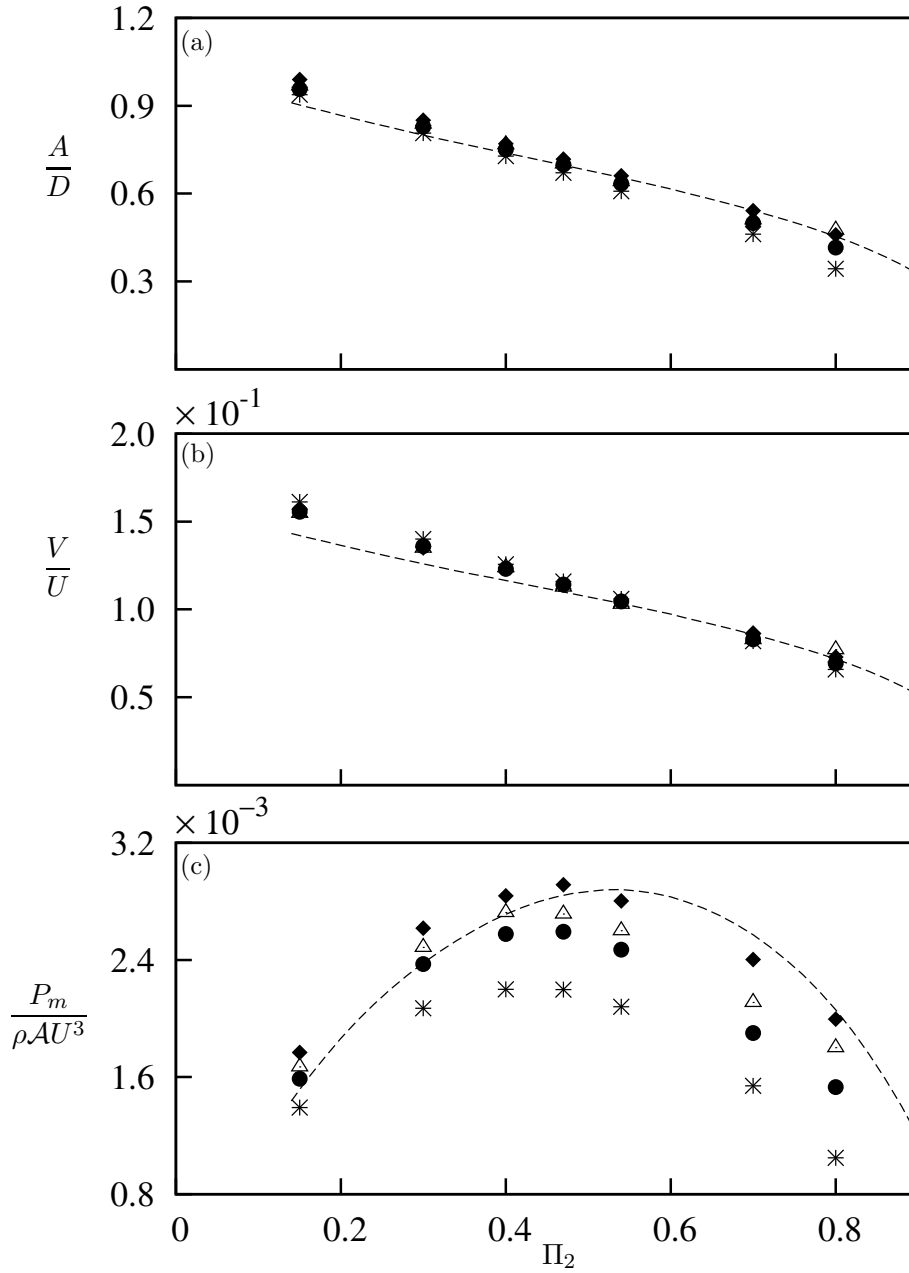


Figure 4.8: Comparison of data generated using the quasi-static model and full DNS simulations at (a) Displacement amplitude, (b) velocity amplitude and (c) dimensionless mean power as functions of  $\Pi_2$ . Data were obtained at  $Re = 200$  at four values  $\Pi_1 = 10$  ( $m^* = 20.13$ ) (\*),  $\Pi_1 = 60$  ( $m^* = 49.31$ ) (●),  $\Pi_1 = 250$  ( $m^* = 100.7$ ) (△) and  $\Pi_1 = 1000$  ( $m^* = 201.3$ ) (◆). The QSS data at  $\Pi_1 = 10$  (---).



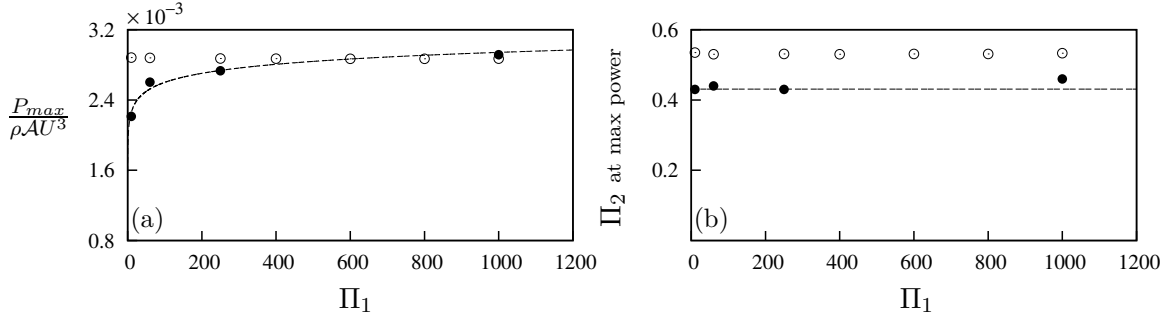


Figure 4.9: (a) Maximum power and (b) the value of  $\Pi_2$  at maximum power of QSS data (○) and DNS data (●), as functions of  $\Pi_1$ . For the DNS data, the maximum power asymptotes to an upper value with increasing  $\Pi_1$ , while the value of  $\Pi_2$  where maximum power occurs is relatively insensitive to  $\Pi_1$ . The maximum power of the QSS data remains relatively constant, as does the value of  $\Pi_2$  where maximum power occurs. The dash curve (---) of (a) follows the logarithmic fit of the maximum power which is  $P_{max}/\rho AU^3 = 1.48 \times 10^{-4} \log(\Pi_1) + 1.9 \times 10^{-3}$ . The dashed curve in (b) shows the value  $\Pi_2 \simeq 0.43$ .

QSS model as  $\Pi_1$  increases.

Figure 4.9(b) shows the value of  $\Pi_2$  at which the turning point, and therefore the maximum power output, occurs. The open symbols show the value predicted by the QSS model, the closed symbols show the value predicted by the DNS. The two are not the same, with a value around 0.41 predicted by the DNS (shown with a dashed line) and a value above 0.5 predicted by the QSS model. However, both models show that while the power extracted is a reasonably strong function of  $\Pi_1$ , the value of  $\Pi_2$  at which this maximum power occurs is relatively unaffected.

In an effort to further quantify the performance of the QSS model, the percentage between the QSS and DNS extracted power data as a function of  $\Pi_1$  was calculated using the equation

$$\% \text{ error} = \left| \frac{P_{m(QSS)} - P_{m(DNS)}}{P_{m(DNS)}} \right| \times 100. \quad (4.9)$$

The results of this calculation are plotted in figure 4.10, along with a power-law best fit of  $\% \text{ error} = 138.697\Pi_1^{-0.6}$ . The figure clearly shows that as  $\Pi_1$  increases, the error between the QSS and DNS models quickly decreases. However, at low values of  $\Pi_1$ , the discrepancy between the two can be quite large, around 30%.

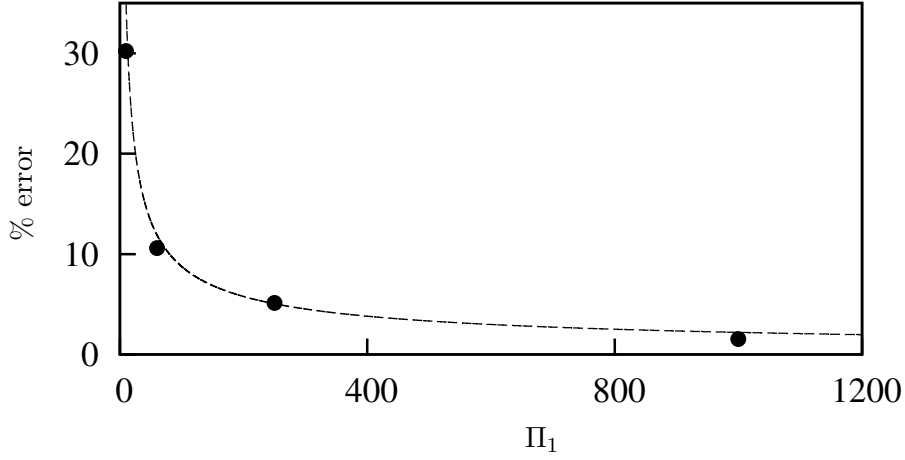


Figure 4.10: The percentage error between the maximum power obtained using DNS data and predicted by QSS model as a function of  $\Pi_1$ . The deviation between them is large for low values of  $\Pi_1$ . The dash curve (---) follows the power law fit of the percentage error which is  $\%error = 138.697\Pi_1^{-0.6}$ .

A likely reason for this discrepancy at low  $\Pi_1$  is the influence of the vortex shedding, which is not accounted for in the QSS model. To investigate this further, frequency spectra for the body velocity from DNS cases at varying values of  $\Pi_1$ , at a value of  $\Pi_2 = 0.47$  (close to the value at which the mean extracted power is a maximum), have been produced. They are presented, along with the original time histories in figure 4.11.

This figure shows the velocity signals at  $\Pi_1 = 0.8$  and  $\Pi_2 = 10, 60, 250$  and 1000 and the corresponding spectrum. The spectral data shows a significant frequency component around  $fd/U = 0.156$  which can be identified as the vortex shedding frequency. The magnitude of the frequency component at the vortex shedding frequency clearly reduces as  $\Pi_1$  is increased. This indicates that the influence of vortex shedding is much more prominent at low  $\Pi_1$ , therefore resulting in larger deviations from quasi-steady state results. This builds on the work of Joly et al. (2012), which was conducted at zero damping, that implied that mean extracted power would be influenced by vortex shedding at low mass. The transverse forcing signal and the respective spectrum are presented for the same cases in figure 4.12. The comparison of figures 4.11 and 4.12 clearly shows that even though vortex shedding has a high significant relative forcing the system tend to select the galloping frequency as the frequency of oscillation.

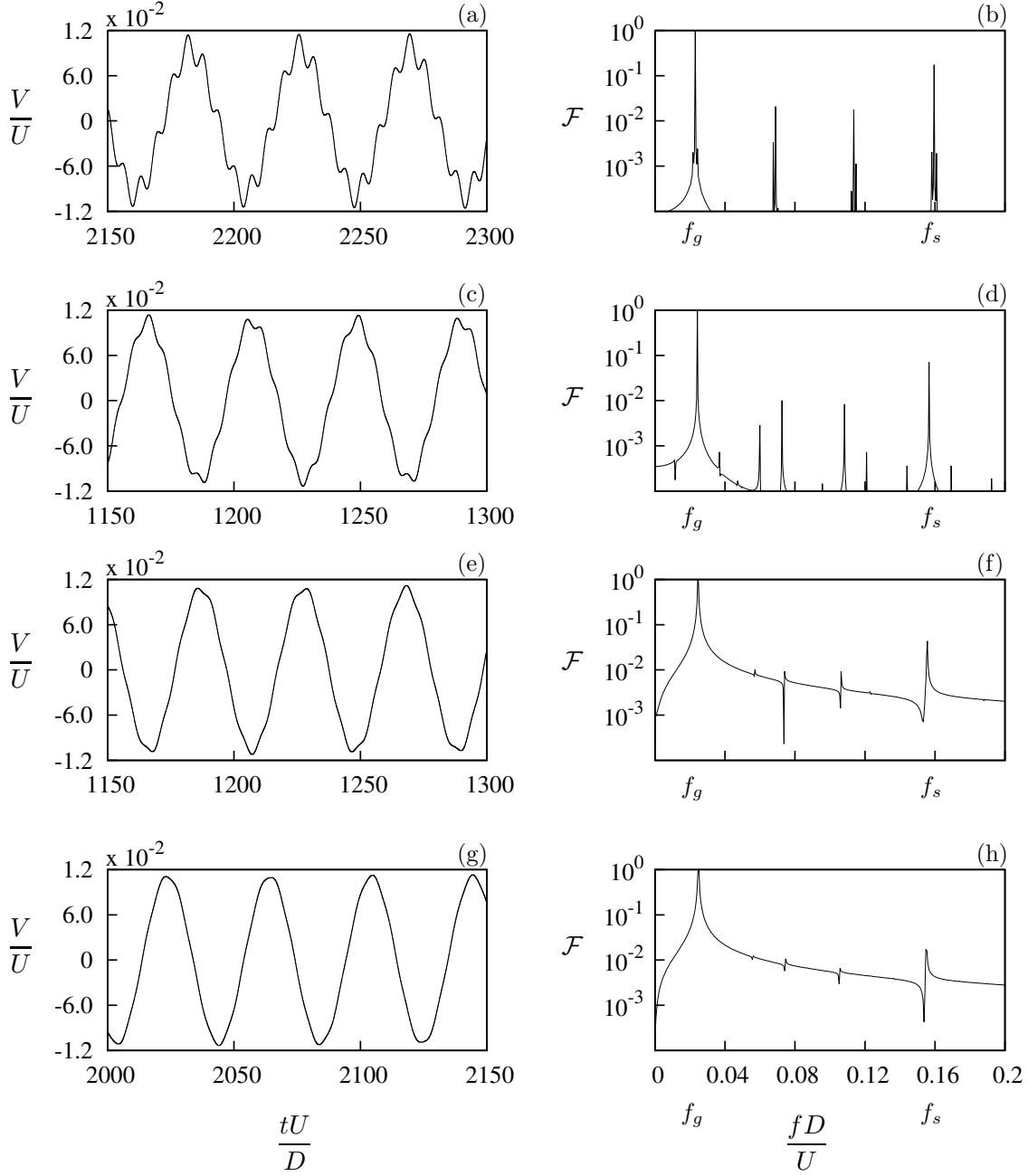


Figure 4.11: Velocity signal (right) and the corresponding power spectrum (left) of the DNS data at four values of  $\Pi_1$  at  $\Pi_2 = 0.47$ . (a) and (b)  $\Pi_1 = 10$ , (c) and (d)  $\Pi_1 = 60$ , (e) and (f)  $\Pi_1 = 250$ , (g) and (h)  $\Pi_1 = 1000$ .  $f_g$  and  $f_s$  represents galloping and vortex shedding frequencies respectively.  $U^*$  is kept at 40 therefore the mass ratio increases as  $\Pi_1$  increases. It is evident that the influence of vortex shedding reduces as the inertia of the system increases.

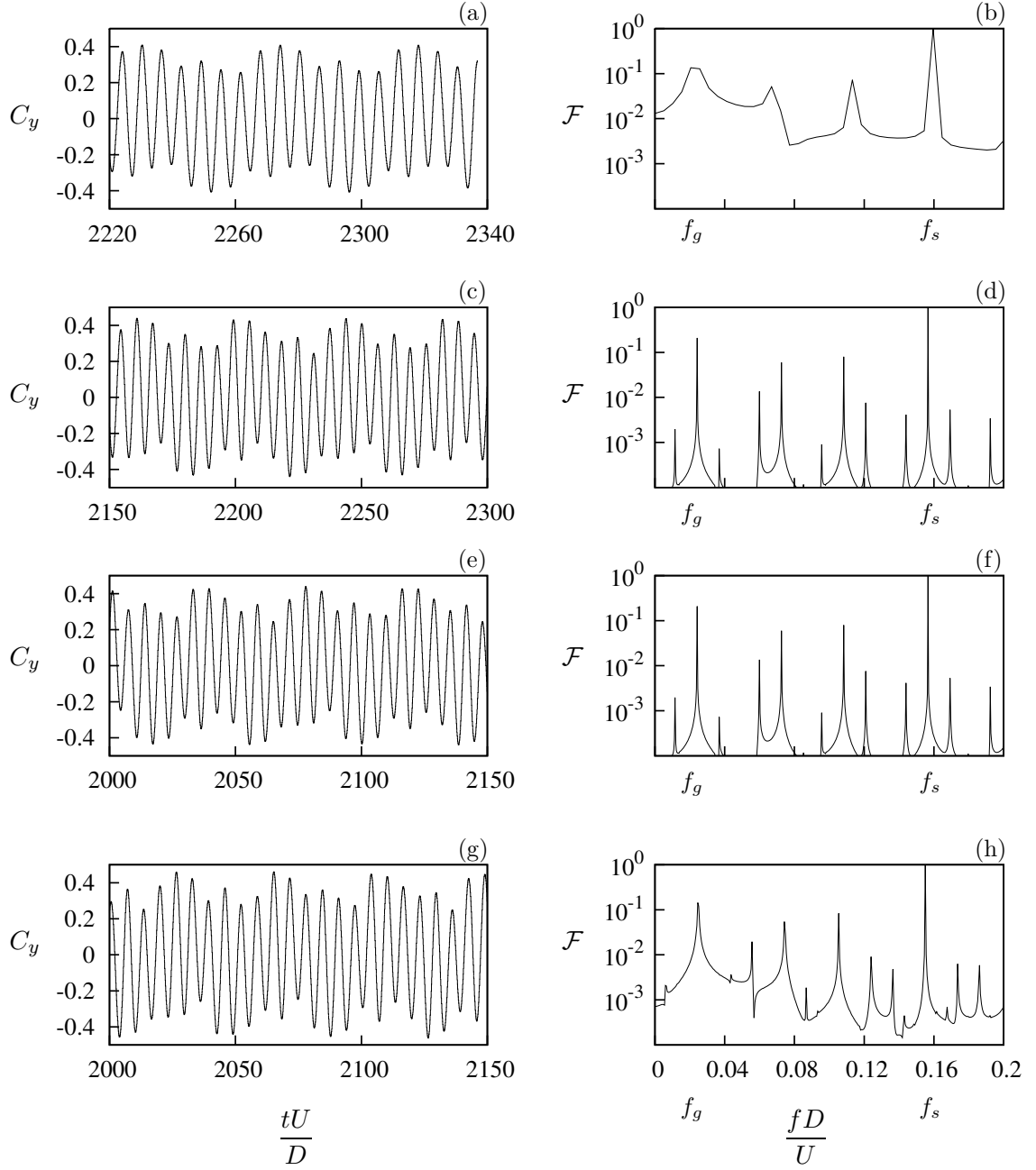


Figure 4.12: Transverse force  $F_y$  signal (right) and the corresponding power spectrum (left) of the DNS data at four values of  $\Pi_1$  at  $\Pi_2 = 0.47$ . (a) and (b)  $\Pi_1 = 10$ , (c) and (d)  $\Pi_1 = 60$ , (e) and (f)  $\Pi_1 = 250$ , (g) and (h)  $\Pi_1 = 1000$ .  $f_g$  and  $f_s$  represents galloping and vortex shedding frequencies respectively.  $U^*$  is kept at 40 therefore the mass ratio increases as  $\Pi_1$  increases. It is evident that the influence of vortex shedding reduces as the inertia of the system increases.

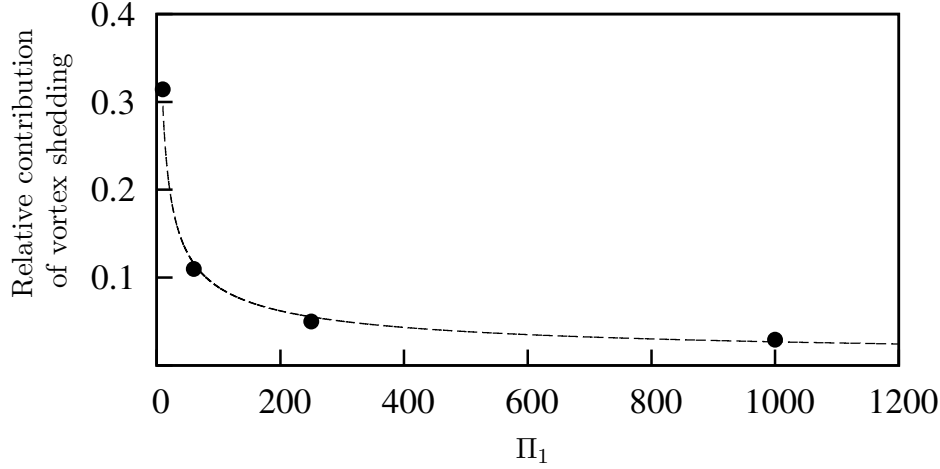


Figure 4.13: The relative contribution of the vortex shedding as a function of  $\Pi_1$ . The relative power of the vortex shedding decreases as  $\Pi_1$  increases. The dash curve (---) follows the power law fit of the percentage error which is  $\text{Relative power} = 0.977\Pi_1^{-0.52}$ .

This influence is explicitly shown here. Figure 4.13 plots the relative intensity of vortex shedding and galloping in the spectra of figure 4.11 which essentially shows the relative contribution of vortex shedding of the galloping system at the give  $\Pi_1$ .

Similar to the discrepancy between the QSS and DNS mean extracted power shown in figure 4.10, the relative strength of the vortex shedding is seen to be large at small values of  $\Pi_1$ , and quickly decreases as  $\Pi_1$  is increased. The figure shows that the relative power of the vortex shedding frequency to the galloping frequency varies like  $0.977\Pi_1^{-0.52}$ .

The difference between the power predicted by the QSS and DNS models scales with  $\Pi_1^{-0.6}$ ; the relative power at the vortex shedding frequency scales with  $\Pi_1^{-0.52}$ . These scalings are quite similar, and both are close to  $1/\sqrt{\Pi_1}$ . While not unequivocal, this correlation strongly indicates this discrepancy is due to the influence of the vortex shedding, even though the vortex shedding and galloping frequencies remain separated by around the same amount for all values of  $\Pi_1$  presented in figure 4.11. The data presented in figure 4.13 also give some indication of the magnitude of any vortex shedding correction term that might be added to the QSS model in an effort to decrease the discrepancy between it and the DNS simulations.

Further information can be gained by observing the flow field. Non-dimensionalised flow field data at values of  $\Pi_2$  close to where maximum power is produced at different  $\Pi_1$

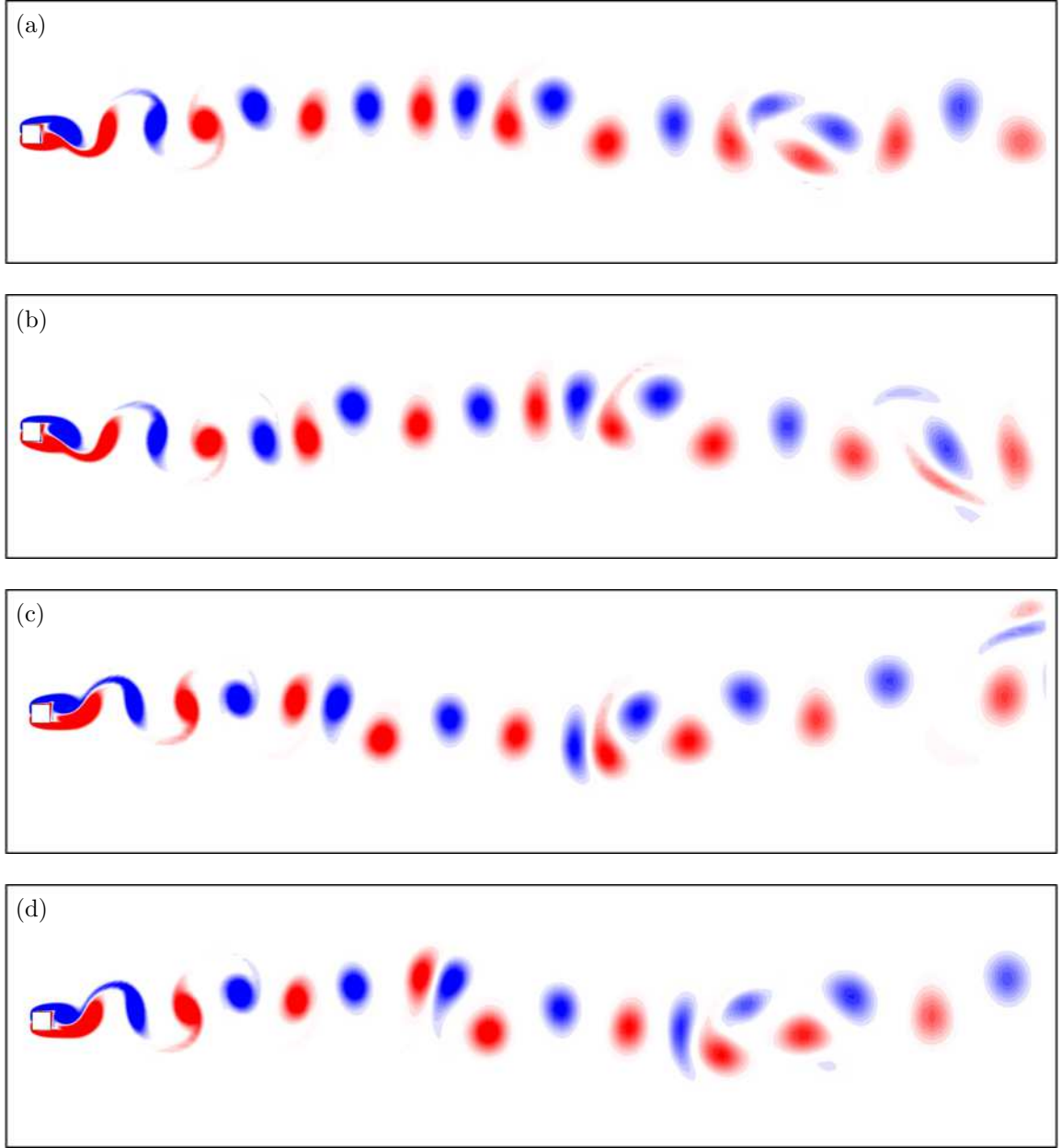


Figure 4.14: Vorticity plots of the flow at arbitrary instants at  $\Pi_2 = 0.47$ . (a)  $\Pi_1 = 10$ , (b)  $\Pi_1 = 60$  (c)  $\Pi_1 = 250$  and (d)  $\Pi_1 = 1000$  at  $Re = 200$ . Contours show vorticity at levels between  $\pm 1$ .

are presented in figure 4.14. The figure shows a clear wavelength of the wake as  $\Pi_1$  is increased. Qualitatively, this can be interpreted as showing that at high  $\Pi_1$ , the vortex shedding is simply superimposed over the path of motion of the cylinder. It shows a decrease

in amplitude of the path of the body at low  $\Pi_1$ , which may be due to the higher levels of non-linear interaction between the vortex shedding and galloping. Such an argument is consistent with the data of figure 4.13 that show the increasing influence of vortex shedding on the velocity of the body as  $\Pi_1$  decreases. Taken together, this also goes some way to explaining the discrepancy between the output power predicted by the QSS and DNS models at low  $\Pi_1$ , highlighted in figure 4.10.

## 4.2 Frequency response of the system

The new governing parameters ( $\Pi_1$  and  $\Pi_2$ ) formulated in section 4.1.2 using the linearised QSS equation show that the velocity amplitude and mean power output are effectively a function of a single parameter,  $\Pi_2$ . The amplitude of the displacement also collapses if the second parameter,  $\Pi_1$ , is also used to scale the amplitude.

Here the frequency response of the body is investigated in terms of these two new parameters.

### 4.2.1 Formulating the linear frequency of the system

The process was initiated by considering the eigenvalues of the linearised QSS model (Eq:4.1), which can be found in equation 4.2. The term under the square root (equation 4.10) of this equation can be used to express the frequency of the system provided that the eigenvalues are complex.

If this condition (presence of complex eigenvalues) is satisfied, the imaginary component can be identified as the frequency of the system.

$$f = \sqrt{\left[ \frac{c - \frac{1}{2}\rho U A a_1}{(m)} \right]^2 - 4 \frac{k}{(m)}}. \quad (4.10)$$

By substituting  $c^*$ ,  $m^*$  and  $U^*$  equation 4.10 can be non-dimensionalised as

$$f = \sqrt{\left[ c^* \left( \frac{U}{D} \right) - \frac{1}{2} \frac{a_1}{m^*} \left( \frac{U}{D} \right) \right]^2 - 4 \left( \frac{U}{D} \right)^2 \frac{2\pi}{U^*}}. \quad (4.11)$$

This can then be rewritten as

$$f_{lin} = \sqrt{\left( \frac{U}{D} \right)^2 \left( c^* - \frac{a_1}{2m^*} \right)^2 - 4 \left( \frac{U}{D} \right)^2 \left( \frac{2\pi}{U^*} \right)^2}. \quad (4.12)$$


---

By taking the factor of  $U/D$  to the left-hand side

$$\frac{f_{lin}D}{U} = \sqrt{\left(c^* - \frac{a_1}{2m^*}\right)^2 - 4\left(\frac{2\pi}{U^*}\right)^2}. \quad (4.13)$$

Expanding terms gives

$$\frac{f_{lin}D}{U} = \sqrt{c^{*2} - \frac{2c^*a_1}{2m^*} + \frac{a_1^2}{4m^{*2}} - \frac{16\pi^2}{U^{*2}}}. \quad (4.14)$$

Multiplying through by  $m^*$  gives

$$\frac{f_{lin}Dm^*}{U} = \sqrt{c^{*2}m^{*2} - c^*m^*a_1 + \frac{a_1^2}{4} - \frac{16\pi^2m^{*2}}{U^{*2}}}. \quad (4.15)$$

By substituting  $\Pi_1$  and  $\Pi_2$  appropriately the expression of the linear frequency is reduced to

$$\frac{f_{lin}Dm^*}{U} = \sqrt{\Pi_2^2 - \Pi_2a_1 + \frac{a_1^2}{4} - 4\Pi_1}. \quad (4.16)$$

Thus, a non-dimensionalised expression for the frequency of the system can be formulated from  $\Pi_1$  and  $\Pi_2$ , which is defined as the linear frequency  $f_{lin}$  of the system.

Note that  $f_{lin}$  is nondimensionalised using the same timescale as was used to arrive at  $\Pi_1$  and  $\Pi_2$ , namely  $m^*(D/U)$ . This definition of  $f_{lin}$  provides a natural limit; when the quantity below the square root in equation (4.16) becomes positive,  $f_{lin}$  will not be a frequency, but a prediction of the growth rate of the amplitude of the body (a complex quantity, generated by a negative number under the square root, is required to produce an oscillation).

## 4.2.2 Comparison of predicted frequencies using different approaches

Predictions for the frequency of the system were obtained using three different techniques namely the predictions of the linearised QSS model, predictions from the full QSS model and DNS. For given values of  $\Pi_1$  and  $\Pi_2$  the linear frequency  $f_{lin}$  was found by solving equation 4.10.  $f_{QSS}$  was obtained by performing a power spectrum analysis on the time trace of the velocity of the body obtained by numerically solving the quasi-steady state equation.  $f_{DNS}$  was obtained using a similar technique as  $f_{QSS}$  however, the velocity data was obtained through DNS simulations of fluid-structure interactions. Data were obtained at a constant undamped natural frequency of  $f = 0.025$  ( $U^* = 40$ ).



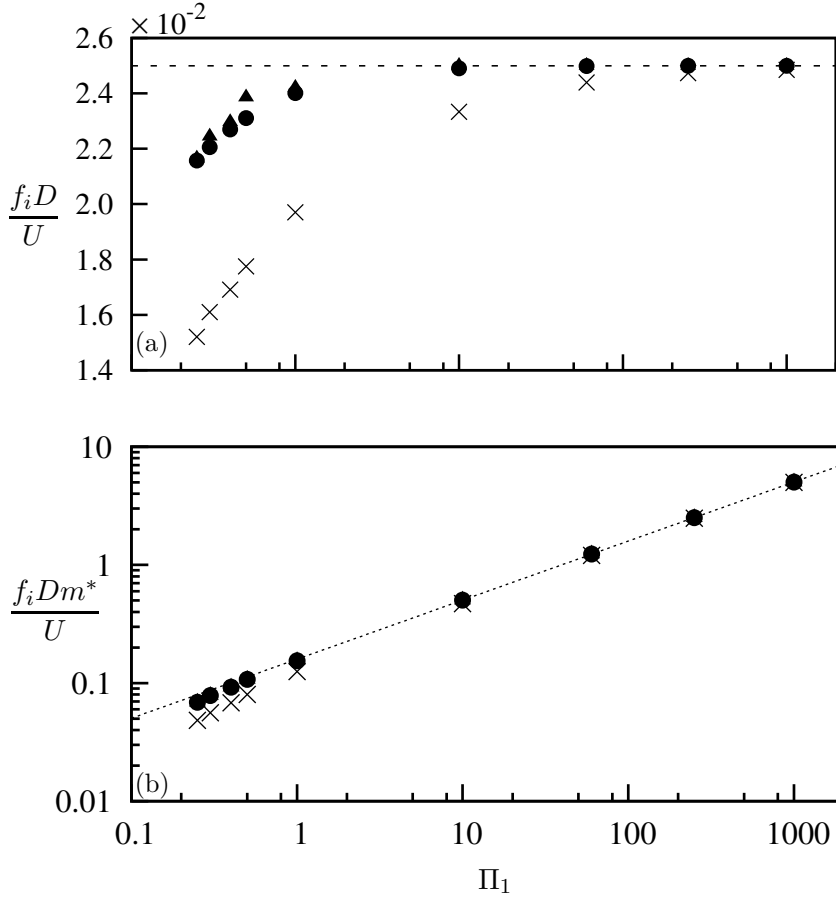


Figure 4.15: Frequency data as a function of  $\Pi_1$ , (a) without and (b) with scaling with  $m^*$ . Frequency obtained using QSS simulations, DNS simulations and the linear frequency equation (Eq:4.12).  $f_i$  is the type of frequency i.e.  $f_{DNS}, f_{QSS}, f_{lin}$ . Data present  $f_{lin}$  ( $\bullet$ ),  $f_{QSS}$  ( $\blacktriangle$ ) and  $f_{DNS}$  ( $\times$ ) at  $\Pi_2 = 0.15$ ,  $Re = 200$  and undamped natural frequency,  $f = 0.025$  (---).

The three frequency predictions are presented as a function of  $\Pi_1$  in figure 4.15 at a constant  $\Pi_2$  of 0.15. Here, the undamped natural frequency was kept constant at  $f = 0.025$  ( $U^* = 40$ ). Thus,  $\Pi_1$  was varied by varying  $m^*$ . Data in figure 4.15 (a) is presented without the scaling of  $m^*$  and 4.15 (b) is presented with the scaling of  $m^*$ . The dilation of different frequencies as  $\Pi_1$  reduces, can clearly be observed in figure 4.15 (a) without the scaling of  $m^*$ .

The DNS frequency  $f_{DNS}$ , deviates from  $f_{lin}$  for low values of  $\Pi_1$ . However, it converges to  $f_{lin}$  around  $\Pi_1 = 10$ . In comparison, both  $f_{lin}$  and  $f_{QSS}$  converge to  $f_{lin}$  much quicker, around  $\Pi_1 = 1$ , with  $f_{lin}$  converging slightly quicker than  $f_{QSS}$ . One noticeable fact is that

the linear frequency deviates from  $f_{in}$  and reduces rapidly for values of  $\Pi_1$  less than 1 in comparison with  $f_{QSS}$ . One possible explanation for this effect is the contribution of the higher-order nonlinear terms present in the forcing in the QSS model presented in equation 2.5. For small values of  $\Pi_1$ , these terms will start to have a significant effect. As these nonlinear terms by definition are not included in  $f_{lin}$ , their relatively larger impact will make the linear frequency prediction less accurate. Furthermore, the ratio of  $\frac{f_{lin}}{f_{QSS}}$  (figure 4.16) shows the deviation becoming larger as the system approaches the region of high power transfer ( $\Pi_2$  0.4 – 0.5). This can be an indication of the non-linearities of the forcing becoming more prominent in the the region of higher power transfer.

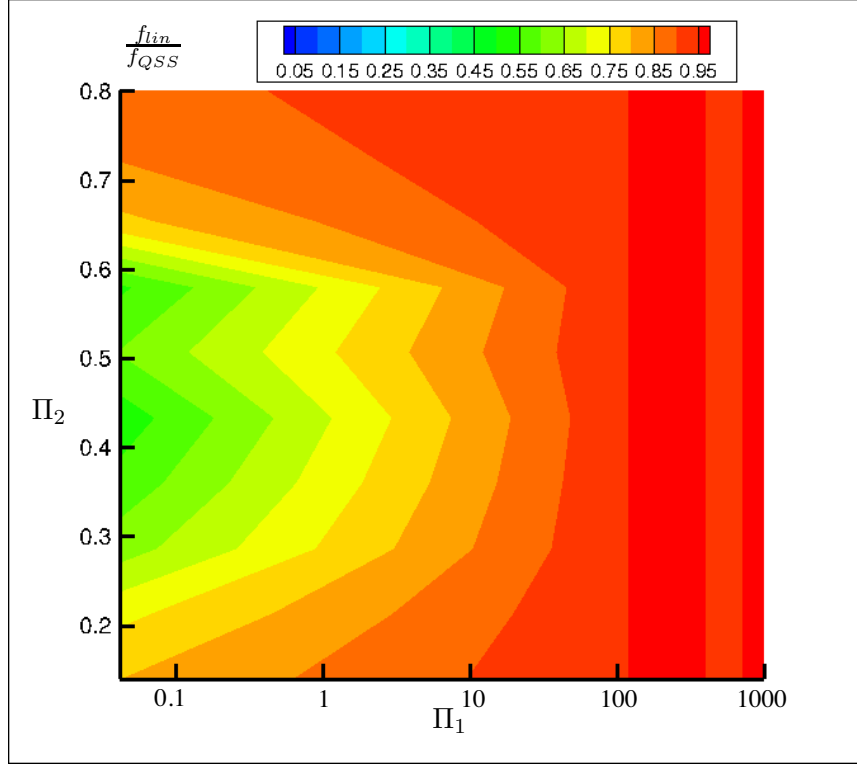


Figure 4.16: Contour plot of  $\frac{f_{lin}}{f_{QSS}}$  in  $\Pi_1$   $\Pi_2$  space. A deviation between the  $f_{lin}$  and  $f_{QSS}$  can be observed for  $\Pi_1 < 10$ . The deviation becomes larger as the system approaches the region of high power transfer ( $\Pi_2$  0.4 – 0.5).

Figure 4.17 shows the time traces of transverse velocity  $\dot{y}$  and the induced angle  $\theta$  obtained using the QSS model, at the two extreme cases of  $\Pi_1$ . The time traces at  $\Pi_1 =$

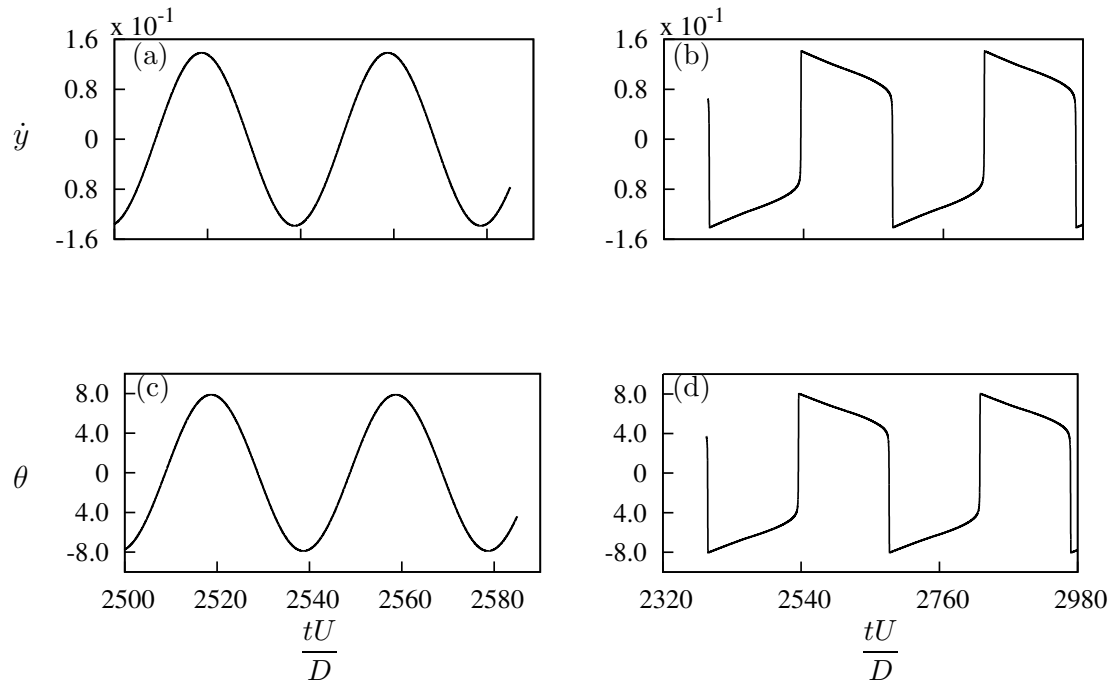


Figure 4.17: Time histories of  $\dot{y}$  and  $\theta$  at  $\Pi_2 = 0.2$  and  $U^* = 40$  obtained from the QSS model . The time histories presented for : (a) and (c) at  $\Pi_1 = 1000$ ; (b) and (d) at  $\Pi_1 = 0.001$  representing the two regions of frequency response. It is clearly evident that as  $\Pi_1$  decreases the system becomes non-sinusoidal,

1000 and  $\Pi_1 = 0.001$  are presented in figures 4.17 (a) and (c) and figure 4.17 (b) and (d) respectively;  $\Pi_2 = 0.2$  is constant, and the reduced velocity is fixed at  $U^* = 40$  so that  $\Pi_1$  is varied by varying the mass ratio  $m^*$ .

Comparing figures 4.17 (c) and (d), with the respective  $C_y$  vs.  $\theta$  plot (figure 4.1(a)) it is clearly seen that at  $\Pi_1 = 0.001$  (figure 4.17 (d)) the body sustains induced angles which fall into the non-linear region of the  $C_y$  vs.  $\theta$  curve for long periods of time in a single oscillation cycle. In contrast the same period of time is significantly less when  $\Pi_1 = 1000$ . Thus, it is clear that the non-linearities of the forcing terms start dominating as  $\Pi_1$  decreases.

The underpinning reason for this phenomenon is that as  $\Pi_2$  is fixed,  $m^*$  decreases as  $\Pi_1$  reduces. Thus at  $\Pi_1 = 1000$  the system has comparatively high inertia ( $m^* = 201$ ) and therefore needs a greater force to accelerate, which results in the body oscillating such that its velocity generates an instantaneous angle of attack  $\theta$  which fall within the linear region of the  $C_y$  vs.  $\theta$  curve over the majority of the galloping cycle.

At  $\Pi_1 = 0.001$ , the inertia of the body is relatively low ( $m^* = 0.2$ ). As a result the body accelerates quickly to high velocities gaining higher induced angles quickly, and these high velocities are sustained for the majority of the time of a galloping period. These high velocities correspond to induced angles which falls in the non-linear region of the  $C_y$  vs.  $\theta$  curve (figure 4.1).

Thus, at high  $\Pi_1$  the significant forcing of the oscillatory system is governed by the linear terms of the forcing. As  $\Pi_1$  drops to a significantly low level, the non-linear terms of the forcing start affecting the system. As the linear frequency model does not account for the non-linear terms of the forcing function, a significant deviation of the linear frequency from the QSS frequency can be observed.

### Spectral analysis of the DNS data at low $\Pi_1$

The power spectral data of the velocity signals between  $\Pi_1 = 0.3$  and  $\Pi_1 = 1$  presented in figure 4.18, shows the galloping signal becoming weaker and the vortex shedding becoming more dominant as  $\Pi_1$  decreases. One interesting fact which can be observed on the vortex shedding frequency is that it slightly increases as  $\Pi_1$  reduced. This can be clearly observed by comparing the frequency values at the peaks which represent the vortex shedding of figures 4.18 and 4.11. The peak at the vortex shedding shifts to the right as  $\Pi_1$  reduces

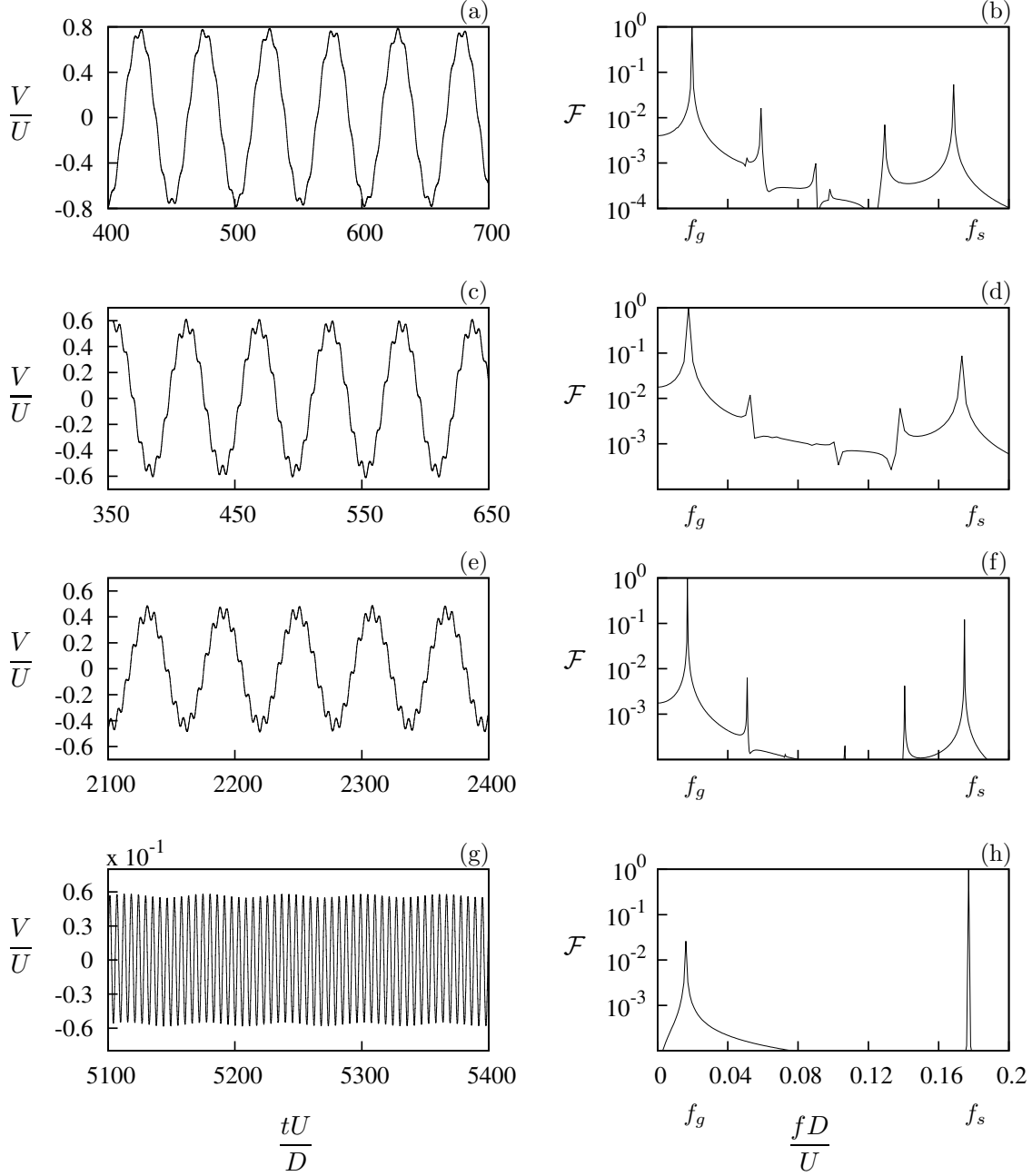


Figure 4.18: Velocity signal (right) and the corresponding power spectrum (left) of the DNS data at four values of  $\Pi_1$  at  $\Pi_2 = 0.15$ . (a) and (b)  $\Pi_1 = 1$ , (c) and (d)  $\Pi_1 = 0.5$ , (e) and (f)  $\Pi_1 = 0.4$ , (g) and (h)  $\Pi_1 = 0.3$ .  $f_g$  and  $f_s$  represents galloping and vortex shedding frequencies respectively.  $U^*$  is kept at 40 therefore the mass ratio decreases as  $\Pi_1$  decreases.

indicating some interaction between vortex shedding and galloping. This phenomenon is very subtle however, a significant difference can be observed by comparing figures 4.11 (h) ( $\Pi_1 = 1000$ ) and 4.18 (h) ( $\Pi_1 = 0.3$ ).

#### Comparison of $f_{lin}$ and $f_{QSS}$ in $\Pi_1$ $\Pi_2$ space

The data of figure 4.15 show how the various frequency measurements vary with respect to  $\Pi_1$  for a single value of  $\Pi_2 = 0.15$ . Here, this data is extended over a range of values of  $\Pi_2$  to produce contours of frequency as a function of  $\Pi_1$  and  $\Pi_2$ .

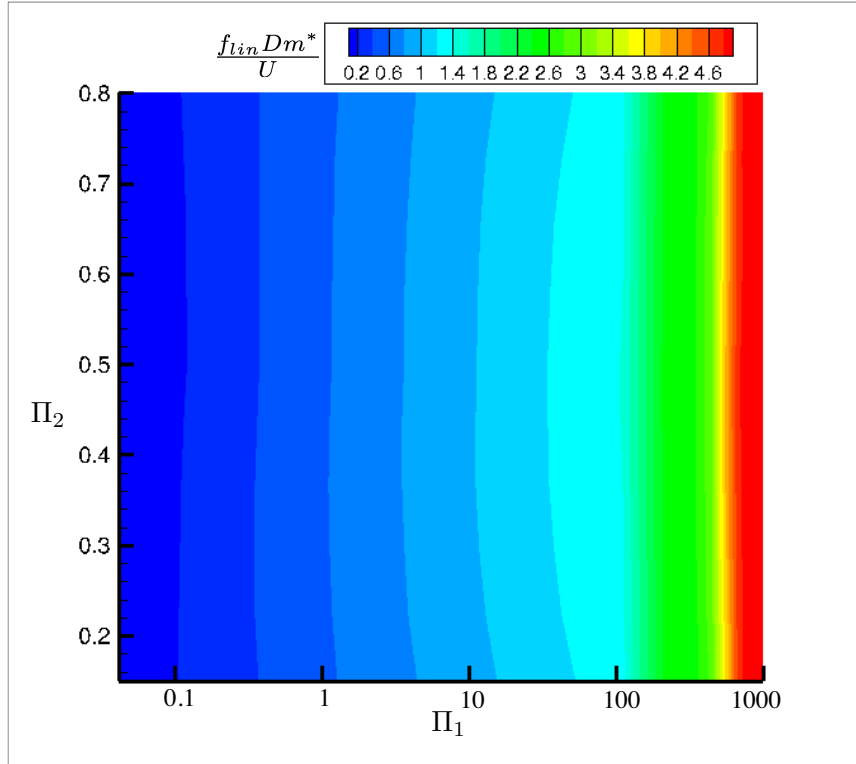


Figure 4.19: Contour plot of  $\frac{f_{lin} Dm^*}{U}$  in  $\Pi_1$   $\Pi_2$  space.

Figures 4.19, 4.20, 4.21 show the non dimensionalised  $f_{lin}$ ,  $f_{QSS}$  and  $f_{DNS}$  respectively. Essentially, both frequencies tend to be functions of  $\Pi_1$ , with very little dependence on  $\Pi_2$ . This is shown by the essentially straight vertical contours in figures 4.19, 4.20, 4.21.

The lower boundary of  $\Pi_1$  for the DNS results was limited  $\Pi_1 = 10$ . As discussed in

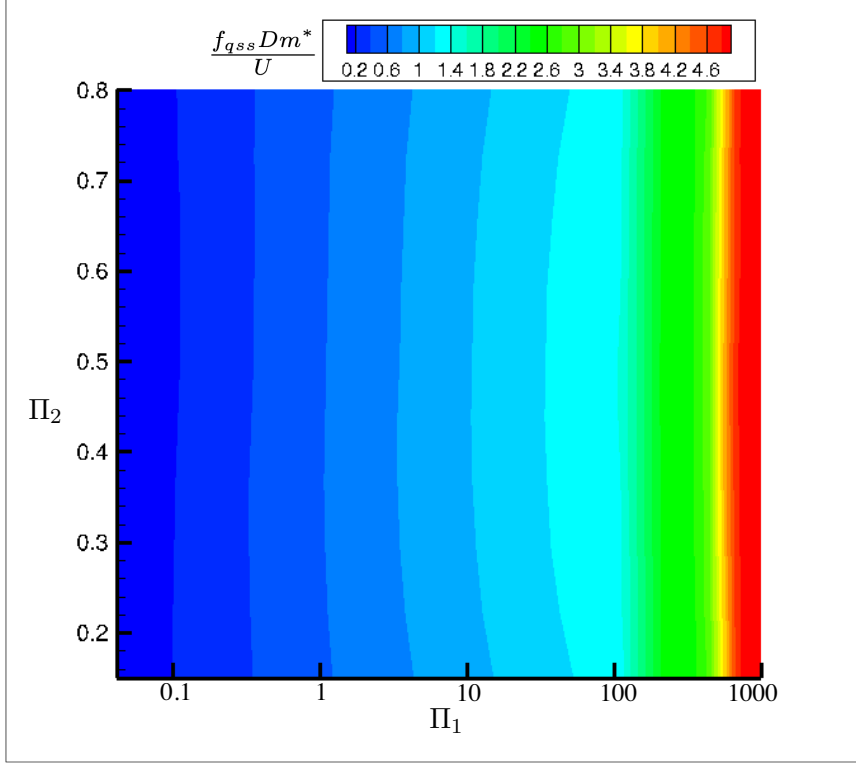


Figure 4.20: Contour plot of  $\frac{f_{qss}}{f}$  in  $\Pi_1$   $\Pi_2$  space.

section 4.2.2, vortex shedding becomes more dominant and galloping becomes weaker as  $\Pi_1$  reduces. Further, as  $\Pi_2$  increases the galloping signal further weakens. Because of this, it was difficult or impossible to obtain a reliable galloping signal through DNS simulations as  $\Pi_2$  increases. Thus, the lower boundary of  $\Pi_1$  was set where DNS data can be obtained across the range of  $\Pi_2$  considered for power transfer ( $\Pi_2$  0.15 – 0.8). The ratio between  $f_{lin}$  and  $f_{DNS}$  over this range is presented in figure 4.22. The figure shows that over this range, the ratio is between 0.9 and 1, showing a good agreement between the two frequencies. Thus, the expression formulated for the frequency presented in equation (4.16), formed by linearising the equation of motion and using the newly formulated parameters  $\Pi_1$  and  $\Pi_2$ , can be used as a model for prediction of the frequency of an energy harvesting system.

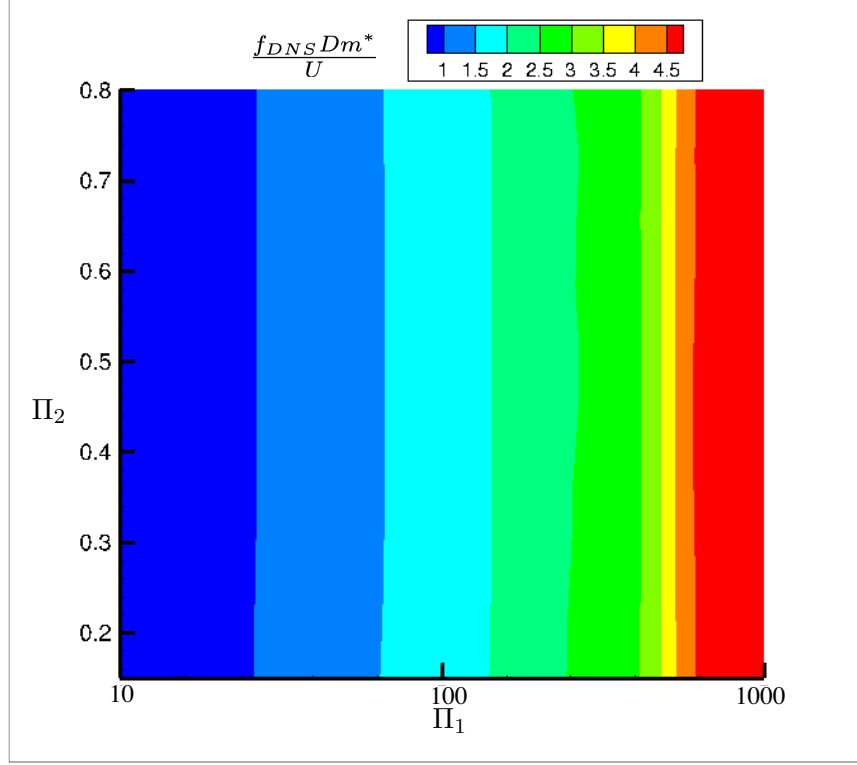


Figure 4.21: Contour plot of  $\frac{f_{dns}}{f}$  in  $\Pi_1$   $\Pi_2$  space.

### 4.3 Summary of analysis of power transfer using the QSS model

Suitable scaling parameters for galloping have been formulated. These parameters  $\Pi_1$ , a combined mass-stiffness, and  $\Pi_2$ , a combined mass-damping, were formulated through the natural time-scales found from the linearised quasi-steady state model.

The power transfer of a square body under fluid-elastic galloping was analysed by solving the quasi-steady state oscillator model equation using numerical integration. Power data were presented in terms of both traditional VIV and the newly formulated scaling parameters. A good collapse for predicted output of power was obtained using the newly formulated dimensionless groups ( $\Pi_1$ ,  $\Pi_2$ ) in comparison with the classical VIV parameters ,i.e.,  $\zeta$  and  $U^*$ . The collapsed data using the dimensionless groups strengthens the argument that the velocity amplitude and the power transfer of the system do not depend on the



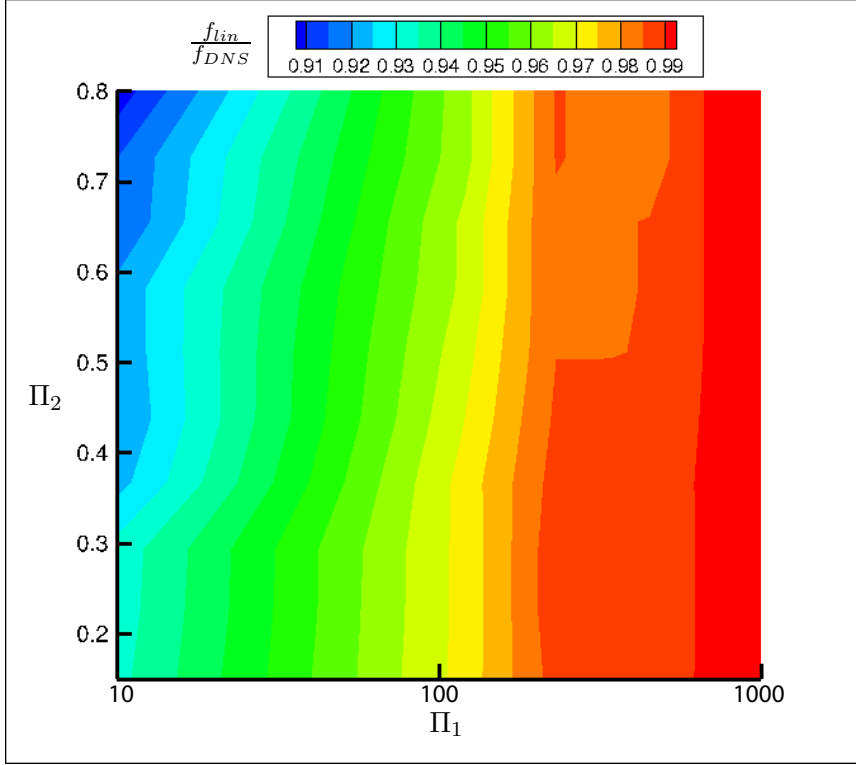


Figure 4.22: Contour plot of  $\frac{f_{lin}}{f_{DNS}}$  in  $\Pi_1$   $\Pi_2$  space. The linear frequency  $f_{lin}$  provides a good prediction of the DNS frequency over the range of  $\Pi_1$  plotted here.

natural frequency of the system over a large range of natural frequencies.

Even though  $m^*$  is an independent parameter as shown in equation 4.8, the results showed that the system is essentially a function of  $\Pi_1$  and  $\Pi_2$  only. This seems to be explained by inspection of equation 4.8, which shows that  $m^*$  only has an impact on the forcing terms which are non-linear in relation to the body velocity. For these terms to be appreciable, the velocity of the body (and therefore the induced angle of attack) needs to be very high, which appears not to be the case for the range of parameters tested here.

In comparison with the direct numerical simulation data, it can be concluded that the QSS model provides a good estimate of the power output of the system when  $\Pi_1$  is relatively high. However, at low values of  $\Pi_1$ , the prediction is not close due to the fact that the QSS model does not account for the influence of vortex shedding which is seen to be relatively increasing as  $\Pi_1$  is decreased. However, the QSS model does provide a

### 4.3. SUMMARY OF ANALYSIS OF POWER TRANSFER USING THE QSS MODEL

---

reasonable prediction of the value of  $\Pi_2$  at which maximum power is produced. Both the error in predicted maximum power between the QSS and the DNS models, and the relative power of the vortex shedding have been quantified and scaled similarly to  $1/\sqrt{\Pi_1}$ .

From the eigenvalues of the system from the linearised QSS model, an expression for the frequency of the system was formulated in terms of  $\Pi_1$  and  $\Pi_2$  which was defined as the linear frequency  $f_{lin}$ .

Comparison of frequency data obtained using the QSS model, linear frequency and DNS simulations shows a deviation from the undamped natural frequency of the system at  $\Pi_1 < 10$ . The linear frequency showed a rapid decrease with further decreases in  $\Pi_1$  for  $\Pi_1 < 1$ . It is concluded that when  $\Pi_1$  drops to a significantly low level, the non-linear terms of the forcing function of the system start affecting the system. As these non-linearities are not accounted in the linearised QSS model which is used to formulate  $f_{lin}$ , a significant deviation of the linear frequency from the QSS frequency can be observed.

The linear frequency agreed well with the DNS results within the boundaries of consideration. The lower boundary of  $\Pi_1$  was limited to  $\Pi_1 = 10$  as it was the lower limit where DNS data can be obtained across the range of  $\Pi_2$  considered for power transfer ( $\Pi_2$  0.15 – 0.8). However, as  $\Pi_1$  considered for energy transfer are  $\Pi_1 > 10$ , it can be concluded that expression formulated for the frequency of the system obtained using the newly formulated parameters  $\Pi_1$  and  $\Pi_2$  can be used as a model for prediction of the frequency of an energy harvesting system.

## CHAPTER 5

---

# OPTIMIZATION OF THE CROSS SECTION FOR POWER EXTRACTION

### 5.1 Introduction

Galloping is due to an increase in mean induced lift force  $C_y$  with an increase in the instantaneous induced angle of attack. This instantaneous angle of attack is directly related to the transverse velocity - an increase in angle of attack implies an increase in velocity. This increase in mean lift force is created by an increase in the difference in mean pressure on the upper and lower sides of the body. The mean pressure on each side of the body is related to the structure of the mean shear layer, in particular to the separation and potential reattachment of this shear layer, and the size of any resulting recirculation region. An increase in angle of attack forces one shear layer (the lower one in figure 2.4) closer to the wall, meaning a high speed region is placed close to this wall. A simple consideration of Bernoulli's equation shows that this high speed region should result in a region of low pressure. This low pressure on the upper side results in a positive pressure difference between the lower and upper sides, and thus a positive mean lift. The fact that this mean lift occurs as a function of the angle of attack, and therefore the transverse velocity, implies that this transverse forcing should be in phase with the transverse velocity.

From equation 3.2 discussed in section 3.3 it is clear that the power transferred from fluid to the body is a function of the induced forcing  $F_y$  and the transverse velocity  $\dot{y}$ .

The sign of the average power represents the direction of power transfer; positive power represents the power transfer from fluid to the body, negative power represents power transferring from body to the fluid. Thus, according to equation 3.2 it can be deduced that if there is a scenario where both high induced forcing and high transverse velocities are present, higher power output can be achieved.

This can be related directly to the shape of the  $C_y$  vs.  $\theta$  curve. To optimize power transfer this curve should,

- have a high gradient  $\partial C_y / \partial \theta$  at  $\theta = 0$
- a large maximum  $C_y$
- this maximum  $C_y$  should occur at a high value of  $\theta$

All of these features can be influenced by the cross section of the body which is galloping. Therefore, if the geometric features of the cross section that influence these curve features can be identified, an informed search for an optimal cross section for power extraction can be undertaken. The major features of the body that influence these  $C_y$  vs.  $\theta$  curve parameters are discussed below.

Luo et al. (1994), showed that the afterbody of the cross section has a direct impact on the  $C_y$  vs.  $\theta$  curve. One interesting observation of this study was that inhibiting the shear layer re-attachment results in a higher peak induced force coefficient  $C_y$  occurring at high induced angles (high transverse velocities). The opposite of this result was discussed by Robertson et al. (2003) where long rectangular cross sections did not exhibit galloping due to shear layer reattachment at low  $\theta$ . Furthermore, Luo et al. (1994) have discussed the impact of the reattachment of the shear layer at the trailing edge. As  $\theta$  is further increased beyond the angle at which reattachment occurs, the enclosed “bubble” region of the separated reattached shear layer shrinks in size reducing the difference in suction in the top and bottom sides of the body and results in a reduction in  $C_y$  (refer section 2.1.3).

Therefore, it can be hypothesised that a higher power transfer can be obtained by inhibiting the shear layer re-attachment.

Here, the influence of the shear layer and its reattachment on the mean power is discussed. It is crucial to keep the shear layer closer to the body for galloping; if it moves

too far from the body, the relationship between a separated shear layer inducing a high velocity, and therefore low pressure, is lost. Thus, a cross section which has a straight initial section (which provides some initial streamlining) followed by a slanting section to inhibit the shear layer, had to be considered for analysis. Therefore, a cross section which is a hybrid of a rectangle and a triangle is considered, as illustrated in figure 5.1. This cross section was essentially developed by slating the afterbody of the square section as illustrated in figure 5.1. The cross section is transformed gradually by manipulating the ratio of two lengths, the first being the length of the straight section, and the second being the streamwise length of the entire body. This cross section provides the flexibility of gradually inhibiting the shear layer reattachment while having the initial streamlining of the shear layers to keep the shear layers reasonably close to the body to sustain galloping.

The force data are presented for each stationary cross section. This is followed by presentation of extracted power curves, calculate from the QSS model using this force data for each new body. Based on the QSS power data, an optimum cross section for power extraction, from the family of cross sections that have been tested, is identified.

The main features of the generated  $C_y$  vs.  $\theta$  curves for the new bodies are identified and linked to the flow structure present by analysing the mean surface pressure and flow velocity data. Following this, a comparison is made between QSS and DNS mean power on the cross section which provides an optimum mean power.

A final summary is presented outlining that the behaviour of the shear layers is a controlling factor for mean power output. The preliminary design considerations to obtain an optimum power output should therefore focus on the manipulation of these shear layers.

### 5.2 Influence of the shear layers

In a typical cross section which sustains galloping, the induced lift  $C_y$  increases with increasing induced angle  $\theta$  until it reaches a maximum value of  $C_y$  where the shear layer reattachment occurs. The lift force then decreases as  $\theta$  is further increased. The underlying mechanism for this behaviour is discussed in detail in section 2.1.3.

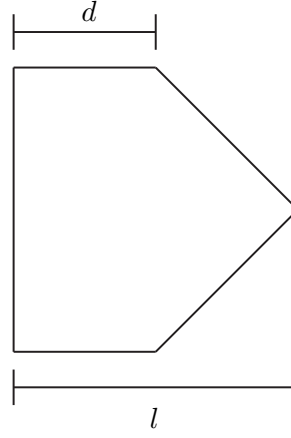


Figure 5.1: Illustration of the hybrid cross section (combination of a square and a triangle) obtained by tapering the afterbody of the square. The afterbody was changed by changing the ratio of  $\frac{d}{l}$ . Hence, data were obtained for  $\frac{d}{l} = 1, 0.75, 0.5, 0.25$  and 0 were considered in this study.

### Selection of the cross section

Several key factors have been considered leading to the selection of a suitable cross section for this analysis. These key factors are:

- The cross section should have a bluff front face with sharp upstream corners for the flow to separate at the leading edges;
- As the proximity of shear layers to the body plays a vital role in creating  $C_y$  (Parkinson, 1989), the cross section should have a basic level of streamlining.
- The cross section should consist of a geometric profile in the afterbody, to inhibit or delay the shear layer reattachment.

The square cross section which is considered as the base cross section in this study satisfies the first two criteria of the selection process. Therefore, in order to inhibit the shear layer reattachment, the top and bottom sides of the trailing edges of the square are tapered off and a hybrid cross section of a rectangle and a triangle (illustrated in figure 5.1), i.e, a pentagon is produced. This cross section satisfies all criteria in the cross section selection process. Another advantage of this cross section is the inhibition of the shear

## 5. OPTIMIZATION OF THE CROSS SECTION FOR POWER EXTRACTION

---

layer can be varied systematically by varying one variable which is  $\frac{d}{l}$ . The ratio  $\frac{d}{l}$  was varied from 1 to zero in increments of 0.25 where 1 is the square cross section and 0 is an isosceles triangle.

### 5.3 Static body results

$\frac{d}{l}$	$a_1$	$a_3$	$a_5$	$a_7$	Overlap range
0	-2.30617	-269.075	-59.2929	4.74389	20.5° – 23.5°
	-5.08342	-56.5390	-160.505	-105.773	
	4.40685	19.9213	22.8894	7.68556	28.6° – 28.7°
0.25	-0.605146	-19.4346	-82.4463	-94.4226	30.1° – 30.2°
	2.50538	9.91021	10.2712	3.94112	
0.5	1.44734	4.83885	-166.900	-983.072	14° – 16°
	1.51455e	15.8476	52.5465	62.8067	
0.75	1.76938	35.2630	-345.562	-10072.7	11.03° – 11.11°
	1.77553	43.0120	262.983	638.484	

Table 5.1: Coefficient values used in the 7th order interpolation polynomial at  $Re = 200$ . Data present for  $\frac{d}{l} = 0 - 0.75$  at increments of 0.25. Multiple polynomials were used to attain a better fit. The plot of the compound fit is presented in figure 5.2. The “Overlap” range refers to the range of angles which the transition of the two polynomials take place.

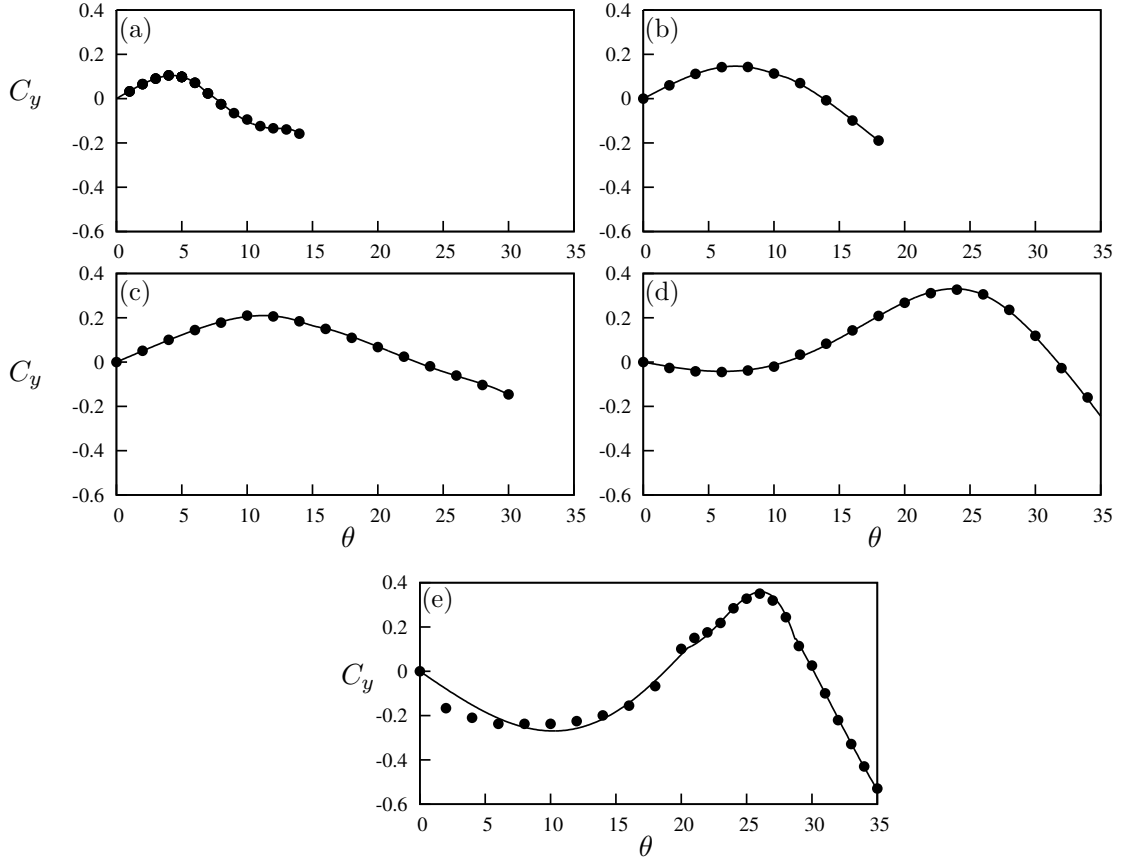


Figure 5.2: Induced lift coefficient  $C_y$  at different angles for selected cross sections. Data presented for cross sections, (a) square, (b)  $\frac{d}{l} = 0.75$ , (c)  $\frac{d}{l} = 0.5$ , (d)  $\frac{d}{l} = 0.25$  and (e) triangle. Points ( $\bullet$ ) are predicted from the static body simulations and the curves are the compound 7<sup>th</sup> order polynomials.

Stationary time averaged  $C_y$  results were obtained for cross sections where  $\frac{d}{l} = 1, 0.75, 0.5, 0.25$  and 0 using DNS at  $Re = 200$ . Table 5.1 shows the coefficients of the 7<sup>th</sup> order curve fitting for each cross section. In order to achieve a better fit, piecewise interpolation using multiple 7<sup>th</sup> order polynomials were incorporated for a single cross section. During the curve fitting process more importance was given to accurately fitting the positive portion of the  $C_y$  curve, as the power transfer from the fluid to the body only occurs in this region.

The  $C_y$  vs.  $\theta$  curves in figure 5.2 show that the peak value of  $C_y$  shifts to the right as  $\frac{d}{l}$  is increased, hence, the peak  $C_y$  occurs at higher induced angles. These data agree with Luo et al. (1994) where the peak of the maximum  $C_y$  value was shifted to higher induced



## 5. OPTIMIZATION OF THE CROSS SECTION FOR POWER EXTRACTION

---

angles when reattachment was delayed on a trapezoidal body. As  $\theta$  is proportional to the transverse velocity of the body via  $\tan \theta = \frac{\dot{y}}{U}$ , the peak value of  $C_y$  occurs at high induced velocities as  $\frac{d}{l}$  is decreased. Therefore, bodies with a short straight section, or small  $\frac{d}{l}$ , satisfy one of the three conditions required to optimize the power transfer.

However, a complicating factor is the appearance of a negative region on the  $C_y$  vs.  $\theta$  curves for cross sections where  $\frac{d}{l} \leq 0.25$ . Here, initially  $C_y$  decreases as  $\theta$  is increased and only increases after reaching a minimum, nonzero value of  $\theta$ . The presence of this negative portion is an indication of unfavourable power transfer, i.e. power transferred from body to the fluid as the direction of the force and velocity vectors are out of phase. This implies that when the induced angle of attack is low (when the transverse velocity is low), power transfer is from the body to the fluid, but when the transverse velocity is high, power transfer is from the fluid to the body. This means that the direction of power transfer can be different at different points in the oscillation cycle. This will be further discussed in the upcoming section 5.5.

### 5.4 QSS Mean power output

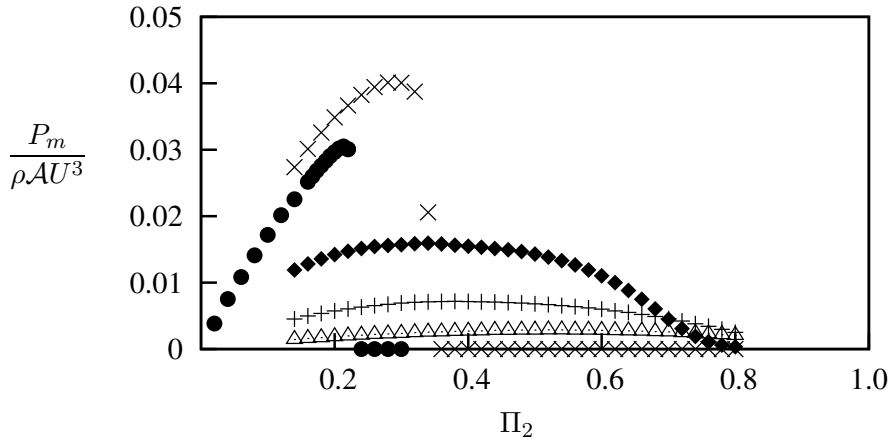


Figure 5.3: Dimensionless mean power obtained using QSS model as a function of  $\Pi_2$ . Data presented for five selected cross sections, square ( $\triangle$ ),  $\frac{d}{l} = 0.75$  ( $+$ ),  $\frac{d}{l} = 0.5$  ( $\blacklozenge$ ),  $\frac{d}{l} = 0.25$  ( $\times$ ) and triangle ( $\bullet$ ) at  $Re = 200$ ,  $\Pi_1 = 100$ .

Mean power output predictions are obtained for these different cross sections using

the QSS model and the stationary lift data shown in figure 5.2 used as inputs to the QSS model. Figure 5.3 shows the mean power vs.  $\Pi_2$  for different cross sections namely  $\frac{d}{l} = 1, 0.75, 0.5, 0.25$  and 0. The cross sections are divided into two classes; high ( $\frac{d}{l} > 0.25$ ) and low ( $\frac{d}{l} \leq 0.25$ ). The general trends of power follows the trends observed in section 4.1.3 for the square body in both classes. The mean power first increases, then peaks, and then reduces as  $\Pi_2$  is increased. For high  $\frac{d}{l}$ , the overall shape of the curves is similar, however as  $\frac{d}{l}$  is decreased, the amount of power increases. For low  $\frac{d}{l}$ , the overall curve shape is markedly different; power first increases with  $\Pi_2$ , then peaks, and then drops dramatically. The power extracted also appears to decrease with a decrease in  $\frac{d}{l}$ . Furthermore, negative regions of the  $C_y$  vs.  $\theta$  curves in figure 5.2 appear in the low  $\frac{d}{l}$  cases. The change in the trend of power, and the appearance of a negative region in the  $C_y$ , for the low  $\frac{d}{l}$  cases clearly indicates that there is a distinct change in the flow structure for these cases. This fact is further investigated in section 5.5.

## 5.5 Investigation of flow characteristics at low $\frac{d}{l}$ cases

The analysis of the mean power and the static body results showed that there is a significant change in the flow structure at low  $\frac{d}{l}$  cases. As the change in mean  $C_y$  is the only input from the fluid dynamics in the QSS model, the distinct features in the  $C_y$  vs.  $\theta$  curves provide an indication of the change in flow structure which results in the distinct change in mean power discussed in section 5.4. The main difference between high and low  $\frac{d}{l}$  cases is the presence of the negative region in the  $C_y$  vs.  $\theta$  curves. Thus, it is of interest to investigate the underpinning reason for the negative region in the low ratios of  $\frac{d}{l}$ . The triangle ( $\frac{d}{l} = 0$ ) which produced the largest negative region out of the cross sections considered, is taken as the representative of the low  $\frac{d}{l}$  cases for further investigation.

### 5.5.1 Surface pressure

The driving force of galloping is the induced force  $F_y$  created as a result of the freestream velocity of the fluid and the transverse velocity of the body. As discussed in section 2.1.3 the pressure difference of the upper and lower sides of the body (figure 2.4) creates this induced force as a result of the relative proximities of the shear layers to the respective

## 5. OPTIMIZATION OF THE CROSS SECTION FOR POWER EXTRACTION

---

sides. Thus, here, surface pressure data on the time averaged flows on the stationary cross section is analysed.

Time averaged (to filter out the influence of vortex shedding) surface pressure data on the top and bottom surfaces of the cross sections at  $\theta = 4^\circ$ ,  $\theta = 16^\circ$  and  $\theta = 21^\circ$  were obtained for the isosceles triangle. These angles correspond to the regions of the  $C_y$  vs  $\theta$  curve of the triangle where:  $C_y$  is negative, but increasing in magnitude;  $C_y$  is negative, but decreasing in magnitude and  $C_y$  is significantly positive.

Figure 5.4 shows the surface pressure of the top and bottom surfaces of the body ( $\frac{d}{l} = 0$ ) as a function of the distance from the leading edge. At  $\theta = 4^\circ$ , the pressure on the bottom of the body is greater than the top at practically all distances. As a result, a pressure difference is created and a force is generated in the upward direction which according to the sign convention in figure 2.1, is against the velocity of the body, hence giving a negative  $C_y$ .

As  $\theta$  is increased to  $16^\circ$ , (figure 5.4 (b)) the gap between the surface pressure at the leading edge of the top and the bottom sides reduces. For small distances downstream from the leading edge, the pressure on the top surface is greater than that on the bottom. This effect results in a reduction of the magnitude of  $C_y$  (although it is still negative).

As  $\theta$  is further increased to  $21^\circ$ , (figure 5.4 (c)) the surface pressure on the top side becomes greater than the bottom over the majority of the body. Therefore, the net effect of the pressure difference is a positive  $C_y$  which is the driving force  $F_y$ , now in phase with the velocity of the body.

### 5.5.2 Velocity profiles at the points of flow separation

Flow separation at the leading edge is equally vital as the afterbody of the cross section for galloping, as it creates the shear layers which sustain it. Two wall jets are created from the top and bottom leading edges. A clearer explanation of the behaviour of the pressures at the top and bottom edges can be gained from a comparison of the velocity profiles of the top and bottom wall jets.

Thus, mean velocity magnitude data of the flow were obtained along two lines parallel to the front wall of the cross section, one starting at the top and the other starting at the bottom leading edges of the cross section, spreading outward as illustrated in figure 5.5.

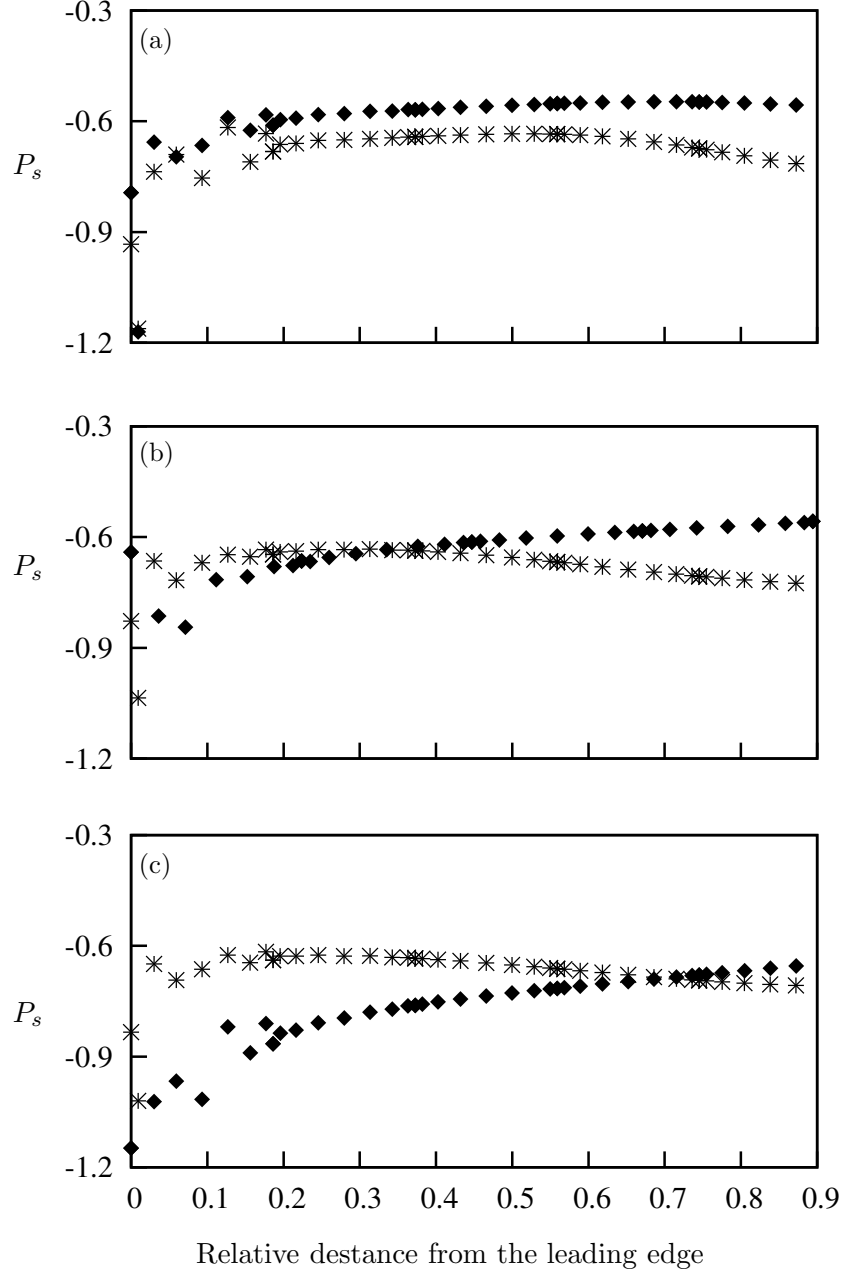


Figure 5.4: Surface pressure of top (\*) and bottom (◆) surfaces of the static triangular cross section at (a)  $\theta = 4^\circ$ , (b)  $\theta = 16^\circ$  and (c)  $\theta = 21^\circ$ . A clear pressure difference is visible between the surfaces. The top surface comparatively has more negative pressure where a lift is created which results in a negative  $C_y$  at  $4^\circ$  and reduces as  $\theta$  is increased, while the vice versa occurs at the top surface.

## 5. OPTIMIZATION OF THE CROSS SECTION FOR POWER EXTRACTION

---

The lengths of these lines were equal to the width of the cross section. Data were obtained for the same cases presented earlier i.e. isosceles triangle ( $\frac{d}{l} = 0$ ) at  $\theta = 4^\circ$ ,  $\theta = 16^\circ$  and  $\theta = 21^\circ$ .

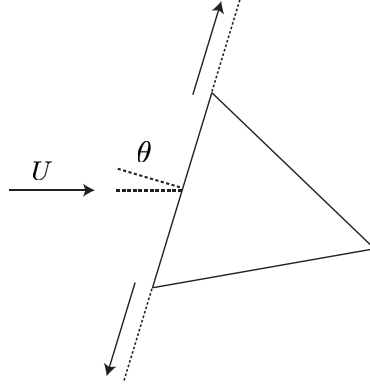


Figure 5.5: Illustration of the lines along which the flow velocity magnitudes have been extracted. The data have been extracted along a line starting from the separation points in the outward direction (shown with arrows) for the top and bottom surfaces.

The maximum velocity magnitude in the top wall jet at  $\theta = 4^\circ$  (figure 5.6 (a)) is higher than that in the corresponding bottom wall jet, leading to a lower pressure at the top edge. However, the velocity magnitude in the bottom wall jet becomes greater than that in the top wall jet at  $\theta = 16^\circ$ . The difference between the top and bottom velocity magnitude in these wall jets tends to increase as  $\theta$  is increased to  $21^\circ$ , where the velocity magnitude at the bottom is greater than at the top (figure 5.6 (c)). This effectively creates the pressure difference (according to the Bernoulli's principle ) shown in figure 5.4 (c), which leads to a positive  $C_y$  and results in a forcing which is in phase with the velocity of the body.

### 5.5.3 Mean streamlines

The shear layers of the body can be visualised using the magnitude of the strain rate tensor. The strain rate is directly proportional to the shear stress and so it will be high in the shear layers. Instantaneous flow-field data consists of vortex shedding on top of the shear layers. Hence, the flow-field data are time averaged over a vortex shedding cycle to filter out the vortex shedding .

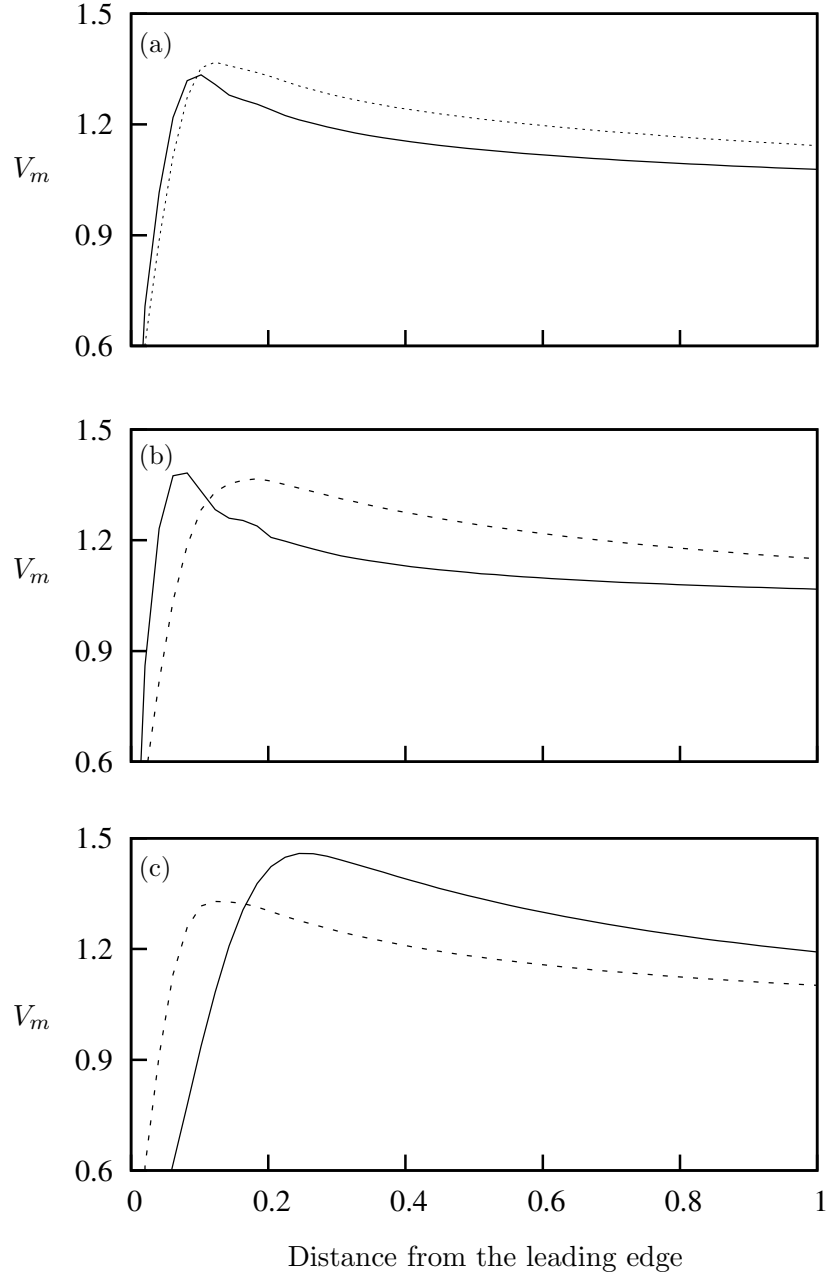


Figure 5.6: Velocity magnitudes of the flow along a line parallel to the front surface spreading towards top (---) and bottom (—) boundaries (figure 5.5). These two lines (for the top and bottom surfaces) start from the top and bottom leading edges of the triangular cross section. Data present (a)  $\alpha = 4^\circ$ , (b)  $\alpha = 16^\circ$  and (c)  $\alpha = 21^\circ$ .

The strain rate tensor of the flow can be expressed as,

$$\varphi = \frac{1}{2} \begin{bmatrix} 2\frac{\partial u}{\partial x} & \frac{\partial u}{\partial y} + \frac{\partial v}{\partial x} \\ \frac{\partial v}{\partial x} + \frac{\partial u}{\partial y} & 2\frac{\partial v}{\partial y} \end{bmatrix} \quad (5.1)$$

thus the magnitude of the strain rate tensor becomes,

$$|\varphi| = \frac{1}{2} \left( 4\frac{\partial u}{\partial x} \frac{\partial v}{\partial y} + \left( \frac{\partial u}{\partial y} + \frac{\partial v}{\partial x} \right)^2 \right) \quad (5.2)$$

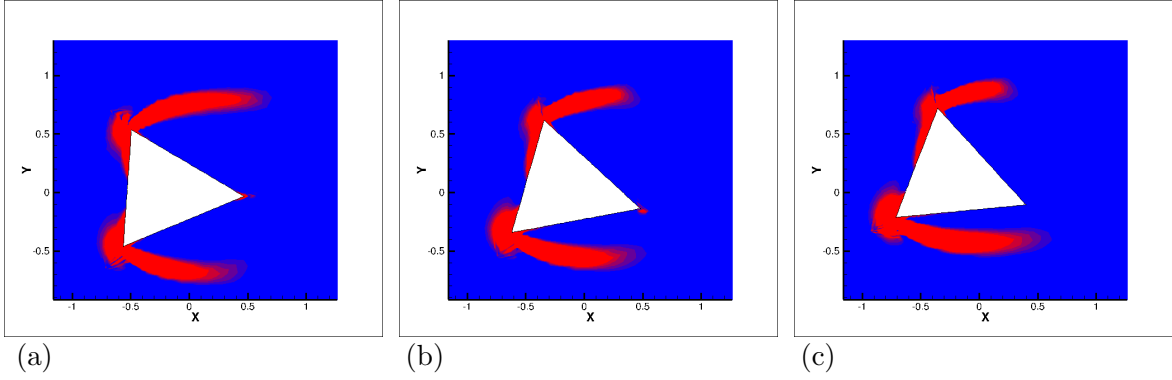


Figure 5.7: Contours of the magnitude of the shear strain rate of time averaged flow field on the stationary isosceles triangle ( $\frac{d}{l} = 0$ ) at  $Re = 200$  at different incidence angles. (a)  $4^\circ$  ( negative value of  $C_y$  that is further decreasing with increasing  $\theta$ ), (b)  $16^\circ$  ( negative value of  $C_y$  that is increasing with increasing  $\theta$ ) and (c)  $21^\circ$  (a significantly positive value of  $C_y$ ). The bottom shear layer comes closer to the bottom wall and as the angle of incidence increases.

Contours of the magnitude of the strain rate tensor of the time averaged flow-field of the stationary isosceles triangle at  $\theta = 4^\circ$ ,  $\theta = 16^\circ$  and  $\theta = 21^\circ$  are presented in figure 5.7. Here, it can be observed that the proximity of the bottom shear layer increases as  $\theta$  is increased from  $4^\circ - 21^\circ$ .

By comparing the pressure and the velocity plots together with the flow-field data, it is evident that there are two mechanisms governing the transverse forcing. The first mechanism is the pressure difference in each shear layer, created as a result of the uneven distribution of the flow created due to the profile and positioning (angle of attack) of the geometry. This uneven distribution creates a different speed wall jet on either side, and a

simple consideration of Bernoulli's equation suggests the higher speed jet will have a lower pressure. This forcing occurs out of phase or in the opposite direction of the transverse velocity of the body, as the lower speed (higher pressure) jet is formed on the lower side of the body (when the body is travelling down). The second mechanism is the relative proximity of the top and bottom shear layers. Regardless of the pressure in each shear layer, that pressure will have a larger influence on the force on the body the closer the shear layer is to the body. So, there are two ways to manipulate the force from the shear layers; increase the pressure difference between the shear layers by increasing the difference between the flow in each shear layer (a "streaming effect"); move the shear layers closer or further from the body (the "proximity effect").

Initially at  $\theta = 4^\circ$  the streaming effect dominates. This can be observed comparing figures 5.7 (a) to (b) and (c). The bottom shear layer is far from the body at  $\theta = 4^\circ$ , hence the proximity effect is low. This results in the negative  $C_y$ .

As  $\theta$  is increased first to  $\theta = 16^\circ$  and then to  $21^\circ$ , the proximity of the bottom shear layer to the wall of the body increases (figure 5.7 (b) and (c)), and thus the proximity effect becomes more dominant. At least for the  $\theta = 21^\circ$  case, this creates the positive region of the  $C_y$  vs.  $\theta$  curve.

## 5.6 Fluid-structure interaction (DNS) results

### 5.6.1 Mean power data

The main limitation of the QSS model as discussed in section 4.1.7 is considering the induced transverse force  $F_y$  as the sole driving force of the system, generated by the relative proximity of the shear layers (refer section 2.1.3). However, it was concluded in chapter 4 the QSS model provides good agreement between QSS and DNS for power at high  $\Pi_1$  for the square cross section, even though the relative error increased as  $\Pi_1$  decreased due to the significant influence of vortex shedding.

A comparison study between QSS and DNS mean power was carried out on the different cross sections considered at high  $\Pi_1$  (i.e.  $\Pi_1 = 1000$ ) and presented in figure 5.8.

Both DNS and QSS mean power data (figure 5.8) show similar trends. The maximum mean extracted power increases as  $\frac{d}{l}$  is decreased. These trends provide a reinforcement



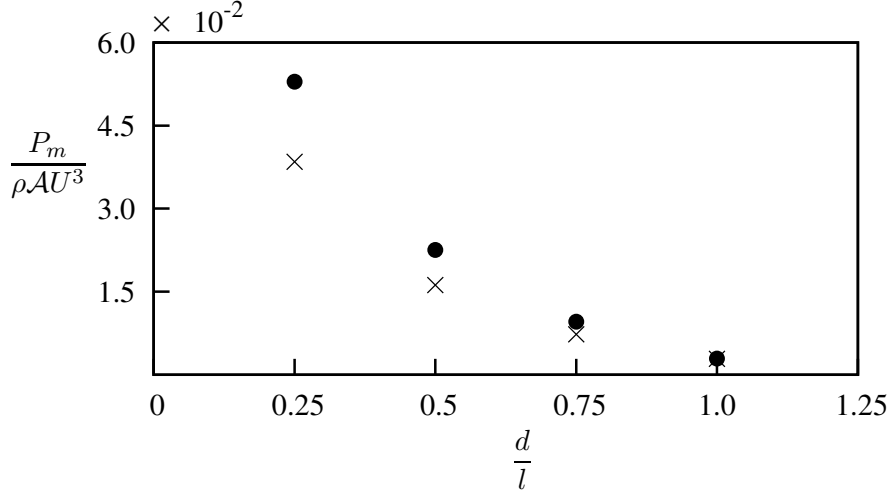


Figure 5.8: Comparison of the maximum power obtained using DNS ( $\bullet$ ) and the QSS ( $\times$ ) model as a function of  $\frac{d}{l}$ . Data obtained at  $\Pi_1 = 1000$  ( $m^* = 201.3$ ) and  $Re = 200$ . Similar trends are present for both QSS and DNS data. A significant reduction in power could be observed as  $\frac{d}{l} \rightarrow 1$

to the hypothesis of attaining a higher power output through inhibition of the shear layer reattachment.

However, a significant error (calculated using equation 4.9) between QSS and DNS power could be observed as  $\frac{d}{l}$  decreases. The quantified errors presented in figure 5.9 shows an almost linear increase in the % error as  $\frac{d}{l} \rightarrow 0.25$ , with a maximum error of 35%.

### 5.6.2 Flow-field data

As a significant discrepancy between the QSS and DNS data was observed, further investigations were conducted in order to identify the cause of this error.

The QSS model assumes that the flow is quasi-static, meaning the instantaneous flow of the oscillating body at a particular induced angle  $\theta$ , is similar to that of a stationary body at the same induced angle. Thus, stream traces of the flow around the oscillatory body at selected instants of a single galloping cycle were compared against the stream traces of a similar stationary cross section at the induced angles produced at the considered points of the galloping cycle. The chosen cross section to perform this task was  $\frac{d}{l} = 0.25$  at  $\Pi_2 = 0.26$  which provided the maximum mean power among all cases considered. Three points of a

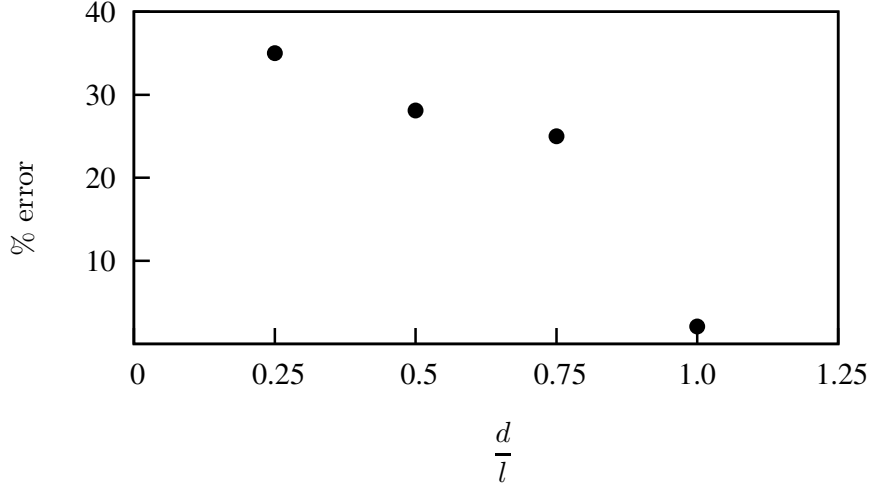


Figure 5.9: The percentage error calculated using equation 4.9 between the maximum power obtained using DNS data and predicted by QSS model as a function of  $\frac{d}{l}$ . The error reduces significantly as  $\frac{d}{l} \rightarrow 1$

galloping cycle was considered. These points corresponded to key instants of the velocity signal. The points considered were point 1 where  $\dot{y}$  is maximum, point 2 where  $\dot{y}$  is close to zero with a negative gradient and point 3 where  $\dot{y}$  is close to zero with a positive gradient. An illustration of these points is presented in figure 5.10.

It should be recalled that the QSS model assumes that only the long-time forces are important; the fluctuation in time at the frequency of the vortex shedding is assumed to play no role. Therefore, both stationary and the instantaneous oscillatory flow data were time averaged over a length of time equal to one vortex shedding cycle in order to filter the vortex shedding and have an estimate of the mean flow.

Figure 5.11 shows the time averaged stream functions for points 1, 2 and 3 and the stationary time averaged stream traces of the corresponding induced angles. Comparison between FSI and stationary data at point 1, where the transverse velocity is at its maximum, (Figure 5.11 (a) and (b)) shows a significant difference of the stream functions.

In contrast, at point 2 and 3 the stream functions at the leading edge of the FSI simulations are similar to those of the stationary simulations. At point 2 both the FSI (figure 5.11 (b)) and stationary case (figure 5.11 (c)) show similar flow behaviour until separation. A single circulation bubble at the top is formed in the FSI case where a symmetrical formation of the circulation bubbles could be observed in the stationary case.

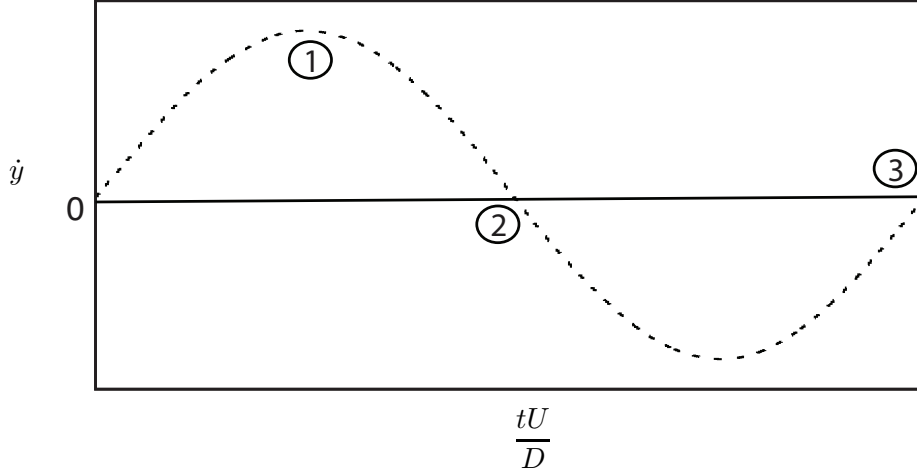


Figure 5.10: Illustration of the time history of velocity depicting the points considered to obtained time averaged stream traces. The points considered are: point 1 where  $\dot{y}$  is maximum, point 2 where  $\dot{y}$  is close to zero with a negative gradient and point 3 where  $\dot{y}$  is close to zero with a positive gradient

A similar behaviour of the stream functions could be observed between point 3 for FSI (figure 5.11 (d)) and stationary (figure 5.11 (e)) cases.

According to the assumptions of the QSS theory the flow-fields between the stationary and FSI cases at points 2 and 3 should be approximately identical as the induced velocities are zero and therefore the induced angles are zero. However, the observations on the corresponding FSI cases show a significant difference, indicating a significant deviation from the quasi-steady assumption.

Thus, from the analysis of the flow data it is clear that the QSS predictions deviates significantly for mean power predictions at decreasing  $\frac{d}{l}$ , as a result of the flow not being quasi-static. Thus, this violates the assumption of considering the time averaged fluid forces as the inputs of the oscillatory system creating a significant discrepancy between QSS and DNS mean power.

However, the QSS model does provide similar trends as the DNS predictions and therefore, can be used as a preliminary design and research tool to obtain data and conclusions to produce efficient galloping energy extraction systems.

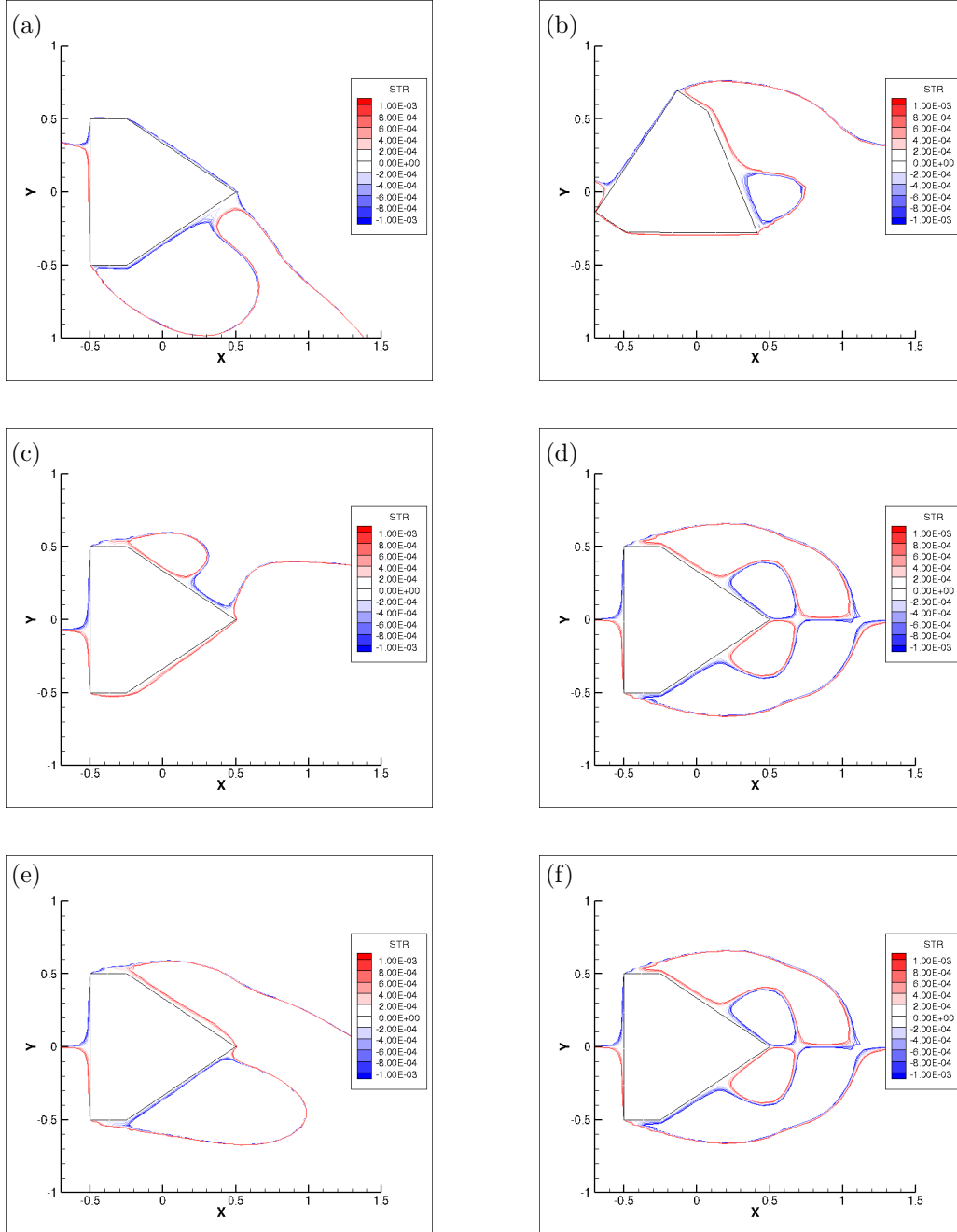


Figure 5.11: Time averaged stream functions of stationary and oscillating flow-fields of the hybrid cross section ( $\frac{d}{T} = 0.25$ ), averaged over a vortex shedding cycle. (a), (c) and (e) are the averaged stream functions of the oscillating case at  $t = 2295.763$  (point 1),  $t = 2305.897$  (point 2) and  $t = 2325.870$  (point 3). (b), (d) and (f) are the stream functions of the flow field of the stationary body corresponding to the induced angles of (a), (c) and (e).

## 5.7 Design considerations for a galloping energy extraction system through inhibition of shear layer reattachment.

From the QSS and DNS results it is clear that inhibition of the shear layer reattachment leads to higher energy output. However, it is to be noted that even though a higher power output could be obtained through inhibition of the shear layer reattachment, a region of adverse power transfer (body-to-fluid) will develop as  $\frac{d}{l}$  decreases. This can be observed through the negative region present in the  $C_y$  curves beyond  $\frac{d}{l} \leq 0.25$ . As this negative region develops the maximum extracted power reduces, which can be observed in the power curves (figure 5.3) where the maximum power at  $\frac{d}{l} = 0$  is less than  $\frac{d}{l} = 0.25$ .

This fact leads to one important design consideration for an optimum cross section. The optimal design would be a trade off between large positive values of  $C_y$  occurring at high angles of attack where significant power could be generated and the negative regions of  $C_y$  where the power transfer occurs in the opposite direction. Barrero-Gil et al. (2010) concluded that the first coefficient  $a_1$  should satisfy  $a_1 > 0$  in order to obtain good operation of an energy harvesting system, where it is furthermore explained in detail using the QSS model together with direct numerical simulations for FSI cases. The conclusion of Barrero-Gil could be considered as somewhat simplistic as cases of higher power output where  $a_1 < 0$  can be observed in figure 5.3. Thus, a more detailed statement to compliment Barrero-Gil is to obtain a cross section which produces a  $C_y$  vs.  $\theta$  curve with optimum balance between negative and positive regions.

As further consideration for future research, DNS and QSS work at  $0 < \frac{d}{l} < 0.25$  could be carried out to find the optimum ratio of  $\frac{d}{l}$  to obtain a maximum power output. Moreover, further work could be carried out to find ways to reduce the negative portion of the  $C_y$  curve by applying modifications to the cross section which can result in further optimisation of the geometry.

## 5.8 Summary

The primary objective of the work presented in this chapter was to test the hypothesis that higher power output could be obtained by inhibition of shear layer reattachment. This was done by incrementally tapering off the top and bottom sides of the trailing edges of the

square cross section. A negative region in the  $C_y$  vs.  $\theta$  curve was observed for  $\frac{d}{l} < 0.25$ . This region resulted in a power loss in a certain portion of the galloping cycle as the driving force  $F_y$  and the velocity  $\dot{y}$  were in opposite directions.

The mean power versus  $\Pi_2$  curves showed an increase in maximum power as  $\frac{d}{l}$  was decreased until  $\frac{d}{l} = 0.25$ . At  $\frac{d}{l} = 0$ , ( $\frac{P_m}{\rho AU^3} = 0.0304$  at  $\Pi_2 = 0.021$ ) the maximum power was less than at  $\frac{d}{l} = 0.25$  ( $\frac{P_m}{\rho AU^3} = 0.04$  at  $\Pi_2 = 0.028$ ), although the peak value of both the induced angle and  $C_y$  were greater in  $\frac{d}{l} = 0$  compared to  $\frac{d}{l} = 0.25$ . Further analysis of the  $C_y$  curve revealed that the negative region of  $\frac{d}{l} = 0$  was greater than that of  $\frac{d}{l} = 0.25$ , hence resulting in a lower maximum power output.

The surface pressure plots and the velocity magnitude profiles at the starting points of the wall jets revealed that there are two mechanisms governing the transverse forcing. The first mechanism is the pressure difference in each shear layer, or the “streaming effect”. The second mechanism was the relative proximity of the top and bottom shear layers, or the “proximity effect”.

Initially at  $\theta = 4^\circ$  the streaming effect dominated resulting the negative  $C_y$ . As  $\theta$  increased from  $\theta = 16^\circ$  to  $\theta = 21^\circ$  the proximity effect started dominating resulting in a positive  $C_y$ .

Comparison of the QSS and DNS predictions of maximum power showed similar trends. The maximum power increased as  $\frac{d}{l}$  decreased supporting the hypothesis of attaining higher power output through inhibition of shear layer reattachment. However, a significant error between the QSS and FSI simulations were observed as  $\frac{d}{l}$  was reduced.

Further investigations carried out using time averaged flow data concluded that the mean flow of FSI simulations had significant deviations from the DNS stationary simulations carried out at corresponding induced angles. This shows that the flow is essentially not quasi-static, violating the primary assumption of considering  $F_y$  as the sole driving force of the system. Yet, the QSS model can be used as a tool to obtain initial approximations to design galloping energy harvesting systems as QSS data produced similar trends as the FSI simulations.

In order to obtain an efficient galloping energy harvesting system through inhibition of shear layer reattachment, one key design consideration is to obtain a cross section which has the optimum balance between the negative and positive regions of the  $C_y$  vs.  $\theta$  curve.

## 5. OPTIMIZATION OF THE CROSS SECTION FOR POWER EXTRACTION

---

Inhibition of the shear layer reattachment through tapering of the trailing edge leads to higher power. However, as it approaches a triangle, a negative region of  $C_y$  emerges in the  $C_y$  vs.  $\theta$  curve which leads to adverse power transfer. This region keeps increasing between  $0 \leq \frac{d}{l} \leq 0.25$ . Thus as a result an optimum  $\frac{d}{l}$  should be obtained in order to get a balance between the negative and positive regions which leads to an optimal galloping energy harvesting system.

As for future research this method of attaining high power through inhibition of shear layer reattachment can be further developed by conducting more detailed investigations into the geometry to find ways to reduce the adverse power transfer which will lead to further increases in power output.

## CHAPTER 6

---

# CONCLUSIONS

This thesis explores the potential of obtaining useful energy from fluid-elastic galloping. This research has employed theoretical modelling and numerical simulations. The study was primarily focussed on understanding the energy transfer between the fluid and the structure.

Galloping being a phenomenon of fluid-structure interaction, two main objectives were identified during the selection of the scope of the research. These were understanding the underpinning structural parameters of the system, and understanding the fluid mechanics of the system and thereby attempting to optimise mean power output through manipulation of these mechanics.

New governing dimensionless groups for galloping namely,  $\Pi_1$  and  $\Pi_2$  were formulated using the natural times-scales of the linearised quasi-steady state model. Data were obtained for a square cross section. The formulated dimensionless groups  $\Pi_1$  and  $\Pi_2$  provided a good collapse for the predicted power output in comparison with the classical VIV parameters i.e.  $U^*$ ,  $m^*$  and  $\zeta$ . The data collapse as a result of using the dimensionless groups reinforce the argument that the velocity amplitude of the system and the power transfer of the system do not depend on the natural frequency of the system over a large range of natural frequencies.

Although this new formulation shows that the mass ratio  $m^*$  is an independent parameter, the findings show that the system is essentially a function of  $\Pi_1$  and  $\Pi_2$ . A close inspection of equation 4.8 reveals that  $m^*$  only has an impact on the non-linear forcing



## 6. CONCLUSIONS

---

terms in relation to the velocity of the body. Thus in order for these non-linear terms to be significant, the induced angle of attack and therefore, the velocity of the body needs to be very large, which is not the case for the range of parameters which were tested.

It can be concluded, through comparison between the quasi-steady state and direct numerical simulation data, that the quasi-steady state model provides a good approximation of the power output of the system when  $\Pi_1$  is relatively high. However, the QSS approximation deviates from DNS predictions at low values of  $\Pi_1$  due to the fact that QSS model does not account for interaction of the body with the unsteady forces created by vortex shedding which is shown to increase as  $\Pi_1$  is decreased. However, the QSS model does provide a reasonable prediction of the value of  $\Pi_2$  at which maximum power is produced. Both the error in predicted maximum power between the QSS and the DNS models and the relative power of the vortex shedding have been quantified and scale approximately as  $1/\sqrt{\Pi_1}$ .

An expression describing the frequency of the system was produced from the eigenvalues of the linearised QSS model, in terms of  $\Pi_1$  and  $\Pi_2$ . This frequency was defined as the linear frequency  $f_{lin}$  of the system. Frequency data obtained through this model were compared against the QSS model and DNS simulations.

The frequency data obtained through these three methods, namely, the QSS model, linear frequency and DNS simulations all showed a deviation from the undamped natural frequency of the system at  $\Pi_1 < 10$ . The linear frequency showed a rapid decrease at  $\Pi_1 < 1$ . It can be concluded that at  $\Pi_1$  where  $\Pi_1$  drops to a significant low level, the non-linear terms of the forcing function of the system start affecting the system. As these non-linearities are not accounted in the linearised QSS model which is used to formulate  $f_{lin}$  a significant deviation of the linear frequency from the QSS frequency can be observed.

The linear frequency agreed well with the DNS results within the boundaries of consideration. The lower boundary of  $\Pi_1$  was limited to  $\Pi_1 = 10$  as a clear deviation of  $f_{lin}$  and  $f_{DNS}$  was observed  $\Pi_1 < 10$ . However, as  $\Pi_1$  considered for energy transfer are  $\Pi_1 > 10$ , it can be concluded that expression formulated for the frequency of the system obtained using the newly formulated parameters  $\Pi_1$  and  $\Pi_2$  can be used as a model for prediction of the frequency of an energy harvesting system.

These conclusions support the first objective of this thesis which is: “*Understanding*

---

*the governing mechanical parameters of the system and isolate regions where a good power transfer could be obtained.”*

The second objective of this study was focused on optimisation of the governing fluid mechanics of the system in order to obtain a higher power output. The primary hypothesis was that inhibition of the shear layer reattachment would result in a higher power output. The square cross section was systematically tapered off into a hybrid rectangular/triangular body. The geometry was controlled by the length of the rectangular section compared the length of the triangular section,  $\frac{d}{l}$ . By changing the  $\frac{d}{l}$  ratio the body could be systematically tapered.

A negative region in the  $C_y$  vs.  $\theta$  curve was observed for  $\frac{d}{l} < 0.25$ . This region resulted in a power loss in a certain portion of the galloping cycle as the driving force  $F_y$  and the velocity  $\dot{y}$  were in opposite directions.

The mean power versus  $\Pi_2$  curves showed an increase in maximum power as  $\frac{d}{l}$  was decreased until  $\frac{d}{l} = 0.25$ . At  $\frac{d}{l} = 0$ , the maximum power ( $\frac{P_m}{\rho AU^3} = 0.0304$  at  $\Pi_2 = 0.021$ ) was less than at  $\frac{d}{l} = 0.25$  ( $\frac{P_m}{\rho AU^3} = 0.04$  at  $\Pi_2 = 0.028$ ), although the peak value of both the induced angle and  $C_y$  were greater in  $\frac{d}{l} = 0$  compared to  $\frac{d}{l} = 0.25$ . Further analysis of the  $C_y$  curve revealed that the negative region of  $\frac{d}{l} = 0$  was greater than  $\frac{d}{l} = 0.25$ , hence resulting in a lower maximum power output.

Inspection of the pressure and velocity fields revealed that there are two mechanisms governing the transverse forcing. The first mechanism is the pressure difference in each shear layer, or the “streaming effect”. The second mechanism was the relative proximity of the top and bottom shear layers, or the “proximity effect”. The negative region in the  $C_y$  curves at low  $\frac{d}{l}$  is caused by the streaming effect dominating.

Comparison of the QSS and DNS predictions of maximum power showed similar trends. The maximum power increased as  $\frac{d}{l}$  decreased supporting the hypothesis of attaining higher power output through inhibition of shear layer reattachment. However, a significant error between the QSS and FSI simulations were observed as  $\frac{d}{l}$  was reduced.

Further investigations carried out using time averaged flow data concluded that the mean flow of FSI simulations had significant deviations from the DNS stationary simulations carried out at corresponding induced angles. This shows that the flow is essentially not quasi-static, violating the primary assumption of considering  $F_y$  as the sole driving force of

## 6. CONCLUSIONS

---

the system. Yet, it can be concluded that the QSS model can be used as a tool to obtain initial approximations to design galloping energy harvesting systems as the QSS data shows similar trends to the FSI simulations.

It is concluded that in order to obtain an efficient galloping energy harvesting system through inhibition of shear layer reattachment, one key design consideration is to obtain a cross section which has the optimum balance between the negative and positive regions of the  $C_y$  vs.  $\theta$  curve. Even though the inhibition of the shear layer reattachment through tapering of the trailing edge leads to higher power, as it approaches a triangle, a negative region of  $C_y$  emerges in the  $C_y$  vs.  $\theta$  curve. This leads to adverse power transfer. This region keeps increasing between  $0 \leq \frac{d}{T} \leq 0.25$ . Therefore, an optimum  $\frac{d}{T}$  should be obtained in order to get a balance between the negative and positive regions which then leads to an optimal energy transfer.

As for future research this method of attaining high power through inhibition of shear layer reattachment can be further developed by conducting more detailed investigations into the geometry to find ways to reduce the adverse power transfer which will lead to further increases in power output.

These conclusions support the second objective of this study: *“Understand the governing fluid mechanics of the system and to optimise and control these mechanics in order to obtain a higher power transfer.”*

# BIBLIOGRAPHY

---

- Alonso, G., Meseguer, J., Pérez-Grande, I., 2005. Galloping instabilities of two-dimensional triangular cross-section bodies. *Experiments in Fluids* 38, 789–795.
- Alonso, G., Meseguer, J., Sanz-Andrés, A., Valero, E., 2010. On the galloping instability of two-dimensional bodies having elliptical cross-sections. *Journal of Wind Engineering and Industrial Aerodynamics* 38, 789–795.
- Alonso, G., Valero, E., Meseguer, J., 2009. An analysis on the dependence on cross section geometry of galloping stability of two-dimensional bodies having either biconvex or rhomboidal cross sections. *European Journal of Mechanics B/Fluids* 28, 328–334.
- Barrero-Gil, A., Alonso, G., Sanz-Andres, A., Jul. 2010. Energy harvesting from transverse galloping. *Journal of Sound and Vibration* 329 (14), 2873–2883.
- Barrero-Gil, A., Sanz-Andrés, A., Roura, M., Oct. 2009. Transverse galloping at low Reynolds numbers. *Journal of Fluids and Structures* 25 (7), 1236–1242.
- Bearman, P. W., Gartshore, I. S., Maull, D. J., Parkinson, G. V., 1987. Experiments on flow-induced vibration of a square-section cylinder. *Journal of Fluids and Structures* 1, 19–34.
- Bernitsas, M. M., Ben-Simon, Y., Raghavan, K., Garcia, E. M. H., 2009. The VIVACE Converter: Model Tests at High Damping and Reynolds Number Around  $10^5$ . *Journal of Offshore Mechanics and Arctic Engineering* 131 (1), 011102.
- Bernitsas, M. M., Raghavan, K., Ben-Simon, Y., Garcia, E. M. H., 2008. VIVACE (Vortex Induced Vibration Aquatic Clean Energy): A new concept in generation of clean and

## BIBLIOGRAPHY

---

- renewable energy from fluid flow. *Journal of Offshore Mechanics and Arctic Engineering* 130 (4), 041101–15.
- Blevins, R. D., 1990. *Flow-Induced Vibration*, 2nd Edition. New York: Van Nostrand Reinhold.
- Bouclin, D. N., 1977. Hydroelastic oscillations of square cylinders. Master's thesis, University of British Columbia.
- Den Hartog, J. P., 1956. *Mechanical Vibrations*. Dover Books on Engineering. Dover Publications.
- Deniz, S. and Staubli, T., 1997. Oscillating rectangular and octagonal profiles: Interaction of leading-and trailing-edge vortex formation. *Journal of Fluids and Structures* 11, 3–31.
- Fletcher, C. A. J., 1984. *Computational Galerkin methods*. Springer-Verlag, New York.
- Fletcher, C. A. J., 1991. *Computational techniques for fluid dynamics*. Vol. 1. Springer-Verlag, New York. Gabbai,.
- Glauert, H., 1919. The rotation of an aerofoil about a fixed axis. Tech. rep., Advisory Committee on Aeronautics R and M 595. HMSO, London.
- Gresho, P. M., Sani, R. L., 1987. On pressure boundary conditions for the incompressible Navier–Stokes equations. *International journal for numerical methods in fluids* 7, 1111–1145.
- Griffith, M. D., Leontini, J. S., Thompson, M. C., Hourigan, K., 2011. Vortex shedding and three-dimensional behaviour of flow past a cylinder confined in a channel. *Journal of Fluids and Structures* 27 (5-6), 855–860.
- Joly, A., Etienne, S., Pelletier, D., Jan. 2012. Galloping of square cylinders in cross-flow at low Reynolds numbers. *Journal of Fluids and Structures* 28, 232–243.
- Karniadakis, G. E., Sherwin, S., 2005. *Spectral/hp element methods for computational fluid dynamics*, ii Edition. Oxford University.
- Kluger, J., Moon, F., Rand, R., 2013. Shape optimization of a blunt body vibro-wind galloping oscillator. *Journal of Fluids and Structures* 40, 185 – 200.

- Kreyszig, E., 2010. Advanced Engineering Mathematics, 10th Edition. John Wiley & Sons.
- Lee, J., Bernitsas, M., Nov. 2011. High-damping, high-Reynolds VIV tests for energy harnessing using the VIVACE converter. *Ocean Engineering* 38 (16), 1697–1712.
- Lee, J., Xiros, N., Bernitsas, M., Apr. 2011. Virtual damperspring system for VIV experiments and hydrokinetic energy conversion. *Ocean Engineering* 38 (5-6), 732–747.
- Leonard, A., Roshko, A., 2001. Aspects of flow-induced vibrations. *Journal of Fluids and Structures* 15, 415–425.
- Leontini, J. S., 2007. A numerical investigation of transversely-oscillating cylinders in two-dimensional flow. Ph.D. thesis, Monash University.
- Leontini, J. S., Lo Jacono, D., Thompson, M. C., Nov. 2011. A numerical study of an inline oscillating cylinder in a free stream. *Journal of Fluid Mechanics* 688, 551–568.
- Leontini, J. S., Thompson, M. C., 2013. Vortex-induced vibrations of a diamond cross-section: Sensitivity to corner sharpness. *Journal of Fluids and Structures* 39, 371–390.
- Leontini, J. S., Thompson, M. C., Hourigan, K., Apr. 2007. Three-dimensional transition in the wake of a transversely oscillating cylinder. *Journal of Fluid Mechanics* 577, 79.
- Luo, S., Chew, Y., Ng, Y., Aug. 2003. Hysteresis phenomenon in the galloping oscillation of a square cylinder. *Journal of Fluids and Structures* 18 (1), 103–118.
- Luo, S. C., Yazdani, M., Chew, Y. T., Lee, T. S., 1994. Effects of incidence and afterbody shape on flow past bluff cylinders. *Journal of Wind Engineering* 53, 375–399.
- Nakamura, Y., Mizota, T., 1975. Unsteady lifts and wakes of oscillating rectangular prisms. *ASCE Journal of the Engineering Mechanics Division* 101, 855–871.
- Nakamura, Y., Tomonari, Y., 1977. Galloping of rectangular prisms in a smooth and in a turbulent flow. *Journal of Sound and Vibration* 52, 233–241.
- Naudascher, E., Rockwell, D., 1994. Flow-induced vibrations: An engineering guide. A.A. Balkema, Rotterdam.

## BIBLIOGRAPHY

---

- Naudascher, E., Wang, Y., 1993. Flow induced vibrations of prismatic bodies and grids of prisms. *Journal of fluids and structures* 7, 341–373.
- Ng, Y., Luo, S., Chew, Y., Jan. 2005. On using high-order polynomial curve fits in the quasi-steady theory for square-cylinder galloping. *Journal of Fluids and Structures* 20 (1), 141–146.
- Païdoussis, M., Price, S., de Langre, E., 2010. *Fluid-Structure Interactions : Cross-Flow-Induced Instabilities*. Cambridge University Press.
- Parkinson, G., 1989. Phenomena and modelling of flow-induced vibrations of bluff bodies. *Progress in Aerospace Sciences* 26, 169–224.
- Parkinson, G., Brooks, N. P. H., 1961. On the aeroelastic instability of bluff cylinders. *Journal of Applied Mechanics* 28, 252–258.
- Parkinson, G. V., 1974. Mathematical models of flow-induced vibrations of bluff bodies. In *Flow-Induced Structural Vibrations*, e. naudascher Edition. Berlin: SpringerVerlag.
- Parkinson, G. V., Smith, J. D., 1964. The square prism as an aeroelastic non-linear oscillator. *The Quarterly Journal of Mechanics and Applied Mathematics* 17 (2), 225–239.
- Pregalato, C., 2003. Flow-induced vibrations of a tethered sphere. Ph.D. thesis, Monash University.
- Raghavan, K., Bernitsas, M., Apr. 2011. Experimental investigation of Reynolds number effect on vortex induced vibration of rigid circular cylinder on elastic supports. *Ocean Engineering* 38 (5-6), 719–731.
- Raghavan, K., Bernitsas, M. M., Maroulis, D. E., 2009. Effect of Bottom Boundary on VIV for Energy Harnessing at  $8 \times 10^3 < Re < 1.5 \times 10^5$ . *Journal of Offshore Mechanics and Arctic Engineering* 131 (3), 031102.
- Robertson, I., Li, L., Sherwin, S. J., Bearman, P. W., 2003. A numerical study of rotational and transverse galloping rectangular bodies. *Journal of Fluids and Structures* 17, 681 – 699.

- Ruscheweyh, H., Hortmanns, M., Schnakenberg, C., 1996. Vortex-excited vibrations and galloping of slender elements. *Journal of Wind Engineering and Industrial Aerodynamics* 65, 347–352.
- Sheard, G. J., Fitzgerald, M. J., Ryan, K., Jun. 2009. Cylinders with square cross-section: wake instabilities with incidence angle variation. *Journal of Fluid Mechanics* 630, 43.
- Shiels, D., Leonard, A., Roshko, A., 2001. Flow-induced vibration of a circular cylinder at limiting structural parameters. *Journal of Fluids and Structures* 15, 3–21.
- Thompson, M., Hourigan, K., Sheridan, J., Feb. 1996. Three-dimensional instabilities in the wake of a circular cylinder. *Experimental Thermal and Fluid Science* 12 (2), 190–196.
- Thompson, M. C., Hourigan, K., Cheung, A., Leweke, T., Nov. 2006. Hydrodynamics of a particle impact on a wall. *Applied Mathematical Modelling* 30 (11), 1356–1369.
- Tong, X., Luo, S., Khoo, B., Oct. 2008. Transition phenomena in the wake of an inclined square cylinder. *Journal of Fluids and Structures* 24 (7), 994–1005.
- Tu, J., Yeoh, G., Liu, C., 2008. *Computational Fluid Dynamics: A Practical Approach*, 1st Edition. Butterworth-Heinemann.
- Vicente-Ludlam, D., Barrero-Gil, A., Velazquez, A., 2014. Optimal electromagnetic energy extraction from transverse galloping. *Journal of Fluids and Structures* 51, 281–291.
- Vio, G., Dimitriadis, G., Cooper, J., Oct. 2007. Bifurcation analysis and limit cycle oscillation amplitude prediction methods applied to the aeroelastic galloping problem. *Journal of Fluids and Structures* 23 (7), 983–1011.
- Weaver, D. S., Veljkovic, I., 2005. Vortex shedding and galloping of open semi-circular and parabolic cylinders in cross-flow. *Journal of Fluids and Structures* 21, 65–74.
- White, F., 1999. *Fluid mechanics*, 4th Edition. McGraw-Hill, Boston.
- Williamson, C. H. K., Govardhan, R., 2004. Vortex-induced vibrations. *Annual Review of Fluid Mechanics* 36, 413–455.